

**MAPPING INTRACORTICAL MYELIN IN HUMANS USING
MAGNETIC RESONANCE IMAGING**

MAPPING INTRACORTICAL MYELIN IN HUMANS USING
MAGNETIC RESONANCE IMAGING
By CHRISTOPHER D ROWLEY, B.SC.

A Thesis Submitted to the School of Graduate Studies in Partial Fulfillment
of the Requirements for the Degree Doctorate of Philosophy

McMaster University © Copyright by Christopher Rowley June 2018

McMaster University DOCTORATE OF PHILOSOPHY (2018) Hamilton, Ontario
(Neuroscience)

TITLE: Mapping Intracortical Myelin in Humans using Magnetic Resonance Imaging

AUTHOR: Christopher D Rowley, B.Sc. (McMaster University)

SUPERVISOR: Dr. Nicholas Bock

SUPERVISORY COMMITTEE: Dr. Michael Noseworthy

Dr. Benicio Frey

NUMBER OF PAGES: xxi, 209

Abstract

Myelin is a protein complex which plays an integral role in developing and maintaining proper brain function. Due to the plasticity of the brain, and the dynamic nature of myelin, it is critical to develop methods that allow for the investigation of changes in myelin *in vivo*, to further our understanding of the brain. A substantial amount of myelin is found in the grey matter (GM) of the cerebral cortex – the outermost structure of the brain that supports higher order functions including cognition and more fundamental functions, such as sensation and motor control. While *in vivo* investigations have traditionally used imaging to focus on myelin in the deep white matter (WM) tracts in the brain, advances in magnetic resonance imaging (MRI) are now allowing investigations of intracortical myelin (ICM). The research in this thesis presents methodology for investigating intracortical myelin levels using magnetic resonance imaging (MRI) in humans, with the aim of developing a better understanding of how myelin contributes to healthy cortical function, and how it may be disrupted in disease.

To characterize intracortical myelin, a novel MRI analysis technique was developed early in this work to report the thickness of the heavily myelinated and lightly myelinated layers of the cortex. This measure of myelinated cortical thickness uses a clustering algorithm to separate the layers of the cortex based on voxel intensity in a T₁-weighted (T₁W) MRI with strong intracortical contrast. The resulting myelinated thickness maps match known myelin profiles of the brain, with cortical regions such as the primary visual and motor cortices displaying proportionally thicker, heavily myelinated layers. The utility of the myelinated cortical thickness for answering clinical

questions was tested in bipolar disorder, where a preferential loss of the more myelinated layers in the dorsal lateral prefrontal cortex was found. This study provided the first in vivo evidence of ICM disruptions in bipolar disorder.

Later in the thesis work, after surface-based analysis techniques became available, an alternative approach to investigate intracortical myelin was developed that sampled the T_1W image intensity at a calculated depth of the cortex as a measure of myelin content. This methodology was used for studying the association of ICM with age in healthy adults ranging from late adolescence to middle-adulthood. It was found that three cortical depths followed a similar trajectory through this age-span, reaching their peak between 35 and 40 years of age. This study contributes to a picture of ICM amounts increasing well into middle age in healthy adults and provides a baseline for studies investigating how this may be disrupted in disease

Up to this point, the analysis in the thesis used a specialized T_1W MRI that had been optimized to provide strong intracortical contrast, but a question remained of how useful the technique would be if more commonly collected clinical MRIs were used as inputs. This analysis was thus applied to standard T_1W and T_2 -weighted (T_2W) anatomical MRIs to test its clinical applicability. 360 participants were investigated from the TRACK-HD dataset to test if intracortical signal analysis could follow the progression of Huntington's disease. A significant increase in intracortical T_1W/T_2W signal was found in the most advanced disease group in several cortical regions. This increase in intracortical signal is likely tracking a known increase in iron and/or myelin levels in the Huntington's disease brain. However, this work suggests that ICM studies would best be

conducted with optimized imaging to better be able to characterize the subtle ICM variations within the GM.

Overall, the work in this thesis presents two techniques for whole-brain mapping of the distribution of intracortical myelin using MRI. The clinical applicability of the techniques was demonstrated in examples of mental and neurodegenerative disorders. The future directions of this work include developing imaging specific to either myelin or iron as well as revisiting these problems while imaging at greater resolution to better characterize the laminar profile across the cortex.

Acknowledgements

The research in this thesis would not have been possible without the contributions of many. I am extraordinarily grateful for the opportunities my supervisor Dr. Nicholas Bock has provided me with, including two undergraduate summer terms prior to taking me under his wing for my PhD studies. Without the learning environment you have built up, and your lessons in science and communication, my learning curve would not have been nearly as steep. Within the lab, I have to thank Eyesha Hashim for teaching me the ropes of brain segmentations. Kim Desmond, you have provided critical input to help develop my Matlab scripts, without which, very little of this research would have been completed! I am also appreciative to the new comers to the Bock lab: Rachelle, Christie and Laagi, all of which helped contribute to the good lab vibes.

Additionally, I am appreciative of the support from other researchers that have helped shape my mind into what it is today. Dr. Benicio Frey has opened my eyes to the applications of MRI to mental health. Dr. Mike Noseworthy has provided insight on MR physics in addition to his mind-blowing rock shows at ISMRM. Also thank you to my comprehensive committee members Dr. Hall and Dr. Mazurek who challenged me greatly to tackle a research question with methods outside my immediate field. I am grateful for Dr. Luciano Minuzzi providing me with a comprehensive understanding of statistics. Much of this work would not have been possible without the great recruiting work of Dr. Manpreet Sehmbi. And thanks to Dr. Tardif and Dr. Bazin who provided the technical support allowing me to get my surface pipeline running.

My friends outside the lab have also helped me develop my critical thinking and communication skills, as well as help me keep stress down to a minimum. Lise, you were the scientist I aspired to become as I went through my undergrad. You provided invaluable mentorship including helping me come up with the idea for the work in Huntington's Disease. Jill, you have tremendously improved my writing and vocabulary through our extensive email chains. Thank you Izzie for being there post-crash, when I looked far from my best. Thanks to Zach, who has been there for me since elementary school. Dhruv, you were my best science friend since the beginning! And to my old roommates Josh and Adam who helped me through undergrad.

Cycling has helped me out so much mentally, so it cannot be left out here. Jacques, Robert, Dan, Chris K and Raye, you have all one way or another, helped me stay on the saddle. Thank you Dr. Bock for accommodating the injuries I sustained during grad school, and forcing me to take a week off with my concussion. My 'properly' functioning brain thanks you every day! And thank you Jill for slugging out some killer spin class sessions with me through the Canadian winters. Thank you to my many other riding partners who have helped ensure my time on the bike drained any built up stress allowing me to think clearly again.

Finally, thank you to my family for helping me out from the very beginning. You provided my life with a strong foundation, on which I was able to build upon. To my brother Jesse, who isn't afraid to tell me I am wrong or I messed up. You are constantly challenging me to improve. Thank you Kayla for being the support that I didn't know I

needed. Rick, you helped keep my family afloat and built confidence into each of us. And thank you so much to my mom who has put herself through so much to ensure I had access to the opportunities that I wanted. And thank you to my Nana and Papa who have always provided their unconditional support.

Table of Contents

Title Page	ii
Descriptive Note	iii
Abstract	iv
Acknowledgements	vii
Table of Contents	x
List of Tables	xviii
Abbreviations and Symbols	xix
Chapter 1: Introduction	1
1.1 Cerebral Cortex.....	2
1.2 Myelin.....	6
1.3 Magnetic Resonance Imaging.....	12
1.4 Image Processing Techniques for Cerebral Cortex	26
1.7 Research Objectives and Overview	29
References.....	31
Chapter 2: Assessing intracortical myelin in the living human brain using myelinated cortical thickness	46
Preamble	46
Abstract.....	56
2.1 Introduction.....	57
2.2 Methods.....	65
2.3 Results.....	75

2.4 Discussion and Conclusion	88
References	94
Chapter 3: Age-related mapping of intracortical myelin from late adolescence to middle adulthood using T₁-weighted MRI	106
Preamble	106
Abstract	113
3.1: Introduction	116
3.2: Methods	119
3.3 Results	126
3.4 Discussion	137
3.5 Conclusion	143
References	144
Chapter 4: Altered Intracortical T₁-weighted/T₂-weighted ratio signal in Huntington's Disease	156
Preamble	156
Abstract:	165
4.1 Introduction	165
4.2 Methods	168
4.3 Results	174
4.4 Discussion	178
4.5 Conclusions	182
References	183

Chapter 5: Future Directions and Conclusions.....	193
5.1 Conclusions.....	193
5.2 Future Directions	194
References.....	203
Appendices.....	209

List of Illustrations, Charts, Diagrams

Figure 1.1: Representation of the layered structure of the cortex. Left: The layering of the cortex can be visualized by cell body or myelin staining of tissue. Right: Four primary patterns of cortical myelination that can be found across the cerebrum. Adapted from Nieuwenhuys (2012).	6
Figure 1.2: Cartoon representation of three functions that oligodendrocytes and their myelin sheaths have within the CNS.	10
Figure 1.3: Illustration of primary mechanisms driving image contrasts used for ICM mapping (left), with resulting MRI images displayed on the right. R_1 describes the longitudinal relaxation of protons back to the main magnetic field, after being excited by an RF pulse. R_2^* contrast is derived from transverse relaxation generated from local field inhomogeneities altering the Larmor frequency of the protons. MT contrast results from a selective RF excitation of bound protons that exchange magnetization with protons in the unbound pool. Finally, QSM represents the changes in the local magnetic	16

field driven largely by dipole-dipole interactions and magnetic sources within the tissue. MRI images are adapted from Callaghan et al., (2014) and Acosta-Cabronero et al., (2016).

Figure 1.4: A visual representation of the processing pipeline of images for ICM mapping. Once the GM and WM surfaces have been defined for each subject, a half depth surface can be calculated. The corresponding MRI data values are then mapped to this surface. Finally, the surface is registered to a group template permitting vertex-wise statistical analysis. 26

Figure 2.1: Myelinated cortical thickness measurements. The depth of the human cerebral cortex can be roughly subdivided into lightly myelinated and heavily myelinated portions, as seen in representative 40 μm thick histological sections stained for myelin (adapted from Braitenberg, 1962). This leads to intracortical contrast on heavily T_1 -weighted MRI, which can be used to segment the cerebrum into lightly myelinated gray matter (GM), heavily myelinated gray matter (mGM), and white matter (WM) tissue classes. Measuring the thickness of the GM and mGM tissue classes yields the thickness of the lightly myelinated (G) and heavily myelinated cortical layers (M). Overall cortical thickness (T) is also measured. The mGM class is thicker in regions known to be highly myelinated, such as the primary motor cortex in the precentral gyrus (PG) and the primary auditory cortex in 55

Heschl's gyri (HG), MFG, middle frontal gyrus.

Figure 2.2: Tissue segmentation results shown for a representative individual **70**
for WM fuzzy c-means threshold values greater than 0.5 or 0.1. Each
histogram plots the number of voxels assigned to each class in the cerebrum
against normalized MRI signal intensity and each image shows the resulting
segmentation superimposed on a 2D slice from the 3D Ratio MRI. Note the
improved definition of the mGM/WM boundary in the thin gyral blade of
white matter located at the white arrow.

Figure 2.3: Dorsal views of four thickness measures in an atlas made from 20 **72**
female subjects. T, total cortical thickness; G, unmyelinated cortical
thickness; M, myelinated cortical thickness; P, proportional myelinated
thickness; PreCG, precentral gyrus; PostCG, postcentral gyrus.

Figure 2.4: Views of proportional myelinated thickness, P, in an atlas made **73**
from 20 female subjects.

Figure 2.5: (A) Representative coronal section of the dorsal frontal cortex **75(A),**
stained for myelin showing the distribution of bundles of myelinated fibers on **76(B)**
the middle frontal gyrus (MFG) [Brodmann's area 46 (BA 46)], on the anterior
cingulate gyrus (aCG), and in the inferior frontal sulcus (IFS). The white
dotted line shows the rough extent of bundles over the three regions. The

asterisk denotes the same blood vessel at each magnification. The bottom panel shows the location of regions on an inflated atlas of M in the right hemisphere in healthy controls on medial and dorsal views, respectively, pCG, posterior cingulate gyrus. (B) 10X magnification in the MFG illustrating bundles of myelinated fibers and distinctly darker blood vessels.

Figure 2.6: Thickness measurements in controls and bipolar disorder type-I subjects ($n = 10$ in each group). **78**

Figure 2.7: Region-of-interest thickness measurements ($\mu \pm \sigma$, $n = 10$ in each group) in the middle frontal gyrus (MFG) and precentral gyrus (PCG). An asterisk denotes statistical significance between control and bipolar groups at $p < 0.05$. **80**

Supplementary Figure 2.8: Individual region-of-interest thickness measures in the middle frontal gyrus (MFG) and precentral gyrus (PCG). The blue colored dot indicates the mean for each group. **81**

Figure 3.1: Illustration of measured T_1 -weighted signal at four depths. Left: 1 mm isotropic T_1 -weighted scan with high intracortical myelin contrast. Right: Four depth-dependent surfaces in and beneath the cortex, which sample the MRI signal. SWM, superficial white matter. **118**

Figure 3.2: GLM fit metrics mapped across the brain. Top: r^2 values for MARS atlas ROIs with signal for the half-depth regressed against age (linear) and age² (quadratic). An increasing yellow hue in the map values indicates more variability is explained by the model fit. Bottom: P value for the fit models. An increasing green hue in the map values depicts a more significant model fit. **121**

Figure 3.3: Age trajectory from superficial cortex to deep WM. Data plotted for an ROI (caudal dorsomedial prefrontal cortex) in all subjects where the quadratic model fit the signal data at all depths. This is contrasted against the signal of a volumetric ROI placed in the superior longitudinal fasciculus (SLF) in deep white matter, which demonstrated no significant effect with age over this range. Shaded regions denote the 95% confidence interval. **122**

Figure 3.4: Four sample ROIs displaying the T₁-weighted signal intensity values fit against age. Shading surrounding the quadratic fit line denotes the 95% confidence interval. Top left: cuneus. Parameters extracted from the quadratic for further analysis are highlighted on this plot. “h” is the age where the maximum signal occurs based on the quadratic fit. “k” is the maximal signal achieved in this brain region. Top right: caudal superior temporal cortex. Bottom left: rostral dorsolateral superior prefrontal cortex. Bottom right: dorsomedial motor cortex. **125**

Figure 3.5: Mapping quadratic parameters across the cortex. Quadratic **126**

parameters calculated from the GLM fit shown for vertex-wise calculations and with signal first averaged across an ROI. Left: The maximum signal reached across the cortex as predicted by the quadratic model or using a smoothing spline (bottom). Right: The temporal shift of the maximum signal value as estimated by the quadratic model, or by the smoothing spline (bottom), is mapped across the cortex.

Figure 3.6: Calculated quadratic parameters across three cortical depths. Top **128**

left: Illustration of the cortical sampling surfaces overlaid on the T_1 -weighted image. Top row: The maximum signal for each vertex at each depth (voxel-wise). Bottom row: The temporal shift of the quadratic fit of the signal intensity with age (averaged over ROI).

Figure 3.7: K-means clustering on peak age signal. Left: K-means clustering **130**

of ROIs into four clusters based on the age when the maximal T_1 -weighted signal is reached. Right: The signal values in all ROIs within each cluster were averaged, and then Z-scores were calculated within each cluster to visualize the signal trajectory. Plotted solid lines highlight the quadratic fit for the half cortical depth signal. Temporal shift (vertical dotted line) increases from cluster 1 to cluster 4.

- Supplementary Figure 3.8:** The number of clusters used in the k-means ROI grouping, and the resulting summed distance to the centroids from each data point. The summed residuals was used as a marker of explained variance. Four clusters was chosen using the elbow method, such that adding more clusters provided a very small decrease in explained variance, and removing clusters added much more. **131**
- Figure 4.1:** T_1W/T_2W ratio changes in HD. Standardized coefficients from the intracortical signal analysis are mapped onto the cortex. Significant changes are seen only in the Stage 2 HD group (highlighted in the bottom panel). **170**
- Figure 4.2:** Separate analysis of T_1W and T_2W signal changes in HD Stage 2. Many of the same regions that were significant for T_1W/T_2W signal in HD Stage 2 relative to control show significant T_2W signal changes ($p < 0.05$ uncorrected). **172**
- Figure 5.1:** Potential mechanisms that could increase intensity in a T_1W image, and/or decrease intensity in a T_2W image. **191**

List of Tables

- Table 2.1:** Subject demographics for the bipolar study presented as mean \pm standard deviation. **60**

Table 4.1: Demographics for the participants used from the baseline TRACK- 164

HD dataset. Disease-burden score = Age \times (CAG length – 35.5). Data values are mean (SD), or number (%).

Abbreviations and Symbols

AIC – Akaike Information Criterion

ARC – Autocalibrating Reconstruction for Cartesian Imaging

BD – Bipolar Disorder

BRAVO – Brain Volume imaging

CSF – Cerebrospinal Fluid

DLPFC – Dorsal Lateral Prefrontal Cortex

DSM – Diagnostic and Statistical Manual

DTI – Diffusion Tensor Imaging

FA – Flip Angle

FLASH – Fast Low Angle Shot

FOV – Field Of View

GE – General Electric

GLM – General Linear Model

GM – Gray Matter

HD – Huntington’s Disease

HTT – huntingtin

ICM – Intracortical Myelin

MBP – Myelin Basic Protein

MCT – Myelinated Cortical Thickness

MPRAGE – Magnetization Prepared Rapidly Acquired Gradient Echo

MRI – Magnetic Resonance Imaging

ms - millisecond

MSN – Medium Spiny Neuron

RF – Radiofrequency

SAR – Specific Absorption Rate

SLF – Superior Longitudinal Fasciculus

SWM – Superficial White Matter

TD – Time Delay

TE – Echo Time

TI – Inversion Time

TR – Repetition Time

VBM – Voxel Based Morphometry

WM – White Matter

B_1 – Radio Frequency Field

B_1^- – Receive Field

B_1^+ – Transmit Field

Chapter 1: Introduction

Studying the structure of the brain *in vivo* has been stimulated with the creation of magnetic resonance imaging (MRI). Technological advancements in MRI have drastically improved images, which have resulted in an increased understanding of the brain. The research laid out in this thesis has taken advantage of computational advancements to uncover structural changes in the brain with healthy aging, and in disease. This introduction begins by reviewing the histological work conducted in the early 20th century that aimed to parcellate the cerebral cortex into what the researchers postulated may be functionally significant regions. Using the myelin content of the cortical region was one method to parcellate the cerebral cortex, but it was not until nearly two decades later where myelin's utility in speeding neural signaling was discovered. Thus, following the historical timeline, the structure and function of myelin is next examined. With an understanding of the significance of myelin in the cerebral cortex, MRI is presented with its ability to capture information about intracortical myelin in the acquired images. Continuing with the historical progression, studies using MRI myelin mapping techniques are reviewed before an overview of the software advancements that were necessary for whole-brain myelin mapping techniques.

The aims of ICM mapping with MRI tend to be two-fold: 1) to develop parcellations of the cerebral cortex, and 2) to study the role of ICM in supporting healthy cortical function and its potential disruption in brain disease. The studies in this thesis focus on the later.

1.1 Cerebral Cortex

The cerebral cortex comprises a layer of gray matter (GM) that surrounds the white matter (WM) of the brain. The cortex forms a convoluted surface at the outside of the brain, whose thickness is regionally dependent and varies from 2-5mm (Triarhou, 2007). Thickness is well conserved across mammals, although the cortical surface area increases with increasing brain size within classes of mammals (Fish, Dehay, Kennedy, & Huttner, 2008). The cortex appears to be composed of columnar processing units (Mountcastle, 1997), where an increase in columns would yield an increase in surface area. It is known that these columnar units are highly structured, where groups of columns make up different areas responsible for different processing functions. This can include fundamental functions such as processing visual information from the eyes, sensing touch and initiating movement, as well as higher order functions such as behaviour, memory and cognition. Thus the underlying structure may provide insight into the functionality of an area.

1.1.1 Cell Types and Distribution

The cortex is composed of two principal cell types: neurons and glial cells. Neurons come in different forms, all of which can fire action potentials to transfer information to the next connected neuron. They are classified based on size, shape and the number of dendrites and axons they have. Glial cells act as supporting cells in the brain, and can be further broken down into microglia, astrocytes and oligodendrocytes, whose respective glial proportions in the brain are 5%, 20% and 75% (Pelvig, Pakkenberg,

Stark, & Pakkenberg, 2008). In the adult brain, it is known that glial cells outnumber the neurons in a ratio ranging from of 1.32 to 1.49 (Pelvig et al., 2008). The abundance of glial cells suggests that they play an integral role to proper brain functioning. For instance, oligodendrocytes produce myelin, an insulating substance that ensheaths neuronal axons to provide structural and functional support to the neuron.

Visually, the cerebral cortex can be divided into six layers based on the density of neuronal cell types. Each layer contains specific types of cells that relate to the function of that layer. The layers moving inwards from the cortical surface to the WM are as follows: (I) the cell-poor zonal layer, (II) the external granular layer, (III) the external pyramidal layer, (VI) the internal granular layer, (V) the internal pyramidal layer, and (VI) the multiform layer (Nieuwenhuys, 2012). These layers exist across the cortex in varying thicknesses that are regionally dependent.

Since the distribution of cells in the cortex is highly organized, it has been hypothesized that the underlying cortical structure is related to its function. Thus the distribution of cell types across the cortex has been used to parcellate it into regions thought to be functionally significant (Nieuwenhuys, 2012). Historically, cortical parcellation has been performed histologically by one of two ways: using a stain for cell bodies to differentiate based on neuronal cell type distribution (cytoarchitecture), or by using a myelin stain and differentiating regions based on differences in myelin fiber distributions (myeloarchitecture) (Nieuwenhuys, 2012).

1.1.2 Cytoarchitecture

Cytoarchitectural parcellations are more well-known in neuroscience and are conducted by using a Nissl stain for neuronal cell bodies, and then visualizing neuronal distribution under a light microscope. This approach produced the famous Brodmann map that divided the cortex into 43 areas. This map was produced from the work performed by Korbinian Brodmann in the early 20th century (Nieuwenhuys, 2012). The Brodmann map is still used widely in neuroimaging studies as a reference to localize functional signals to specific cortical areas. There is, however, significant variation between individuals within the same species for the borders of these Brodmann areas (Lashley & Clark, 1946). A weakness in this parcellation method is that there is a lack of knowledge on the extent of intersubject variability from cytoarchitecture work (Zilles & Amunts, 2010), making direct intersubject comparisons difficult. It is also not currently possible to accurately parcellate the cortex based on cytoarchitecture *in vivo*. However, it remains as a simple naming system to describe different structural areas of the cortex, which may be more focal than using the labels of the gyri and sulci.

1.1.3 Myeloarchitecture

In addition to neuronal cell bodies in the cortex, there are many myelinated fibers that run both radially and tangentially through the depth of the cortex. These fibers form regionally distinct patterns that allow for cortical parcellation by grouping similar patterned regions together. The study of these fibers for cortical parcellation began with Oskar and Cécile Vogt, who divided the cortex into approximately 200 regions

(Nieuwenhuys, 2012). While this parcellation contains many more regions than Brodmann's map, the primary regional boundaries between the two are very similar. Other groups have produced myeloarchitectonic maps with a varying number of delineated regions. This is likely due to the fact that there are no sharp transitions between regions, but rather gradual shifts in fiber densities, which allows for subjectivity in the parcellation (Braitenberg, 1962).

Myeloarchitecture studies can be performed using different staining techniques such as a Weigert stain or Luxol Fast Blue to stain for myelinated fibers which are then viewed under light microscope (Schmued, 1990). Using a myelin stain, some of the six cortical layers can be further subdivided based on the quantity of tangentially myelinated fibers they contain. Based on the tangential myelinated fibers, there has been found to be four principal types of cortical tissue: *bistriate*, *unistriate*, *unitostriate* and *astriate* (Figure 1.1). The first contains two Bands of Baillarger in layers IV and V of the cortex that are separate from the heavily myelinated layer VI. The second type is similar to the first, except now the inner band cannot be distinguished from layer VI. *Unitostriate* cortex can be visualized when the two bands merge together, and there is a clear distinction from layer VI. The final *astriate* layer appears as one myelinated section from layer IV to layer VI. For this thesis, it is important to note that intracortical (ICM) patterns change across the brain in both the thickness of the myelinated layers and in the density of myelin present in these layers. Unlike cytoarchitecture, myeloarchitecture can be investigated *in vivo* using MRI because the patterns are visible at a mesoscopic scale. Much histological-based research has been done to establish the functional significance of

myelin sheaths, such that being able to map ICM *in vivo* is now of increased interest to uncover regional functions of the cortex and to monitor disease progression.

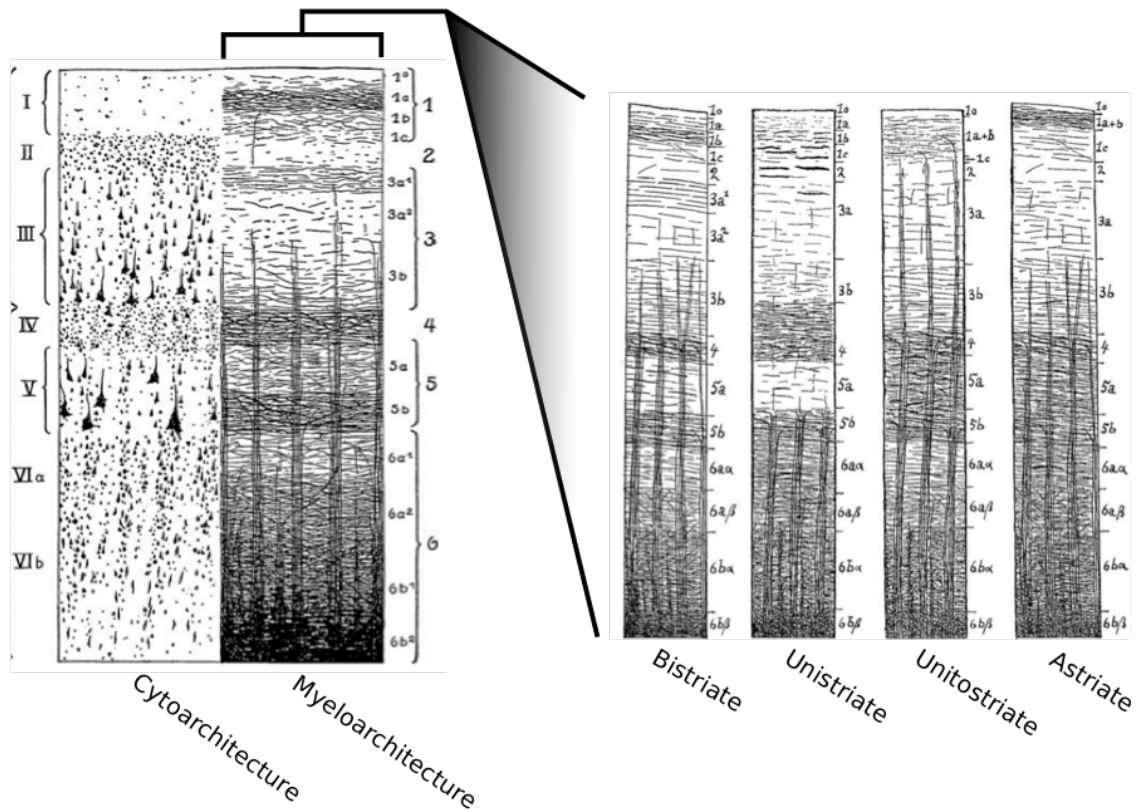


Figure 1.1: Representation of the layered structure of the cortex. Left: The layering of the cortex can be visualized by cell body or myelin staining of tissue. Right: Four primary patterns of cortical myelination that can be found across the cerebrum. Adapted from Nieuwenhuys (2012).

1.2 Myelin

Myelin is a membranous structure with a high lipid, and low water content that

surrounds an axon (Baumann & Pham-Dinh, 2001). Oligodendrocytes produce the myelin sheathing in the central nervous system (CNS), whereas Schwann cells comprise the sheaths in the peripheral nervous system. The structure of the sheath is similar in both conditions, but in this introduction the focus will be on oligodendrocytes in the CNS.

1.2.1 Sheath Structure

The myelin sheath consists of a spiral layer of cytoplasmic membrane from an oligodendrocyte that surrounds a portion of a neuron's axon. An oligodendrocyte can myelinate up to 30 axons (Butt & Ransom, 1989), with adjacent sheaths on axons belonging to different oligodendrocytes (Baumann & Pham-Dinh, 2001). The relative water content of a myelin sheath is 40%, which is roughly half the water content averaged over GM (Baumann & Pham-Dinh, 2001). Myelin by dry weight is 70% lipids and 30% proteins (Baumann & Pham-Dinh, 2001). The lipids within myelin are primarily cholesterol, phospholipids and glycolipids, found in a ratio ranging from 4:3:2 to 4:4:2 (Baumann & Pham-Dinh, 2001), and it is these lipids that largely make myelin MRI-detectable. In terms of protein composition, Myelin Basic Protein (MBP) and proteolipid (PLP) protein make up 80% of myelin proteins (Baumann & Pham-Dinh, 2001). MBP has been suggested to play an important role in the compaction of the myelin sheath (Baumann & Pham-Dinh, 2001), where PLP has been suggested to form stabilizing junctions (Boison, Büssow, D'Urso, Müller, & Stoffel, 1995). The length of the sheaths can vary from 150-200µm, connected to oligodendrocytes by processes 15-30µm in length (Butt & Ransom, 1989).

Myelin may play an important role in brain plasticity, due to its dynamic nature. It has been shown that the compaction of the myelin sheath can be affected by extracellular molecules such as transferrin (Marta et al., 2003). Recently, the direct evidence for the plasticity of sheaths has shown that axonal myelination patterns are maintained once established (Auer, Vagionitis, & Czopka, 2018). In the event of insult to a myelin sheath, neighbouring sheaths will adjust in size until the sheath can regenerate (Auer et al., 2018). Thus, the dynamic nature of myelin makes it an interesting neurobiological candidate for how the function of the cortex can change over the lifespan and in disease.

1.2.2 Function of Myelin

Research suggests that myelin has multiple functions in the CNS. Myelin is primarily known for its role in speeding neural signal conduction. Myelin permits efficient saltatory conduction, first described in 1925 (Lillie, 1925), where only unmyelinated sections of the axon contain ion channels for depolarization. The region between myelin sheaths is called a Node of Ranvier, and has a dense packing of sodium channels to facilitate the rapid depolarization of the axonal membrane. The high lipid and low water content give the myelin membrane a high resistance and low capacitance, which accelerates the movement of current down the axon in saltatory conduction (Huxley & Stämpfli, 1949). This allows the propagation of current down the axon to move up to ten times as quickly, compared to an unmyelinated axon (Lillie, 1925). There is an ongoing regulation of sheath and axonal properties to fine tune conduction speed and thus neuronal circuit timing (reviewed in (Seidl, 2014)). Thus myelin plays an integral role in maintaining temporal accuracy of neural circuits. From an energetics point

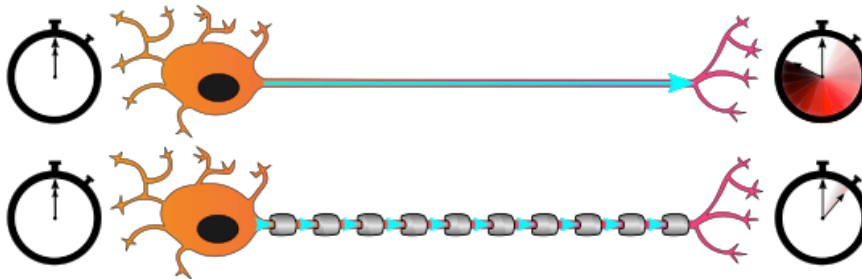
of view, myelin utilizes more energy to be maintained relative to the energy saved from saltatory conduction (Harris & Attwell, 2012). However, it has been shown that their existence is critical for additional functions within the CNS, potentially justifying their high metabolic rates.

An secondary role of myelin is to provide metabolic support for neurons (Nave, 2010). As up to 99% of an axon can be covered by myelin, the axon requires a source of energy as it cannot access the compounds in the extracellular space (Morrison, Lee, & Rothstein, 2013). Multiple studies have provided evidence that oligodendrocytes perform aerobic glycolysis where some of the products of the process such as lactate and pyruvate are provided to neurons for energy (Fünfschilling et al., 2013). It was found that when the lactate transporter in oligodendrocytes was inhibited, axons became damaged and there was abundant neuronal death (Lee et al., 2013). Further evidence has been provided in a mouse model with the knockout of a myelin:axon junction protein, where knockout mice demonstrated aberrant mitochondria in nodal regions of the axon (Einheber, Bhat, & Salzer, 2006). This appears to be a symbiotic relationship as neurons then provide N-acetylaspartate (NAA) from the breakdown of these products to be used for production of fatty acids (Jalil et al., 2005). Combined, this evidence suggests that myelin sheaths aid in the survival and proper function of neuronal axons.

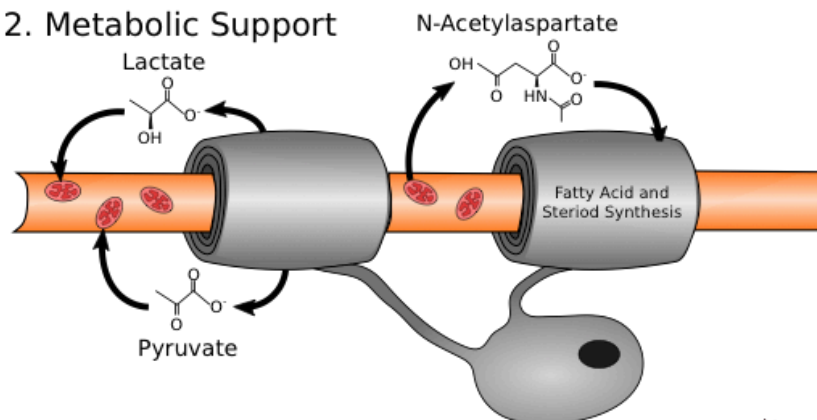
A third role exists for myelin in where it can act like a ‘guard rail’ for axons. Myelin in the CNS contains neurite growth inhibitors that may serve as a boundary and for guidance to late developing neurons. This was demonstrated in the rat corticospinal tract, where the blocking of one of these inhibitors lead to aberrant axonal formation

being mixed in with neighbouring tracts (Schwab & Schnell, 1991). Additionally it has been shown that oligodendrocytes promote the radial growth of axons by signaling for the reorganization of the neurofilament network (Sánchez, Hassinger, Paskevich, Shine, & Nixon, 1996). These studies highlight the regulatory role of oligodendrocytes in the structural development of neural networks.

1. Speed Signal Conduction



2. Metabolic Support



3. Axonal Guidance

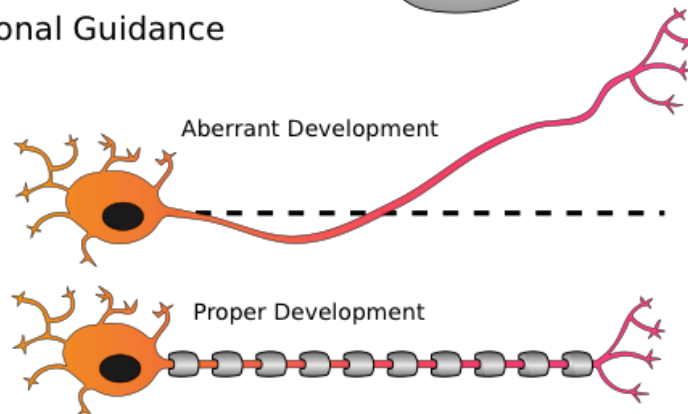


Figure 1.2: Cartoon representation of three functions that oligodendrocytes and their myelin sheaths have within the CNS.

These three functions of myelin combine to help build, maintain and fine tune neural circuits, which has a direct impact on an organism's ability to perform a task. For instance, it has been shown in mice that an increase in myelin is necessary for an improvement in a motor task (Gibson et al., 2014). Oligodendrocytes are fast acting to external stimulus as it has been shown that an increase in myelination can start within a few hours of a training task (Xiao et al., 2016). There is no doubt that myelin plays a crucial, if not complicated, role in the nervous system, and thus the study of it should help us better understand how the brain functions.

1.2.3 Myelin Mapping with MRI

While histological studies have used both cytoarchitecture and myeloarchitecture to parcellate the cortex, MRI has primarily used the latter. This is because commonly acquired image intensities have been found to be more correlated with myelin staining compared to cell body staining (Eickhoff et al., 2005). Thus, MR signals can be used as proxies for the underlying myelin density in the cortex. Indeed, *in vivo* visualizations of myeloarchitecture have been around for some time (V. P. Clark, Courchesne, & Grafe, 1992), but has only recently gained traction for mapping the entire cortex thanks to improved imaging resolution and cortical coverage, methods for bias field correction, increased computational power, and the availability of software to perform the

computations. The resurgence of the technique came with a study showing the effectiveness of the technique in marmosets with MRI and matched histology (Bock, Kocharyan, Liu, & Silva, 2009). A few years later, a “myelin map” in humans was published using MRI (Glasser & Van Essen, 2011).

1.3 Magnetic Resonance Imaging

MRI can be used to visualize myelin levels in the cortex and is the modality used for the myelin mapping in this thesis. MRI is primarily based off of the work by Joseph Larmor, who discovered the relationship between an external magnetic field, the precession frequency of proton which is placed in the field and the gyromagnetic ratio (Tubridy & McKinstry, 2000). The journey of MRI continued with the work done by Purcell and Bloch on ‘nuclear induction’ around 1945 (McRobbie, Moore, Graves, & Prince, 2009). This work proved that a signal could be collected in a coil from a sample that was subjected to radiofrequency energy, given at the sample’s resonant frequency. In 1973, Paul Lauterbur proposed the use of magnetic field gradients for spatial coding in MRI (McRobbie et al., 2009). Following this in 1974, Peter Mansfield’s group developed the process for slice selection (McRobbie et al., 2009). The final major piece of the puzzle was generated by Richard Ernst’s group, who developed 2D Fourier Transform imaging (McRobbie et al., 2009).

While the development of the first imaging scanner took some time since Larmor’s discovery, much work was performed to learn about the nuclear properties in a magnetic field during this time. It was found that there are three types of relaxation for

protons to realign with a magnetic field: T_1 , T_2 and T_2^* . T_1 relaxation describes the time it takes for the net magnetic moment of precessing protons to realign with the main magnetic field after being tilted away from it. T_2 and T_2^* describe the dephasing of precessing protons, and ultimately, the decay of the MR signal. Importantly for contrast in the brain, the values of these three relaxations are determined by the electrical and magnetic microenvironments of the individual protons (Vymazal et al., 1995).

MRI imaging works by selectively exciting the protons in water molecules, and recording the electrical signal they radiate as they relax to align with the magnetic field. Water is chosen as the excitation molecule as it can provide a strong signal with human tissue comprised of 70-90% water (McRobbie et al., 2009). The T_1 relaxation of brain tissue can range from 0.5 to 1 second, where the T_2 relaxation is on the order of 100msec or less (Vymazal et al., 1995). The following section will highlight different compounds that will alter these relaxation rates, permitting the distinction of myelinated from unmyelinated tissue.

1.3.1 How Myelin Affects T_1W and T_2W contrast

Myelin contrast in MRI images is primarily generated from its high lipid content. Increased levels of cholesterol and lipids decrease both T_1 and T_2 relaxation of water protons through dipole cross relaxation (Ceckler, Wolff, Yip, Simon, & Balaban, 1992). As such, the lipid and cholesterol dense WM has a shorter T_1 and T_2 compared to that of GM (Stanisz et al., 2005). This has the ultimate effect of fatty tissue presenting brighter on a T_1W image, and darker in a T_2W image. Since a large component of myelin is a lipid

membrane with cholesterol, areas of high amounts of myelin can then be delineated from regions of less myelin. In fact, MRI parameters can be optimized to increase the image contrast in the cortex of myelinated regions (Bock et al., 2013). However, T_1 and T_2 relaxation values are affected by many surrounding substances in the protons' local environment, and thus it has been suggested that iron levels contribute to the myelin contrast in MRI.

Ferritin is a primary source of iron storage in the brain that colocalizes with myelin (Fukunaga et al., 2010) and is stored in high quantities in oligodendrocytes. Thus, iron could provide image contrast to distinguish highly myelinated areas from areas with less myelin. Due to iron's magnetic properties, it is known to have a large impact on MR parameters, and exists in two ionic forms: Fe(III) and Fe(II). While both are paramagnetic ions, Fe(III) ion has 5 unpaired electrons, where Fe(II) has 4, making Fe(III) a stronger paramagnet (Saini, Frankel, Stark, & Ferrucci, 1988). The ferritin core has been found to be antiferrimagnetic, but still contains a superparamagnetic moment due to the incomplete cancelling of magnetic moments that leads to a shortening of T_2 (Brooks, Vymazal, Goldfarb, Bulte, & Aisen, 1998). Paramagnetic iron exists on the core surface in ferritin and it believed to be responsible for the weak shortening of T_1 (Brooks et al., 1998). The effect of ferritin on T_1 and T_2 is also non-linearly dependent on the number of iron atoms it contains (Brooks et al., 1998). To summarize, an increase in iron stored in ferritin leads to a decrease in T_2 W signal, and an increase in T_1 W signal (Vymazal et al., 1995). While it is not currently possible to know the proportion of contrast that comes from lipid and cholesterol compared to iron, it has previously been suggested that iron contributes 36%

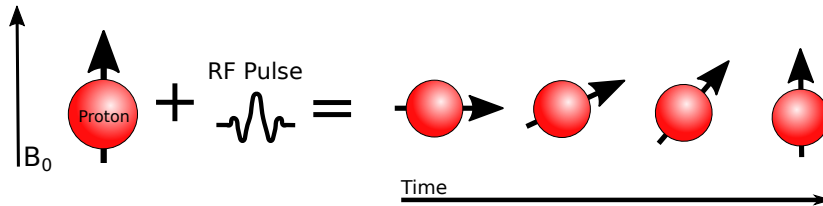
of T_1 contrast and myelin provides 64% (Stüber et al., 2014). However, this distinction may not be necessary due to the high level of colocalization between iron and myelin in the cortex (Fukunaga et al., 2010).

1.3.2 MRI Myelin Mapping Techniques

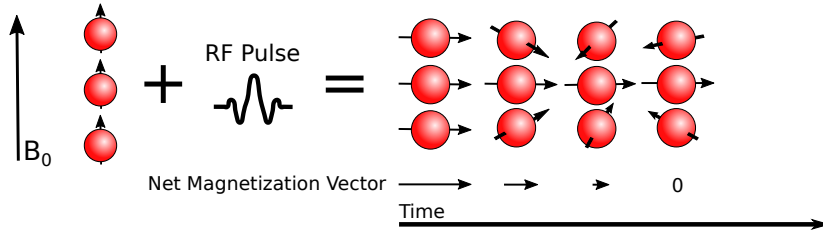
Myelin mapping can be performed using several different contrasts, each with their own benefits. Each of the relaxation mechanisms can be exploited in different ways to provide varying levels of intracortical contrast. For simplicity, they will be grouped into five categories: T_1 imaging (including R_1 and T_1W), T_2^* (including R_2^* and T_2^*W), T_1W/T_2W and composite maps, magnetization transfer (MT) imaging, and quantitative susceptibility mapping (QSM). The physical mechanisms driving individual contrasts with their representative MRI images are displayed in Figure 1.3.

T_2 imaging is also sensitive to myelin, but quantitative T_2 imaging has resolution limitations preventing it from being used for ICM mapping. This imaging is used in myelin water fraction imaging, where quantitative T_2 is used to extract information about the fast-relaxing water pool trapped in myelin (MacKay et al., 1994). However, myelin water fraction imaging is currently limited to WM studies due to the low resolution currently achievable. Additionally T_2W images are sensitive to myelination, but in practice are combined with other contrast images to generate ICM maps.

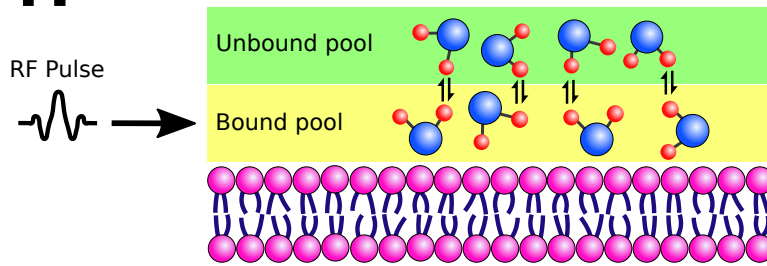
R1



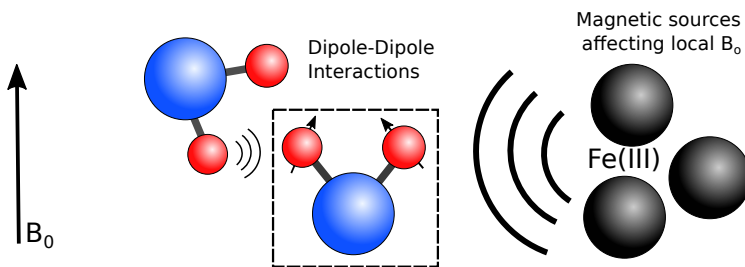
R2*



MT



QSM



MRI

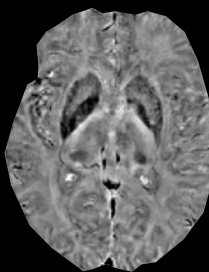
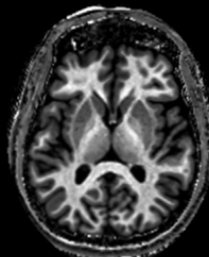
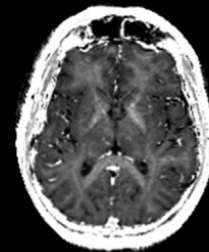
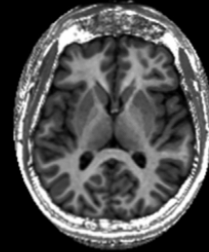


Figure 1.3: Illustration of primary mechanisms driving image contrasts used for ICM mapping (left), with resulting MRI images displayed on the right. R_1 describes the longitudinal relaxation of protons back to the main magnetic field, after being excited by an RF pulse. R_2^* contrast is derived from transverse relaxation generated from local field inhomogeneities altering the Larmor frequency of the protons. MT contrast results from a selective RF excitation of bound protons that exchange magnetization with protons in the unbound pool. Finally, QSM represents the changes in the local magnetic field driven largely by dipole-dipole interactions and magnetic sources within the tissue. MRI images are adapted from Callaghan et al., (2014) and Acosta-Cabronero et al., (2016).

1.3.2.1 T_1

T_1 contrast is primarily driven by myelin content, but is also susceptible to iron density (Desmond et al., 2016; Stüber et al., 2014). T_1 contrast has been used in numerous studies to study intracortical myelin, including the work presented in Chapters 2 and 3 of this thesis. Quantitative T_1 uses multiple inversion times to measure the average longitudinal relaxation rate within a voxel, whereas T_1W imaging uses only one inversion time to obtain a strong T_1 dependency of the signal from a voxel. Within the cortex, R_1 values ($1/T_1$) decreases monotonically across the cortical depth moving from WM to CSF (Marques, Khabipova, & Gruetter, 2017). R_1 has been shown to have lower intra- and intersubject variation and higher CNR relative to T_1W and T_2^* imaging (Haast, Ivanov, Formisano, & Uludag, 2016), suggesting its utility in studying structural changes within the cortex. Recently, multicomponent T_1 analysis has emerged, which may aid in differentiating the six cortical layers in human MRI while maintaining clinically relevant

scanning time (Lifshits et al., 2018). A technical consideration in ICM analysis is the resolution and scanner magnet strength used. It has been shown that T_1W scans at 3T at 0.8mm resolution provide similar information to higher resolution T_1 images at 7T and 0.5mm, however the higher resolution images provided further information about the cortical layers (Ferguson et al., 2018). This is important as it suggests new studies with high strength MRI and higher resolution should not provide conflicting findings from current previous studies performed below 7T.

Many quantitative T_1 mapping studies have been used to replicate early histological work to delineate cortical region boundaries. Previous studies have delineated sensory and motor cortices (Dinse et al., 2015), as well as localize primary auditory cortex (Dick et al., 2012) with quantitative T_1 . R_1 maps in visual cortex have been shown to share comparable borders in visual regions extracted from retinotopic maps derived from fMRI (Sereno, Lutti, Weiskopf, & Dick, 2013). These studies highlight the usefulness of T_1 imaging for defining potentially functionally significant cortical regions.

T_1 imaging has been combined with functional metrics aimed to correlate structure with function. Quantitative T_1 imaging combined with functional MRI has demonstrated a differential development of the area in visual cortex linked to facial recognition (Gomez et al., 2017), and delineation of various visual areas in the cortex (Dumoulin et al., 2017). Myelin levels predicted by both R_1 and MT in the anterior prefrontal cortex (PFC) have been correlated with a subject's confidence in their performance on a dot motion task (Allen et al., 2017). Functionally, R_1 values in the temporal lobe have correlated myelin

content, with a musician's ability to detect absolute pitch (Kim & Knösche, 2016). T_1 mapping combined with resting state fMRI revealed a link between areal functional connectivity and ICM levels (Huntenburg et al., 2017). From non-MRI functional data, myelin estimates from quantitative T_1 in the auditory cortex have been correlated with dipole moments from magnetoencephalography (Helbling et al., 2015). Combined, this work highlights the potential worth of combined functional and structural studies in mapping function across the cerebral cortex.

1.3.2.2 T_2^*

T_2^* ($1/R_2^*$) contrast has been shown to provide great intracortical contrast, however, these values can be affected by air-tissue and bone-tissue interfaces that cause B_0 inhomogeneities (Deistung et al., 2013). T_2^* values are also dependent on the orientation of fibers in relation to the main magnetic field (Cohen-Adad et al., 2012). It has been determined that there is a strong colocalization of R_2^* values, ICM and ferritin throughout the laminar profile of the cortex (Fukunaga et al., 2010). This iron and ICM colocalization is essential to make estimates of myelin changes, as the study also suggested that the changes in ferritin concentrations could be sufficient to explain changes in R_2^* signal (Fukunaga et al., 2010). R_2^* values correlate highly with iron maps in the cortex, while a linear relationship with iron and myelin concentrations best describes the signal (Stüber et al., 2014). High resolution T_2^* imaging in the visual cortex was found to provide better contrast to noise compared to a T_1W image (Sánchez-Panchuelo, Francis, Schluppeck, & Bowtell, 2011). Like R_1 imaging, R_2^* contrast

decreases monotonically from WM to the pial surface (Marques et al., 2017).

T_2^* values are dependent on cortical region, as they are significantly decreased in the PFC compared to the occipital cortex (Deistung et al., 2013), potentially reflecting the myelin content of those regions. An increase of R_2^* values with age was found in the supplementary motor cortex (Callaghan et al., 2014). Additionally, R_2^* has been shown to increase throughout most of the cortex in elderly subjects (64-75 years) compared to young adults (22-28 years) (Betts, Acosta-Cabronero, Cardenas-Blanco, Nestor, & Düzel, 2016). Phase shift maps derived from T_2W images revealed an increase in phase shift with age, in line with reports of cortical iron accumulation (Buijs et al., 2017). T_2^* has also been used to study disease, where decreases were found in amyotrophic lateral sclerosis patients in the motor cortex, which co-localized with increases in QSM (reviewed below) (Costagli et al., 2016). In a study of amyotrophic lateral sclerosis patients, changes in R_2^* was confirmed to be due to iron, and not myelin content based on combined *ex vivo* MRI and histology (Kwan et al., 2012).

1.3.2.3 T_1W/T_2W and Composite Maps

Multiple images of differing contrasts can be combined to study ICM. One method uses the ratio of T_1W/T_2W to increase the myelin-related contrast in the image while removing much of the bias field artifacts from the images (Glasser & Van Essen, 2011). The ratio has been shown to contain a higher intrasubject coefficient of variation, suggesting that it may not be as reliable as using the contrasts on their own with bias

correction (Haast et al., 2016). The bias correction is important, and will be reviewed further into the introduction.

Reports from T_1W/T_2W studies have described a linear relationship with age and ratio intensity from 18-35 years old, and this increase occurs primarily in the inner layers (Shafee, Buckner, & Fischl, 2015). Recently, the cortex was parcellated into 180 regions per hemisphere using the ratio image myelin map, combined with fMRI imaging in 210 subjects (Glasser et al., 2016). T_1W/T_2W myelin maps combined with functional resting state data showed a separation of the head and hand in sensory motor cortices, despite Brodmann labeling these areas as homogeneous (Kuehn et al., 2017). Combined T_1W/T_2W and functional imaging has indicated that the highly myelinated region in Heschl's gyrus can be defined and that it contained the regions responsible for primary auditory functions (De Martino et al., 2015). It has also been shown with a quantitative T_1 and R_2^* and its ratio, that there is a shared contrast mechanisms between these three imaging techniques (Kuehn et al., 2017). This finding may suggest that since differing contrast mechanisms are correlated, the contrast for a study may not need to be stringently chosen, due to the highly colocalized nature of iron and myelin (Fukunaga et al., 2010).

In addition to the T_1W/T_2W ratio contrast, combined myelin estimate maps have been constructed by combining multiple contrasts. This method utilizes independent component analysis to extract the “myelin signal” that is shared by both contrasts. The first component would explain the greatest variation explained by both contrasts, and this is suggested to be myelin (Mangeat, Govindarajan, Mainero, & Cohen-Adad, 2015).

Using MTR and T_2^* , the extracted myelin map displays adequate variation between primary cortical regions for parcellation (Mangeat et al., 2015). This methodology using quantitative T_1 and T_2^* images was used to correlate ICM levels and multiple sclerosis disease duration (Mangeat et al., 2018). This section demonstrates that multiple contrasts may be combined to increase image contrast and remove bias fields, but in turn, it may lead to the loss of the specificity of being able to attribute intensity changes to biological mechanisms.

1.3.2.4 Magnetization Transfer

MT contrast arises from the transfer of magnetization from “restricted” protons such as those that exist in macromolecules and bound water molecules to “free” protons in unbound water molecules (Wolff & Balaban, 1989). This method applies an off-resonant RF pulse to saturate macromolecular magnetization prior to an on-resonance excitation, and MT is the resulting reduction of image intensity (Helms, Dathe, Kallenberg, & Dechent, 2008). Magnetization transfer ratio (MTR) imaging attempts to qualitatively visualize the amount of this magnetization transfer between proton pools, while quantitative MT measurement approaches, including calculating MT saturation maps aim to remove the effects of longitudinal relaxation seen in MTR (Helms et al., 2008). Variations in quantitative MT values indicate differences in macromolecular content, and this is usually suggested to be myelin (Callaghan et al., 2014). In fact, a post mortem study found a high correlation between Luxol fast blue staining for myelin in WM and MTR values (Schmierer, Scaravilli, Altmann, Barker, & Miller, 2004). MTR has a high correlation with T_2^* , suggesting a common contrast mechanism (Mangeat et al.,

2015). Structurally, MT values have been shown to increase monotonically across the cortical depth, moving from CSF to WM (Whitaker et al., 2016). It has been shown to increase from 14-24 years of age (Whitaker et al., 2016), suggesting an increase in ICM. As age progresses, ICM decreases, and this was replicated using MT saturation where it was found to be negatively correlated with age from 19-75 years old (Callaghan et al., 2014). Like quantitative T_1 , MT and R_2^* values in the auditory cortex are correlated with magnetoencephalography recorded dipole moments (Helbling et al., 2015). Its application to study clinical populations has been exhibited in a study where a decrease in MTR in GM was correlated with multiple sclerosis disability scores (Fisniku et al., 2009). While not having been extensively used as of yet, MT has promise in the future of ICM studies as it has the potential to be more specific marker of myelin content.

1.3.2.5 Quantitative Susceptibility Mapping

QSM is the final ICM mapping contrast reviewed here and it arises from the diamagnetic properties of myelin and magnetic field perturbations caused by paramagnetic ions such as iron (Deistung et al., 2013). QSM images are generated by solving for the magnetic susceptibility using data from gradient echo sequences that provide phase data (Li, Wu, & Liu, 2011). QSM values change non-monotonically while moving from WM to GM, in contrast to monotonically changing R_1 and R_2^* values, which is likely due to the opposing effects of iron and myelin density (Marques et al., 2017). It was found that the main contributor to QSM contrast is iron (Deistung et al., 2013; Shmueli et al., 2009; Stüber et al., 2014). Additionally, QSM values demonstrated a

strong linear correlation with expected iron concentrations derived from a previous histological report (Costagli et al., 2016). QSM values are cortical region dependent, as it has been found that GM-WM contrast is inverted in frontal cortex compared to that of the occipital cortex (Deistung et al., 2013). Three images are generated in susceptibility-weighted imaging: magnitude, phase, and a calculated susceptibility-weighted image, with the later combining information from the magnitude and phase images to enhance contrast. When comparing the phase and magnitude images, it has been demonstrated that the magnitude images better report cortical structure relative to phase images likely due to phase image contrast is sensitive to structure orientation and B_0 inhomogeneities (Shmueli et al., 2009). Age-related increases in QSM values in elderly subjects was similar to those reported by R_2^* , except in visual cortices, where age-related increases were reduced in QSM (Betts et al., 2016). It has been suggested from QSM imaging of subcortical nuclei and the cortex, that GM iron increases with aging through adulthood (Acosta-Cabronero, Betts, Cardenas-Blanco, Yang, & Nestor, 2016). Functionally, QSM values in motor cortex have been found to correlate with impairment scores in amyotrophic lateral sclerosis, with increases in magnetic susceptibility found in disease patients (Costagli et al., 2016). Similar to MT, QSM has not been used as frequently as R_1 and R_2^* imaging for mapping ICM, but has been reported to hold promise to be combined with R_2^* to develop more specific estimations of iron and myelin changes in the cortex (Deistung et al., 2013).

1.3.3 Bias correction

Signal analysis in MRI relies heavily on the assumption that the signal is correlated with the underlying anatomy. Bias fields can have a strong effect on image intensities where one tissue class can have grossly different values depending on its location in the scanner bore and thus the image. Weighted-contrast imaging is more susceptible than quantitative imaging to these artifacts, but quantitative methods such as variable flip angle (VFA) T_1 mapping are still susceptible (Boudreau et al., 2017). These inhomogeneities are generated by the MR physics and hardware, and thus can be somewhat mitigated through quality assurance checks, and optimized hardware. Bias field inhomogeneities in the images can further be corrected *post hoc* (Belaroussi, Milles, Carne, Zhu, & Benoit-Cattin, 2006). Several algorithms exist to remove some of the B_1 shading in an image (Ahmed, Yamany, & Farag, 1999; C. Han, Hatsukami, & Yuan, 2001; Vovk, Pernu, & Likar, 2004; Weiskopf et al., 2011). One of the most popular algorithms is N3 Correction, which aims to find the smooth multiplicative field that maximizes the high frequency content of the image (Sled, Zijdenbos, & Evans, 1998). This has the advantage of not making assumptions about the underlying intensity of the images, but requires the input of the smoothness estimation of the field. This type of correction may inadvertently remove some of the ICM contrast as it smoothly varies across the cortex. More recent parametric corrections involve obtaining a B_1 transmit map at the time of subject imaging, and this will be discussed in the Future Directions section of **Chapter 5**. Finally, bias fields may also be removed to some extent by combining multiple images in order to cancel out the bias fields between images (Bock et al., 2013;

Glasser & Van Essen, 2011; Marques et al., 2010), which is the method that was employed in the work presented in this thesis.

1.4 Image Processing Techniques for Cerebral Cortex

Once a 3D volumetric MRI of the brain with good ICM contrast is obtained, it must be processed to map ICM features over the cortical surface. There are two approaches to this. The most direct is to map the myelin-related MR signal over the cortex. The second is to study how the thickness of the deeper myelinated layers in the cortex change. The work in this thesis began with thickness measure as techniques were unavailable at the time to robustly map the signal. Both of these methodologies begin the same way, with the definition of the WM and GM surfaces. An outline of landmarks in the processing pipeline are presented in Figure 1.4.

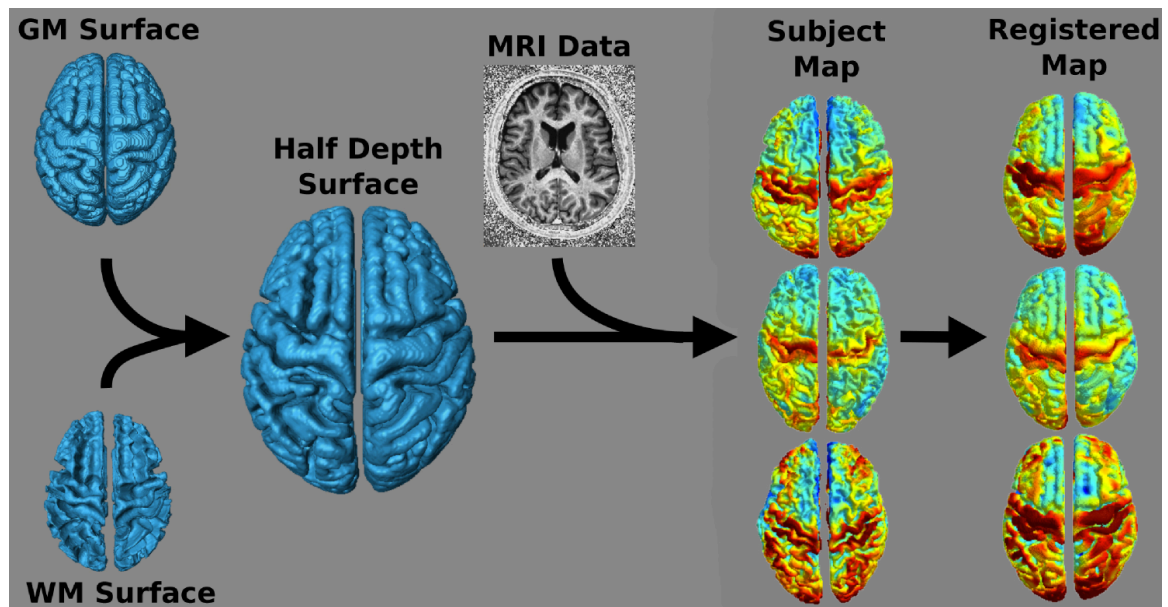


Figure 1.4: A visual representation of the processing pipeline of images for ICM mapping. Once the GM and WM surfaces have been defined for each subject, a half depth surface can be calculated. The corresponding MRI data values are then mapped to this surface. Finally, the surface is registered to a group template permitting vertex-wise statistical analysis.

1.4.1 Segmentation

The first step of any cortical analysis is the definition of the location of WM and GM tissues in the image. This can be performed manually, which has the limitations of lacking consistency and is very time consuming, making studies with a large number of subjects infeasible. Many different algorithms have been created to automatically perform this task such as FreeSurfer (Fischl, 2012), multiple object geometric deformable model (MGDM) (Bogovic, Prince, & Bazin, 2013), cortical reconstruction using implicit surface evolution (CRUISE) (X. Han et al., 2004) and robust fuzzy segmentation (Pham, 2001). The task of tissue segmentation is complicated by partial voluming of two or more tissue classes occupying a single voxel, noise, and by field inhomogeneities. Some algorithms are better than others at handling some of these issues, however, there is currently still a need to manually correct small errors generated by the algorithms. .

1.4.2 Defining Surfaces

The segmentation of the WM and GM tissue classes inherently provides the surfaces at the WM/GM and pial boundaries, although these are usually refined to estimate features that are unresolvable at the available resolution of the MRI. In order to

sample cortical thickness values, or MRI signal in the cortex, it can be useful to generate an intermediate surface between these two surfaces. Some studies have taken the approach of defining the surface a set distance into the GM from the WM (ex. (Grydeland, Walhovd, Tamnes, Westlye, & Fjell, 2013)). Waehnert et al (Waehnert et al., 2014) conducted an imaging study and determined that the layering of the cortex best followed a volume-preserving model through the gyri and sulci. Thus, using this volume-preserving model, the middle depth surface is more likely to sample the same cortical layer across the cortex. This is an important consideration in studies conducting group comparisons, as it is imperative that each subject's anatomy is being represented accurately.

1.4.3 Intersubject Registration for Group Analysis

The cerebral cortex is highly variable between individuals, both varying in size and shape. Being able to properly align the cortex between individuals is essential to make group-wise comparisons. Registrations typically work using a cost function, where deformations aim to produce the lowest “cost” or difference between two images. In volume-based registration, this calculation is performed over the entire brain and/or image (S. Klein, Staring, Murphy, Viergever, & Pluim, 2010). This can lead to inaccuracies in the registration of the cortex as the algorithm aims to provide the best fit over the entire image (A. Klein et al., 2009). Recent work on cortical processing has moved to surface-based registration. This improves cortical registration accuracy, as only the cortical surface is included in the calculation, and is thus not affected by other deformations that are apparent in the image, such as in subcortical structures (Ghosh et

al., 2010). As the cortex lacks boundaries to delineate functional areas, algorithms have added additional inputs for registration to improve intersubject alignment. Subject specific information such as curvature maps and image intensity maps can help improve alignment of the underlying cortical anatomy (Tardif et al., 2015).

1.7 Research Objectives and Overview

The overarching aim of this thesis was to develop methods for investigating intracortical myelin using MRI.

Chapter 2 aimed to expand on overall cortical thickness measurements in humans by separately investigating the thickness of just the heavily myelinated layers in the cortex. By using a clustering algorithm and optimized imaging, it was possible to separate the cortex into two depth portions based on their ICM content, whose thickness values can be separately reported. The applicability of the technique was then demonstrated in bipolar disorder, where it was shown that the more myelinated layers of the cortex are thinner in the dorsal lateral prefrontal cortex (DLPFC) relative to healthy controls.

Chapter 3 aimed to characterize age-related intracortical myelin trajectories in healthy humans from late adolescence to middle adulthood. The analysis framework in this chapter moved from volume to surface-based, and from thickness to signal analysis. The first adjustment was due to software techniques became available to perform surface-based registrations and analyses. The change to signal-based analysis was based on previous reports of the two metrics and how they follow aging. Cortical thickness has a very minor decreasing trend over all of adulthood (Fjell et al., 2009), which may have

been difficult to detect in a limited age range. This is in contrast to intracortical signal that shows a very strong correlation with age (Grydeland et al., 2013). While using a surface-based framework with signal analysis, we were able to show that intracortical T_1W signal follows a quadratic trajectory with age through middle adulthood. It was then possible to use the T_1W signal peaks of these trajectories to map developmental patterns over the cortex.

Finally, **Chapter 4** aimed to test the intracortical signal analysis method in a clinical population using non-optimized imaging. Without optimized imaging, the myelinated cortical thickness technique in Chapter 2 would not work due to the low contrast to noise ratio in the cortex. Thus I sought to conduct signal analysis on a T_1W/T_2W ratio; images that are commonly collected, and their ratio has been reported to generate a ‘myelin map’ (Glasser & Van Essen, 2011). The TRACK-HD dataset, which contains both of these image contrasts, was obtained for this analysis in Huntington’s disease. Due to previously reported increases in oligodendrocyte densities in HD, I hypothesized that a signal increase would be detected with disease progression. It was found that the middle cortical depth signal began to significantly increase in the cortex in the most severe disease group that was studied.

Taken together, this work highlights analytical frameworks for the examination of intracortical myelin through thickness and signal analysis. Additionally, the utility of the techniques was shown in charting cortical development and in exposing cortical changes in bipolar disorder as an example of a major mental disorder and in Huntington’s disease as an example of a neurodegenerative disorder.

References

- Acosta-Cabronero, J., Betts, M. J., Cardenas-Blanco, A., Yang, S., & Nestor, P. J. (2016). In Vivo MRI Mapping of Brain Iron Deposition across the Adult Lifespan. *Journal of Neuroscience*, *36*(2), 364–374. <http://doi.org/10.1523/JNEUROSCI.1907-15.2016>
- Ahmed, M. N., Yamany, S. M., & Farag, A. A. (1999). Bias field estimation and adaptive segmentation of MRI data using a modified fuzzy C-means algorithm. *Computer Vision and ...*, 250–255. http://doi.org/10.1109/CVPR.1999.786947&url_ctx_fmt=info:ofi/fmt:kev:mtx:ctx&rf t_val_fmt=info:ofi/fmt:kev:mtx:journal&rf t.atitle=Bias
- Allen, M., Glen, J. C., Müllensiefen, D., Schwarzkopf, D. S., Fardo, F., Frank, D., et al. (2017). Metacognitive ability correlates with hippocampal and prefrontal microstructure. *NeuroImage*, *149*, 415–423. <http://doi.org/10.1016/j.neuroimage.2017.02.008>
- Auer, F., Vagionitis, S., & Czopka, T. (2018). Evidence for Myelin Sheath Remodeling in the CNS Revealed by In Vivo Imaging. *Current Biology : CB*, *28*(4), 549–559.e3. <http://doi.org/10.1016/j.cub.2018.01.017>
- Belaroussi, B., Milles, J., Carme, S., Zhu, Y. M., & Benoit-Cattin, H. (2006). Intensity non-uniformity correction in MRI: Existing methods and their validation. *Medical Image Analysis*, *10*(2), 234–246. <http://doi.org/10.1016/j.media.2005.09.004>
- Betts, M. J., Acosta-Cabronero, J., Cardenas-Blanco, A., Nestor, P. J., & Düzel, E.

- (2016). High-resolution characterisation of the aging brain using simultaneous quantitative susceptibility mapping (QSM) and R2* measurements at 7T. *NeuroImage*, *138*, 43–63. <http://doi.org/10.1016/j.neuroimage.2016.05.024>
- Bock, N. A., Hashim, E., Janik, R., Konyer, N. B., Weiss, M., Stanisiz, G. J., et al. (2013). Optimizing T1-weighted imaging of cortical myelin content at 3.0T. *NeuroImage*, *65*, 1–12. <http://doi.org/10.1016/j.neuroimage.2012.09.051>
- Bogovic, J. A., Prince, J. L., & Bazin, P.-L. (2013). A Multiple Object Geometric Deformable Model for Image Segmentation. *Computer Vision and Image Understanding : CVIU*, *117*(2), 145–157. <http://doi.org/10.1016/j.cviu.2012.10.006>
- Boudreau, M., Tardif, C. L., Stikov, N., Sled, J. G., Lee, W., & Pike, G. B. (2017). B1 mapping for bias-correction in quantitative T1 imaging of the brain at 3T using standard pulse sequences. *Journal of Magnetic Resonance Imaging : JMRI*. <http://doi.org/10.1002/jmri.25692>
- Braitenberg, V. (1962). A note on myeloarchitectonics. *The Journal of Comparative Neurology*, *118*, 141–156.
- Brooks, R. A., Vymazal, J., Goldfarb, R. B., Bulte, J. W., & Aisen, P. (1998). Relaxometry and magnetometry of ferritin. *Magnetic Resonance in Medicine*, *40*(2), 227–235.
- Buijs, M., Doan, N. T., van Rooden, S., Versluis, M. J., van Lew, B., Milles, J., et al. (2017). In vivo assessment of iron content of the cerebral cortex in healthy aging using 7-Tesla T2*-weighted phase imaging. *Neurobiology of Aging*, *53*, 20–26.

<http://doi.org/10.1016/j.neurobiolaging.2016.09.005>

Callaghan, M. F., Freund, P., Draganski, B., Anderson, E., Cappelletti, M., Chowdhury, R., et al. (2014). Widespread age-related differences in the human brain microstructure revealed by quantitative magnetic resonance imaging. *Neurobiology of Aging*, 35(8), 1862–1872. <http://doi.org/10.1016/j.neurobiolaging.2014.02.008>

Ceckler, T. L., Wolff, S. D., Yip, V., Simon, S. A., & Balaban, R. S. (1992). Dynamic and chemical factors affecting water proton relaxation by macromolecules. *Journal of Magnetic Resonance*, (98), 637–645.

Cohen-Adad, J., Polimeni, J. R., Helmer, K. G., Benner, T., McNab, J. A., Wald, L. L., et al. (2012). T_2^* mapping and B_0 orientation-dependence at 7 T reveal cyto- and myeloarchitecture organization of the human cortex. *NeuroImage*, 60(2), 1006–1014. <http://doi.org/10.1016/j.neuroimage.2012.01.053>

Costagli, M., Donatelli, G., Biagi, L., Ienco, E. C., Siciliano, G., Tosetti, M., & Cosottini, M. (2016). Magnetic susceptibility in the deep layers of the primary motor cortex in Amyotrophic Lateral Sclerosis. *NeuroImage. Clinical*, 12(C), 965–969. <http://doi.org/10.1016/j.nicl.2016.04.011>

De Martino, F., Moerel, M., Xu, J., van de Moortele, P.-F., Ugurbil, K., Goebel, R., et al. (2015). High-Resolution Mapping of Myeloarchitecture In Vivo: Localization of Auditory Areas in the Human Brain. *Cerebral Cortex*, 25(10), 3394–3405. <http://doi.org/10.1093/cercor/bhu150>

Deistung, A., Schäfer, A., Schweser, F., Biedermann, U., Turner, R., & Reichenbach, J.

- R. (2013). Toward in vivo histology: a comparison of quantitative susceptibility mapping (QSM) with magnitude-, phase-, and R2*-imaging at ultra-high magnetic field strength. *NeuroImage*, *65*, 299–314.
<http://doi.org/10.1016/j.neuroimage.2012.09.055>
- Desmond, K. L., Al-Ebraheem, A., Janik, R., Oakden, W., Kwiecien, J. M., Dabrowski, W., et al. (2016). Differences in iron and manganese concentration may confound the measurement of myelin from R1 and R2 relaxation rates in studies of dysmyelination. *NMR in Biomedicine*, *29*(7), 985–998. <http://doi.org/10.1002/nbm.3549>
- Dick, F., Taylor Tierney, A., Lutti, A., Josephs, O., Sereno, M. I., & Weiskopf, N. (2012). In Vivo Functional and Myeloarchitectonic Mapping of Human Primary Auditory Areas. *Journal of Neuroscience*, *32*(46), 16095–16105.
<http://doi.org/10.1523/JNEUROSCI.1712-12.2012>
- Dinse, J., Härtwich, N., Waehnert, M. D., Tardif, C. L., Schäfer, A., Geyer, S., et al. (2015). A cytoarchitecture-driven myelin model reveals area-specific signatures in human primary and secondary areas using ultra-high resolution in-vivo brain MRI. *NeuroImage*, *114*(C), 71–87. <http://doi.org/10.1016/j.neuroimage.2015.04.023>
- Dumoulin, S. O., Ben M Harvey, Fracasso, A., Zuiderbaan, W., Luijten, P. R., Wandell, B. A., & Petridou, N. (2017). In vivo evidence of functional and anatomical stripe-based subdivisions in human V2 and V3. *Scientific Reports*, 1–12.
<http://doi.org/10.1038/s41598-017-00634-6>
- Einheber, S., Bhat, M. A., & Salzer, J. L. (2006). Disrupted axo-glial junctions result in

accumulation of abnormal mitochondria at nodes of ranvier. *Neuron Glia Biology*, 2(3), 165–174. <http://doi.org/10.1017/S1740925X06000275>

Ferguson, B., Petridou, N., Fracasso, A., Heuvel, M. P., Brouwer, R. M., Pol, H. E. H., et al. (2018). Detailed T1-Weighted Profiles from the Human Cortex Measured in Vivo at 3 Tesla MRI, 1–16. <http://doi.org/10.1007/s12021-018-9356-2>

Fischl, B. (2012). FreeSurfer. *NeuroImage*, 62(2), 774–781. <http://doi.org/10.1016/j.neuroimage.2012.01.021>

Fish, J. L., Dehay, C., Kennedy, H., & Huttner, W. B. (2008). Making bigger brains-the evolution of neural-progenitor-cell division. *Journal of Cell Science*, 121(17), 2783–2793. <http://doi.org/10.1242/jcs.023465>

Fisniku, L. K., Altmann, D. R., Cercignani, M., Tozer, D. J., Chard, D. T., Jackson, J. S., et al. (2009). Magnetization transfer ratio abnormalities reflect clinically relevant grey matter damage in multiple sclerosis. *Multiple Sclerosis Journal*, 15(6), 668–677. <http://doi.org/10.1177/1352458509103715>

Fjell, A. M., Westlye, L. T., Amlie, I., Espeseth, T., Reinvang, I., Raz, N., et al. (2009). High Consistency of Regional Cortical Thinning in Aging across Multiple Samples. *Cerebral Cortex*, 19(9), 2001–2012. <http://doi.org/10.1093/cercor/bhn232>

Fukunaga, M., Li, T. Q., van Gelderen, P., de Zwart, J. A., Shmueli, K., Yao, B., et al. (2010). Layer-specific variation of iron content in cerebral cortex as a source of MRI contrast. *Proceedings of the National Academy of Sciences of the United States of America*, 107(8), 3834–3839. <http://doi.org/10.1073/pnas.0911177107>

Fünfschilling, U., Supplie, L. M., Mahad, D., Boretius, S., Saab, A. S., Edgar, J., et al.

(2013). Glycolytic oligodendrocytes maintain myelin and long-term axonal integrity.

Nature, 485(7399), 517–521. <http://doi.org/10.1038/nature11007>

Ghosh, S. S., Kakunoori, S., Augustinack, J., Nieto-Castanon, A., Kovelman, I., Gaab, N.,

et al. (2010). Evaluating the validity of volume-based and surface-based brain image

registration for developmental cognitive neuroscience studies in children 4 to 11 years

of age. *NeuroImage*, 53(1), 85–93. <http://doi.org/10.1016/j.neuroimage.2010.05.075>

Gibson, E. M., Purger, D., Mount, C. W., Goldstein, A. K., Lin, G. L., Wood, L. S., et al.

(2014). Neuronal activity promotes oligodendrogenesis and adaptive myelination in

the mammalian brain. *Science (New York, N.Y.)*, 344(6183), 1252304–1252304.

<http://doi.org/10.1126/science.1252304>

Glasser, M. F., & Van Essen, D. C. (2011). Mapping Human Cortical Areas In Vivo

Based on Myelin Content as Revealed by T1- and T2-Weighted MRI. *Journal of*

Neuroscience, 31(32), 11597–11616. <http://doi.org/10.1523/JNEUROSCI.2180->

11.2011

Glasser, M. F., Coalson, T. S., Robinson, E. C., Hacker, C. D., Harwell, J., Yacoub, E., et

al. (2016). A multi-modal parcellation of human cerebral cortex. *Nature*, 536(7615),

171–178. <http://doi.org/10.1038/nature18933>

Gomez, J., Barnett, M. A., Natu, V., Mezer, A., Palomero-Gallagher, N., Weiner, K. S., et

al. (2017). Microstructural proliferation in human cortex is coupled with the

development of face processing. *Science (New York, N.Y.)*, 355(6320), 68–71.

<http://doi.org/10.1126/science.aag0311>

Grydeland, H., Walhovd, K. B., Tamnes, C. K., Westlye, L. T., & Fjell, A. M. (2013).

Intracortical Myelin Links with Performance Variability across the Human Lifespan: Results from T1- and T2-Weighted MRI Myelin Mapping and Diffusion Tensor Imaging. *Journal of Neuroscience*, *33*(47), 18618–18630.

<http://doi.org/10.1523/JNEUROSCI.2811-13.2013>

Haast, R. A. M., Ivanov, D., Formisano, E., & Uludag, K. (2016). Reproducibility and

Reliability of Quantitative and Weighted T1 and T2* Mapping for Myelin-Based Cortical Parcellation at 7 Tesla. *Frontiers in Neuroanatomy*, *10*(710), 1–17.

<http://doi.org/10.3389/fnana.2016.00112>

Han, C., Hatsukami, T. S., & Yuan, C. (2001). A multi-scale method for automatic

correction of intensity non-uniformity in MR images. *Journal of Magnetic Resonance Imaging : JMRI*, *13*(3), 428–436.

Han, X., Pham, D. L., Tosun, D., Rettmann, M. E., Xu, C., & Prince, J. L. (2004).

CRUISE: Cortical reconstruction using implicit surface evolution. *NeuroImage*, *23*(3), 997–1012. <http://doi.org/10.1016/j.neuroimage.2004.06.043>

Harris, J. J., & Attwell, D. (2012). The Energetics of CNS White Matter. *Journal of*

Neuroscience, *32*(1), 356–371. <http://doi.org/10.1523/JNEUROSCI.3430-11.2012>

Helbling, S., Teki, S., Callaghan, M. F., Sedley, W., Mohammadi, S., Griffiths, T. D., et

al. (2015). Structure predicts function: Combining non-invasive electrophysiology with in-vivo histology. *NeuroImage*, *108*(C), 377–385.

<http://doi.org/10.1016/j.neuroimage.2014.12.030>

Helms, G., Dathe, H., Kallenberg, K., & Dechent, P. (2008). High-resolution maps of magnetization transfer with inherent correction for RF inhomogeneity and T1

relaxation obtained from 3D FLASH MRI. *Magnetic Resonance in Medicine*, *60*(6),

1396–1407. <http://doi.org/10.1002/mrm.21732>

Huntenburg, J. M., Bazin, P.-L., Goulas, A., Tardif, C. L., Villringer, A., & Margulies, D.

S. (2017). A Systematic Relationship Between Functional Connectivity and

Intracortical Myelin in the Human Cerebral Cortex. *Cerebral Cortex*, *27*(2), 981–997.

<http://doi.org/10.1093/cercor/bhx030>

Huxley, A. F., & Stämpfli, R. (1949). Evidence for saltatory conduction in peripheral myelinated nerve fibres. *The Journal of Physiology*, *108*(3), 315–339.

[http://doi.org/10.1111/\(ISSN\)1469-7793](http://doi.org/10.1111/(ISSN)1469-7793)

Jalil, M. A., Begum, L., Contreras, L., Pardo, B., Iijima, M., Li, M. X., et al. (2005).

Reduced N-Acetylaspartate Levels in Mice Lacking Aralar, a Brain- and Muscle-type

Mitochondrial Aspartate-glutamate Carrier. *Journal of Biological Chemistry*,

280(35), 31333–31339. <http://doi.org/10.1074/jbc.M505286200>

Kim, S.-G., & Knösche, T. R. (2016). Intracortical myelination in musicians with

absolute pitch: Quantitative morphometry using 7-T MRI. *Human Brain Mapping*,

37(10), 3486–3501. <http://doi.org/10.1002/hbm.23254>

Klein, A., Andersson, J., Ardekani, B. A., Ashburner, J., Avants, B., Chiang, M.-C., et al.

(2009). Evaluation of 14 nonlinear deformation algorithms applied to human brain

MRI registration. *NeuroImage*, 46(3), 786–802.

<http://doi.org/10.1016/j.neuroimage.2008.12.037>

Klein, S., Staring, M., Murphy, K., Viergever, M. A., & Pluim, J. P. W. (2010). elastix: a toolbox for intensity-based medical image registration. *IEEE Transactions on Medical Imaging*, 29(1), 196–205. <http://doi.org/10.1109/TMI.2009.2035616>

Medical Imaging, 29(1), 196–205. <http://doi.org/10.1109/TMI.2009.2035616>

Kuehn, E., Dinse, J., Jakobsen, E., Long, X., Schäfer, A., Bazin, P.-L., et al. (2017). Body

Topography Parcellates Human Sensory and Motor Cortex. *Cerebral Cortex*, 27(7),

3790–3805. <http://doi.org/10.1093/cercor/bhx026>

Kwan, J. Y., Jeong, S. Y., van Gelderen, P., Deng, H.-X., Quezado, M. M., Danielian, L.

E., et al. (2012). Iron Accumulation in Deep Cortical Layers Accounts for MRI

Signal Abnormalities in ALS: Correlating 7 Tesla MRI and Pathology. *PLoS ONE*,

7(4), e35241–9. <http://doi.org/10.1371/journal.pone.0035241>

Lashley, K. S., & Clark, G. (1946). The cytoarchitecture of the cerebral cortex of Ateles;

a critical examination of architectonic studies. *The Journal of Comparative*

Neurology, 85(2), 223–305.

Lee, Y., Morrison, B. M., Li, Y., Lengacher, S., Farah, M. H., Hoffman, P. N., et al.

(2013). Oligodendroglia metabolically support axons and contribute to

neurodegeneration. *Nature*, 487(7408), 443–448. <http://doi.org/10.1038/nature11314>

Li, W., Wu, B., & Liu, C. (2011). Quantitative susceptibility mapping of human brain

reflects spatial variation in tissue composition. *NeuroImage*, 55(4), 1645–1656.

<http://doi.org/10.1016/j.neuroimage.2010.11.088>

- Lifshits, S., Tomer, O., Shamir, I., Barazany, D., Tsarfaty, G., Rosset, S., & Assaf, Y. (2018). Resolution considerations in imaging of the cortical layers. *NeuroImage*, *164*, 112–120. <http://doi.org/10.1016/j.neuroimage.2017.02.086>
- Lillie, R. S. (1925). Factors Affecting Transmission and Recovery in the Passive Iron Model. *The Journal of General Physiology*, *7*(4), 473–507.
- MacKay, A., Whittall, K., Adler, J., Li, D., Paty, D., & Graeb, D. (1994). In vivo visualization of myelin water in brain by magnetic resonance. *Magnetic Resonance in Medicine*, *31*(6), 673–677.
- Mangeat, G., Badji, A., Ouellette, R., Treaba, C. A., Herranz, E., Granberg, T., et al. (2018). Changes in structural network are associated with cortical demyelination in early multiple sclerosis. *Human Brain Mapping*, *99*(2), 509–14. <http://doi.org/10.1002/hbm.23993>
- Mangeat, G., Govindarajan, S. T., Mainero, C., & Cohen-Adad, J. (2015). Multivariate combination of magnetization transfer, T2* and B0 orientation to study the myeloarchitecture of the in vivo human cortex. *NeuroImage*, *119*(C), 89–102. <http://doi.org/10.1016/j.neuroimage.2015.06.033>
- Marques, J. P., Khabipova, D., & Gruetter, R. (2017). Studying cyto and myeloarchitecture of the human cortex at ultra-high field with quantitative imaging: R1, R2* and magnetic susceptibility. *NeuroImage*, *147*(C), 152–163. <http://doi.org/10.1016/j.neuroimage.2016.12.009>
- Marques, J. P., Kober, T., Krueger, G., van der Zwaag, W., van de Moortele, P.-F., &

- Gruetter, R. (2010). MP2RAGE, a self bias-field corrected sequence for improved segmentation and T1-mapping at high field. *NeuroImage*, *49*(2), 1271–1281.
<http://doi.org/10.1016/j.neuroimage.2009.10.002>
- Marta, C. B., Paez, P., Lopez, M., Pellegrino de Iraldi, A., Soto, E. F., & Pasquini, J. M. (2003). Morphological changes of myelin sheaths in rats intracranially injected with apotransferrin. *Neurochemical Research*, *28*(1), 101–110.
- McRobbie, D. W., Moore, E. A., Graves, M. J., & Prince, M. R. (2009). MRI From Picture to Proton (2nd ed., pp. 1–406). Cambridge: Cambridge University Press.
<http://doi.org/10.1017/CBO9780511545405>
- Morrison, B. M., Lee, Y., & Rothstein, J. D. (2013). Oligodendroglia: metabolic supporters of axons. *Trends in Cell Biology*, *23*(12), 644–651.
<http://doi.org/10.1016/j.tcb.2013.07.007>
- Mountcastle, V. B. (1997). The columnar organization of the neocortex. *Brain*, *120* (Pt 4), 701–722.
- Nave, K.-A. (2010). Myelination and the trophic support of long axons, 1–9.
<http://doi.org/10.1038/nrn2797>
- Nieuwenhuys, R. (2012). The myeloarchitectonic studies on the human cerebral cortex of the Vogt–Vogt school, and their significance for the interpretation of functional neuroimaging data. *Brain Structure and Function*, *218*(2), 303–352.
<http://doi.org/10.1007/s00429-012-0460-z>
- Pelvig, D. P., Pakkenberg, H., Stark, A. K., & Pakkenberg, B. (2008). Neocortical glial

cell numbers in human brains. *Neurobiology of Aging*, 29(11), 1754–1762.

<http://doi.org/10.1016/j.neurobiolaging.2007.04.013>

Pham, D. L. (2001). Robust fuzzy segmentation of magnetic resonance images.

Computer-Based Medical Systems.

Sánchez, I., Hassinger, L., Paskevich, P. A., Shine, H. D., & Nixon, R. A. (1996).

Oligodendroglia regulate the regional expansion of axon caliber and local accumulation of neurofilaments during development independently of myelin formation. *Journal of Neuroscience*, 16(16), 5095–5105.

Sánchez-Panchuelo, R. M., Francis, S. T., Schluppeck, D., & Bowtell, R. W. (2011).

Correspondence of human visual areas identified using functional and anatomical MRI in vivo at 7 T. *Journal of Magnetic Resonance Imaging : JMRI*, 35(2), 287–299.

<http://doi.org/10.1002/jmri.22822>

Schmierer, K., Scaravilli, F., Altmann, D. R., Barker, G. J., & Miller, D. H. (2004).

Magnetization transfer ratio and myelin in postmortem multiple sclerosis brain.

Annals of Neurology, 56(3), 407–415. <http://doi.org/10.1002/ana.20202>

Schmued, L. C. (1990). A rapid, sensitive histochemical stain for myelin in frozen brain

sections. *The Journal of Histochemistry and Cytochemistry : Official Journal of the Histochemistry Society*, 38(5), 717–720. <http://doi.org/10.1177/38.5.1692056>

Schwab, M. E., & Schnell, L. (1991). Channeling of developing rat corticospinal tract

axons by myelin-associated neurite growth inhibitors. *Journal of Neuroscience*, 11(3), 709–721.

- Seidl, A. H. (2014). Regulation of conduction time along axons. *Neuroscience*, 276, 126–134. <http://doi.org/10.1016/j.neuroscience.2013.06.047>
- Sereno, M. I., Lutti, A., Weiskopf, N., & Dick, F. (2013). Mapping the Human Cortical Surface by Combining Quantitative T1 with Retinotopy. *Cerebral Cortex*, 23(9), 2261–2268. <http://doi.org/10.1093/cercor/bhs213>
- Shafee, R., Buckner, R. L., & Fischl, B. (2015). Gray matter myelination of 1555 human brains using partial volume corrected MRI images. *NeuroImage*, 105(C), 473–485. <http://doi.org/10.1016/j.neuroimage.2014.10.054>
- Shmueli, K., de Zwart, J. A., van Gelderen, P., Li, T.-Q., Dodd, S. J., & Duyn, J. H. (2009). Magnetic susceptibility mapping of brain tissue in vivo using MRI phase data. *Magnetic Resonance in Medicine*, 62(6), 1510–1522. <http://doi.org/10.1002/mrm.22135>
- Saini, S., Frankel, R. B., Stark, D. D., & Ferrucci, J. T. (1988). Magnetism: a primer and review. *AJR. American Journal of Roentgenology*, 150(4), 735–743. <http://doi.org/10.2214/ajr.150.4.735>
- Sled, J. G., Zijdenbos, A. P., & Evans, A. C. (1998). A nonparametric method for automatic correction of intensity nonuniformity in MRI data. *IEEE Transactions on ...*, 17(1), 87–97. http://doi.org/10.1109/42.668698&url_ctx_fmt=info:ofi/fmt:kev:mtx:ctx&rft_val_fmt=info:ofi/fmt:kev:mtx:journal&rft.atitle=A
- Stanisz, G. J., Odobina, E. E., Pun, J., Escaravage, M., Graham, S. J., Bronskill, M. J., &

- Henkelman, R. M. (2005). T1, T2 relaxation and magnetization transfer in tissue at 3T. *Magnetic Resonance in Medicine*, *54*(3), 507–512.
<http://doi.org/10.1002/mrm.20605>
- Stüber, C., Morawski, M., Schäfer, A., Labadie, C., Wähnert, M., Leuze, C., et al. (2014). Myelin and iron concentration in the human brain: A quantitative study of MRI contrast. *NeuroImage*, *93*, 95–106. <http://doi.org/10.1016/j.neuroimage.2014.02.026>
- Tardif, C. L., Schäfer, A., Waehnert, M., Dinse, J., Turner, R., & Bazin, P.-L. (2015). Multi-contrast multi-scale surface registration for improved alignment of cortical areas. *NeuroImage*, *111*(C), 107–122.
<http://doi.org/10.1016/j.neuroimage.2015.02.005>
- Triarhou, L. C. (2007). The Economo-Koskinas atlas revisited: cytoarchitectonics and functional context. *Stereotactic and functional neurosurgery* (Vol. 85, pp. 195–203). Karger Publishers. <http://doi.org/10.1159/000103258>
- Tubridy, N., & McKinsty, C. S. (2000). Neuroradiological history: Sir Joseph Larmor and the basis of MRI physics. *Neuroradiology*, *42*(11), 852–855.
- Vovk, U., Pernu, F., & Likar, B. T. (2004). MRI intensity inhomogeneity correction by combining intensity and spatial information. *Physics in Medicine and Biology*, *49*(17), 4119–4133. <http://doi.org/10.1088/0031-9155/49/17/020>
- Vymazal, J., Brooks, R. A., Patronas, N., Hajek, M., Bulte, J. W., & Di Chiro, G. (1995). Magnetic resonance imaging of brain iron in health and disease. *Journal of the Neurological Sciences*, *134 Suppl*, 19–26.

- Waehnert, M. D., Dinse, J., Weiss, M., Streicher, M. N., Waehnert, P., Geyer, S., et al. (2014). Anatomically motivated modeling of cortical laminae. *NeuroImage*, *93*(P2), 210–220. <http://doi.org/10.1016/j.neuroimage.2013.03.078>
- Weiskopf, N., Lutti, A., Helms, G., Novak, M., Ashburner, J., & Hutton, C. (2011). Unified segmentation based correction of R1 brain maps for RF transmit field inhomogeneities (UNICORT). *NeuroImage*, *54*(3), 2116–2124. <http://doi.org/10.1016/j.neuroimage.2010.10.023>
- Whitaker, K. J., Vértes, P. E., Romero-Garcia, R., Váša, F., Moutoussis, M., Prabhu, G., et al. (2016). Adolescence is associated with genomically patterned consolidation of the hubs of the human brain connectome. *Proceedings of the National Academy of Sciences*, *113*(32), 9105–9110. <http://doi.org/10.1073/pnas.1601745113>
- Wolff, S. D., & Balaban, R. S. (1989). Magnetization transfer contrast (MTC) and tissue water proton relaxation in vivo. *Magnetic Resonance in Medicine*, *10*(1), 135–144.
- Xiao, L., Ohayon, D., McKenzie, I. A., Sinclair-Wilson, A., Wright, J. L., Fudge, A. D., et al. (2016). Rapid production of new oligodendrocytes is required in the earliest stages of motor-skill learning. *Nature Neuroscience*, *19*(9), 1210–1217. <http://doi.org/10.1038/nn.4351>
- Zilles, K., & Amunts, K. (2010). Centenary of Brodmann's map — conception and fate, *11*(2), 139–145. <http://doi.org/10.1038/nrn2776>

Chapter 2: Assessing intracortical myelin in the living human brain using myelinated cortical thickness

Preamble

Bipolar disorder (BD) is characterized by cyclical periods of depression and mania, with periods of euthymia in between. Despite roughly 4% of the population experiencing BD (Kessler et al., 2005), the biological mechanisms underlying the disorder are unknown. Due to the distinctive interchanging of mood states in the disorder, it has lead researchers to investigate the prefrontal cortex (PFC) due to its involvement in mood and cognition. Histological reports in this area of the brain have since implicated myelin with BD.

Myelin plays a critical role in the development, maintenance and functioning of neural circuits, so its feasible that it may be impaired in mood disorders such as BD. Cortical glial cells (Ongür, Drevets, & Price, 1998; Rajkowska, Halaris, & Selemon, 2001) and specifically oligodendrocytes (Uranova:2004hq, (Uranova et al., 2001) have been found in decreased densities in the PFC in BD in *post mortem* histology work. Additionally there has been found to be a decrease in the expression of oligodendrocyte and myelin-related genes in BD (Tkachev et al., 2003). *In vivo*, MRI studies have demonstrated the cortical involvement in BD where decreases in cortical thickness have been found (Elvsåshagen et al., 2013; Foland-Ross et al., 2011; Lyoo et al., 2006; Oertel-Knöchel et al., 2015). Currently, it is unknown as to whether the structural deficits in

myelin are a cause or an effect of the disorder, but its involvement makes it a candidate to be used as a proxy to study the progression of the disorder.

As myelin is disrupted in BD and as myelin aids in the metabolics of cell signaling, BD subjects could also exhibit abnormal brain metabolism. Indeed, numerous studies have demonstrated decreased brain metabolism in the frontal cortex of patients with bipolar disorder. A reduction in metabolism has been found in the orbital frontal cortex of BD patients during manic episodes (Blumberg et al., 1999). Lowered metabolic rates have also been reported in BD during episodes of depression (Baxter et al., 1989; Drevets et al., 1997). These decreases are also found in euthymic patients (Deicken, Fein, & Weiner, 1995). Together this evidence suggests that the brain's metabolism is compromised during all mental states in BD, which may be related to underlying structural changes.

With the structure and metabolism of the cortex in BD compromised, it would be expected that patients would display cognitive deficits. It has been shown that BD patients experience deficits across multiple cognitive domains during all mood states of the disorder (Martínez-Arán et al., 2004). A worsening of verbal memory scores have been correlated with duration of BD, the number of previous manic episodes, hospitalization and suicide attempts (Martínez-Arán et al., 2004). Additionally, it has been seen that patients that experience psychosis have worse cognitive scores (Simonsen et al., 2011). Also processing speed has been found to predict social functionality in BD (Burdick, Goldberg, & Harrow, 2010). Combined, all of these findings suggest how

myelin deficits could progress to produce cognitive deficits. Thus studying ICM in BD may lead to an understanding of the biological mechanisms underlying the disorder.

This Chapter presents the first *in vivo* indication that ICM may be implicated in BD using a novel technique for investigating ICM. These results paved the way for additional studies in our lab on ICM and BD including: a histology study (Lake et al., 2016), a larger study on ICM and BD where I was co-first author (Sehmbi, Rowley, Minuzzi, Kapczinski, Kwiecien, et al., 2018a), and a study on the correlation of ICM and cognition in BD (Sehmbi, Rowley, Minuzzi, Kapczinski, Steiner, et al., 2018b).

References

- Baxter, L. R., Schwartz, J. M., Phelps, M. E., Mazziotta, J. C., Guze, B. H., Selin, C. E., et al. (1989). Reduction of prefrontal cortex glucose metabolism common to three types of depression. *Archives of General Psychiatry*, *46*(3), 243–250.
- Blumberg, H. P., Stern, E., Ricketts, S., Martinez, D., de Asis, J., White, T., et al. (1999). Rostral and orbital prefrontal cortex dysfunction in the manic state of bipolar disorder. *American Journal of Psychiatry*, *156*(12), 1986–1988.
<http://doi.org/10.1176/ajp.156.12.1986>
- Burdick, K. E., Goldberg, J. F., & Harrow, M. (2010). Neurocognitive dysfunction and psychosocial outcome in patients with bipolar I disorder at 15-year follow-up. *Acta Psychiatrica Scandinavica*, *122*(6), 499–506. <http://doi.org/10.1111/j.1600-0447.2010.01590.x>

Deicken, R. F., Fein, G., & Weiner, M. W. (1995). Abnormal frontal lobe phosphorous metabolism in bipolar disorder. *American Journal of Psychiatry*, *152*(6), 915–918.

<http://doi.org/10.1176/ajp.152.6.915>

Drevets, W. C., Price, J. L., Simpson, J. R., Todd, R. D., Reich, T., Vannier, M., & Raichle, M. E. (1997). Subgenual prefrontal cortex abnormalities in mood disorders.

Nature, *386*(6627), 824–827. <http://doi.org/10.1038/386824a0>

Elvsåshagen, T., Westlye, L. T., Bøen, E., Hol, P. K., Andreassen, O. A., Boye, B., & Malt, U. F. (2013). Bipolar II disorder is associated with thinning of prefrontal and

temporal cortices involved in affect regulation. *Bipolar Disorders*, *15*(8), 855–864.

<http://doi.org/10.1111/bdi.12117>

Foland-Ross, L. C., Thompson, P. M., Sugar, C. A., Madsen, S. K., Shen, J. K., Penfold, C., et al. (2011). Investigation of cortical thickness abnormalities in lithium-free adults with bipolar I disorder using cortical pattern matching. *The American Journal of Psychiatry*, *168*(5), 530–539.

<http://doi.org/10.1176/appi.ajp.2010.10060896>

Kessler, R. C., Berglund, P., Demler, O., Jin, R., Merikangas, K. R., & Walters, E. E.

(2005). Lifetime prevalence and age-of-onset distributions of DSM-IV disorders in the National Comorbidity Survey Replication. *Archives of General Psychiatry*, *62*(6),

593–602. <http://doi.org/10.1001/archpsyc.62.6.593>

Lake, E. M. R., Steffler, E. A., Rowley, C. D., Sehmbi, M., Minuzzi, L., Frey, B. N., &

Bock, N. A. (2016). Altered intracortical myelin staining in the dorsolateral prefrontal

cortex in severe mental illness. *European Archives of Psychiatry and Clinical Neuroscience*, 1–8. <http://doi.org/10.1007/s00406-016-0730-5>

Lyoo, I. K., Sung, Y. H., Dager, S. R., Friedman, S. D., Lee, J.-Y., Kim, S. J., et al.

(2006). Regional cerebral cortical thinning in bipolar disorder. *Bipolar Disorders*, 8(1), 65–74. <http://doi.org/10.1111/j.1399-5618.2006.00284.x>

Martínez-Arán, A., Vieta, E., Reinares, M., Colom, F., Torrent, C., Sanchez-Moreno, J.,

et al. (2004). Cognitive function across manic or hypomanic, depressed, and euthymic states in bipolar disorder. *American Journal of Psychiatry*, 161(2), 262–270. <http://doi.org/10.1176/appi.ajp.161.2.262>

Oertel-Knöchel, V., Reuter, J., Reinke, B., Marbach, K., Feddern, R., Alves, G., et al.

(2015). Association between age of disease-onset, cognitive performance and cortical thickness in bipolar disorders. *Journal of Affective Disorders*, 174(C), 627–635. <http://doi.org/10.1016/j.jad.2014.10.060>

Ongür, D., Drevets, W. C., & Price, J. L. (1998). Glial reduction in the subgenual

prefrontal cortex in mood disorders. *Proceedings of the National Academy of Sciences*, 95(22), 13290–13295.

Rajkowska, G., Halaris, A., & Selemon, L. D. (2001). Reductions in neuronal and glial

density characterize the dorsolateral prefrontal cortex in bipolar disorder. *Biological Psychiatry*, 49(9), 741–752.

Sehmbi, M., Rowley, C. D., Minuzzi, L., Kapczynski, F., Kwiecien, J., Bock, N. A., &

- Frey, B. N. (2018a). Deficits in intracortical myelination in young adults with Bipolar I Disorder. *Journal of Psychiatry and Neuroscience*. In Revision.
- Sehmbi, M., Rowley, C. D., Minuzzi, L., Kapczinski, F., Steiner, M., Sassi, R. B., et al. (2018b). Association of intracortical myelin and cognitive function in bipolar I disorder. *Acta Psychiatrica Scandinavica*, *161*, 262–11. <http://doi.org/10.1111/acps.12875>
- Simonsen, C., Sundet, K., Vaskinn, A., Birkenaes, A. B., Engh, J. A., Faerden, A., et al. (2011). Neurocognitive dysfunction in bipolar and schizophrenia spectrum disorders depends on history of psychosis rather than diagnostic group. *Schizophrenia Bulletin*, *37*(1), 73–83. <http://doi.org/10.1093/schbul/sbp034>
- Tkachev, D., Mimmack, M. L., Ryan, M. M., Wayland, M., Freeman, T., Jones, P. B., et al. (2003). Oligodendrocyte dysfunction in schizophrenia and bipolar disorder. *The Lancet*, *362*(9386), 798–805. [http://doi.org/10.1016/S0140-6736\(03\)14289-4](http://doi.org/10.1016/S0140-6736(03)14289-4)
- Uranova, N., Orlovskaya, D., Vikhreva, O., Zimina, I., Kolomeets, N., Vostrikov, V., & Rachmanova, V. (2001). Electron microscopy of oligodendroglia in severe mental illness. *Brain Research Bulletin*, *55*(5), 597–610.

The material presented in this chapter is a representation of the following open-access publication that was reproduced under the Creative Commons Attribution License (CC BY <https://creativecommons.org/licenses/by/4.0/>).

Rowley CD, Bazin P-L, Tardif CL, Sehmbi M, Hashim E, Zaharieva N, Minuzzi L, Frey BN and Bock NA (2015) Assessing intracortical myelin in the living human brain using myelinated cortical thickness. *Front. Neurosci.* 9:396. doi: 10.3389/fnins.2015.00396

The only changes made were for thesis formatting and continuity purposes and copy editing.

Author List Contributions:

CD Rowley conducted image processing and analysis, contributed to writing manuscript.

PL Bazin provided code for the analysis of images

CL Tarfif also provided code for image analysis

M Sehmbi recruited and imaged subjects for the experiment

E Hashim contributed to analysis methods and writing the manuscript

N Zaharieva provided code for statistical methods

L Minuzzi contributed to the statistical analysis

BN Frey assisted in study design

NA Bock contributed to study design and writing of the manuscript

**Assessing intracortical myelin in the living human brain using myelinated cortical
thickness**

Christopher D. Rowley¹, Pierre-Louis Bazin², Christine L. Tardif², Manpreet Sehmbi³,
Eyesha Hashim¹, Nadejda Zaharieva¹, Luciano Minuzzi³, Benicio N. Frey³, Nicholas A.
Bock^{1*}

¹Department of Psychology, Neuroscience and Behaviour, McMaster University,
Hamilton, Ontario, Canada

²Department of Neurology, Max Planck Institute for Human Cognitive and Brain
Sciences, Leipzig, Germany

³Department of Psychiatry and Behavioural Neurosciences, McMaster University,
Hamilton, Ontario, Canada

*Corresponding Author

1280 Main Street West, Hamilton Ontario, Canada L8S 4K1

bockn@mcmaster.ca, Phone: 905-525-9140 ext. 21437

Conflict of Interest: The authors declare no competing financial interests.

Funding: This project was supported by the Independent Investigator Award, Brain & Behavior Research Foundation (Dr. Frey) and the AFP Innovations Award, Department of Psychiatry and Behavioural Neurosciences, McMaster University (Dr. Minuzzi). The authors are grateful to the Stanley Foundation for postmortem tissue donations.

Abstract

Alterations in the myelination of the cerebral cortex may underlie abnormal cortical function in a variety of brain diseases. Here, we describe a technique for investigating changes in intracortical myelin in clinical populations on the basis of cortical thickness measurements with magnetic resonance imaging (MRI) at 3 Tesla. For this, we separately compute the thickness of the shallower, lightly myelinated portion of the cortex and its deeper, heavily myelinated portion (referred to herein as unmyelinated and myelinated cortex, respectively). Our expectation is that the thickness of the myelinated cortex will be a specific biomarker for disruptions in myeloarchitecture. We show representative atlases of total cortical thickness, T , unmyelinated cortical thickness, G , and myelinated cortical thickness, M , for a healthy group of 20 female subjects. We further demonstrate myelinated cortical thickness measurements in a preliminary clinical study of 10 bipolar disorder type-I subjects and 10 healthy controls, and report significant decreases in the middle frontal gyrus in T , G , and M in the disorder, with the largest percentage change occurring in M . This study highlights the potential of myelinated cortical thickness measurements for investigating intracortical myelin involvement in brain disease at clinically relevant field strengths and resolutions.

2.1 Introduction

The cerebral cortex contains a substantial number of myelinated axons whose pattern of distribution describes its *myeloarchitecture*. Intracortical myelin is found predominantly in the deeper layers of the cortex, and likely serves to speed the propagation of neural signals, as myelin does in the major white matter tracts. It also fine-tunes the timing and synchrony of neural networks, thereby continuously optimizing cortical function (Haroutunian et al., 2014). The density of these myelinated axons, their orientation, and how they are distributed over the cortical layers are regionally dependent in the cortex (Nieuwenhuys, 2012), suggesting that specific features of myeloarchitecture may be related to specific cortical functions. Thus, abnormalities in intracortical myelin may correlate with disrupted function in brain disease.

Magnetic resonance imaging (MRI) is now used *in vivo* to visualize intracortical myelin (Glasser & Van Essen, 2011), since myelin alters MR parameters within the gray matter similarly to how it alters MR parameters in white matter. There have been several MRI studies linking changes in intracortical myelin to changes in function. Imaging studies in large numbers of subjects have confirmed cerebral myelin maturation and aging-related degradation (Grydeland, Walhovd, Tamnes, Westlye, & Fjell, 2013; Shafee, Buckner, & Fischl, 2015) and have indicated that a higher degree of intracortical myelin is associated with greater performance stability on a cognitive task (Grydeland et al., 2013). It has also been shown that the degree of myelination in the left posterior cortex

plays a role in error processing and cognitive control (Grydeland, Westlye, Walhovd, & Fjell, 2016), while a study in blind individuals suggests that increased intracortical myelin may represent a mechanism for compensatory functional reorganization in the visual cortex (Voss, Pike, & Zatorre, 2014). Conversely, MRI has identified deficits in cortical myelin in mental disease, with losses of intracortical myelin being observed in patients with schizophrenia (Bartzokis et al., 2012; 2009). Combined, these studies predict a future role for MRI in studies of how intracortical myelin is related to function in health and disease.

While MRI lacks the resolution to visualize the fine details of the myeloarchitecture in living humans, it can map intracortical myelin content grossly across the entire cortex. For intracortical myelin mapping studies, the cortex is imaged with either a quantitative MRI sequence that measures a parameter that is sensitive to myelin [T_1 (or R_1), T_2^* , magnetization transfer ratio (MTR) (Cohen-Adad et al., 2012; Mangeat, Govindarajan, Mainero, & Cohen-Adad, 2015; Marques & Gruetter, 2013; Sereno, Lutti, Weiskopf, & Dick, 2013), or a qualitative sequence with the contrast optimized such that the image intensity strongly correlates with the presence of myelin (T_1 -weighted; (Bock et al., 2013)). We used T_1 -weighted contrast for this study, because we have previously shown with *in vivo* MRI and matched histology in non-human primates that T_1 -weighted signal increases are spatially correlated with myelin density in the cortex (Bock, Kocharyan, Liu, & Silva, 2009). An image consisting of a combination of weightings (T_1 -

weighted/ T_2 -weighted) may also be used (Glasser & Van Essen, 2011). Since the highest density of myelinated axons occurs in the deeper layers of the cortex (Layers IV–VI), the parameter or signal intensity in the resulting image is interpolated and displayed on a surface computed at a specific depth in the cortex to represent best the intracortical myelin content over all regions. Changes in the parameter value or signal intensity are then interpreted as reflecting changes in myelin amounts.

In cortical mapping studies, data sampled at the middle depth of the cortex are often used to summarize cortical myelin; high resolution imaging studies, however, have shown that the appearance of a map of myelin content over the cortex is highly dependent on the cortical depth at which it is made (De Martino et al., 2015; Lutti, Dick, Sereno, & Weiskopf, 2014; Tardif et al., 2015). This means that comparisons of myelin content using MR signal between healthy and disease populations should incorporate cortical depth in their analyses, which could be hampered by the need to find a common cortical depth in diseases where overall cortical thickness is altered.

In this paper, we propose to investigate changes in cortical myelination based on morphology, rather than on MR signal changes. We do this by means of a myelinated cortical thickness technique, where we measure the thickness of lightly and heavily myelinated portions of the cortical depth separately. Separating cortical tissue into lightly and heavily myelinated portions based on MR contrast was previously suggested in 2D for studies of intracortical myelin in schizophrenia (Bartzokis et al., 2009), and here we

extend it to map the entire cortex in 3D. Figure 2.1 shows representative 40 μm thick histological sections of human cortex stained for myelin (adapted from (Braitenberg, 1962)). In general, the deeper layers of the cortex (IV–VI) are typically the most heavily myelinated and will have an MR signal that is distinct from the signal in superficial gray matter, which has few myelinated fibers. There may be variations in these layers in some regions (where the Bands of Baillarger and the Stria of Gennari are not continuous with deeper heavily myelinated layers), but at the 1 mm isotropic resolution of clinical MRI, the cortical depth divides overall into a lightly myelinated and heavily myelinated portion. Thus, we propose to separate the traditional measure of total cortical thickness from neuroanatomical MRI into measures of the thickness of the lightly myelinated cortex (which we will refer to as “unmyelinated” cortex here for simplicity) and heavily myelinated cortex (referred to as “myelinated” cortex).

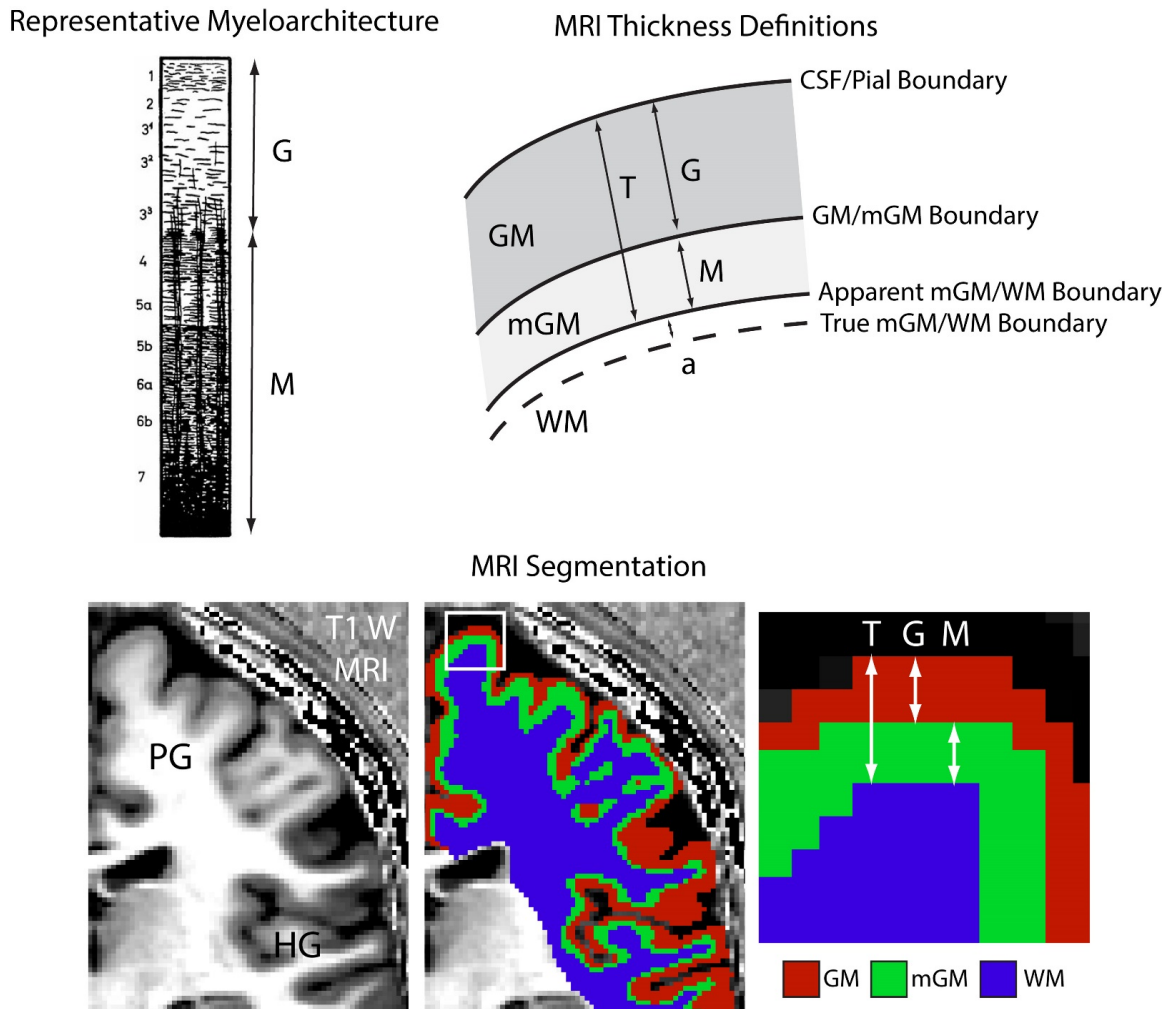


Figure 2.1: Myelinated cortical thickness measurements. The depth of the human cerebral cortex can be roughly subdivided into lightly myelinated and heavily myelinated portions, as seen in representative 40 μm thick histological sections stained for myelin (adapted from (Braitenberg, 1962)). This leads to intracortical contrast on heavily T₁-weighted MRI, which can be used to segment the cerebrum into lightly myelinated gray matter (GM), heavily myelinated gray matter (mGM), and white matter (WM) tissue

classes. Measuring the thickness of the GM and mGM tissue classes yields the thickness of the lightly myelinated (G) and heavily myelinated cortical layers (M). Overall cortical thickness (T) is also measured. The mGM class is thicker in regions known to be highly myelinated, such as the primary motor cortex in the precentral gyrus (PG) and the primary auditory cortex in Heschl's gyri (HG), MFG, middle frontal gyrus.

The myelinated cortical thickness measurement proceeds in three general steps:

1. Generate a weighted intensity image or a parametric map of the brain using MRI with strong intracortical contrast.
2. Identify the cerebrum (consisting of cortical gray matter and underlying major white matter tracts) in the brain and use a clustering algorithm to segment this anatomy into three tissue classes based on signal or parameter intensities: unmyelinated gray matter (GM), myelinated gray matter (mGM), and white matter (WM).
3. Use cortical thickness measurement techniques to find the distance between the cerebral spinal fluid (CSF)/GM boundary and the mGM/WM boundary (T), the distance between the CSF/GM and GM/mGM boundaries (G), and the distance between the GM/mGM boundary and the mGM/WM boundary (M).

These measurements yield three thickness parameters as shown in **Figure 1**: the total cortical thickness, T , the thickness of the unmyelinated layers, G , and the thickness of the myelinated layers, M . One may also calculate the proportional myelinated thickness

of the cortex as:

$$P = \frac{M}{T} \quad (1)$$

which summarizes the proportion of the cortical depth that is myelinated. The approach is similar to that used to measure total cortical thickness in standard software packages such as Freesurfer (<http://surfer.nmr.mgh.harvard.edu/>), except that it is considering three tissue classes in the cerebrum (GM, mGM, and WM), rather than two (GM and WM). This is only appropriate in the case that the input MRI image has enough intracortical contrast to allow segmentation into three classes.

In typical cortical thickness studies of brain disease, changes in total cortical thickness, T , are interpreted as broadly reflecting changes in cortical substructure caused by neurogenesis, axonal sprouting, dendritic branching, angiogenesis, and myelination (Zatorre, Fields, & Johansen-Berg, 2012). We expect that changes in the thickness of the myelinated portion, M , will be more specific to changes in intracortical myelin in brain disease than T , since that portion contains most of the myelin in the cortex.

Below, we demonstrate the feasibility of myelinated cortical thickness measurements made on T₁-weighted images with strong intracortical contrast collected at a clinically-relevant field strength of 3 T. We show patterns of T , G , M , and P in representative atlases made from 20 healthy female subjects. We also demonstrate the

utility of myelinated cortical thickness measurements in a preliminary study of 10 subjects with bipolar disorder and 10 healthy controls. The consensus in the literature is that bipolar disorder is associated with decreases in cortical thickness (Elvsåshagen et al., 2013; Lan et al., 2014; Lyoo et al., 2006) and we question whether losses in intracortical myelin may underlie that thinning. This is in light of imaging (Lewandowski et al., 2015; Marlinge, Bellivier, & Houenou, 2014) and histology (Regenold et al., 2007) studies which indicate losses of myelin in major white matter tracts in bipolar disorder, and neuropathology studies indicating losses of the oligodendrocytes in cortical tissue that maintain myelin (Savitz, Price, & Drevets, 2014; Uranova, Vostrikov, Orlovskaya, & Rachmanova, 2004).

We performed two imaging studies: one in healthy controls to generate atlases showing normal myelinated cortical thickness patterns, and one in subjects with bipolar disorder type-I and healthy controls to see if we could detect differences in myelinated thickness in this mental disorder. Both studies used the same imaging procedure, image processing, image registration, and atlas generation techniques. We also performed histology in the cortex of a representative individual to examine myeloarchitecture in frontal regions relevant to bipolar disorder. For the bipolar study, we performed a region-of-interest analysis of *T*, *G*, and *M* in the middle frontal gyrus, a highly myelinated area that has been implicated in bipolar disorder in humans, and also in the precentral gyrus, an area containing motor regions thought to have little involvement in the disorder.

2.2 Methods

2.2.1 Imaging Subjects

Studies were approved by the Hamilton Integrated Research Ethics Board and informed consent was obtained from each volunteer before enrollment. Images for the first study were collected in 20 healthy females, aged 30 ± 8 years ($\mu \pm \sigma$). Images for the second study were obtained in 10 healthy females, aged 30 ± 9 years, and 10 females with bipolar disorder type- I, aged 33 ± 8 years. Nine bipolar subjects had been clinically stable (euthymic) for at least 2 months and one was in a current depressive episode. All study participants were interviewed with the Structured Clinical Interview for DSM-IV (First et al., 2002) to confirm group status. In terms of treatment, three bipolar subjects were on lithium at the time of the study, four were on anticonvulsants, six were on atypical antipsychotics, two were on antidepressants and four were on anxiolytics. The average medication count across all 10 bipolar subjects was 2.50 (SD: 1.72), which is well-consistent with studies in bipolar disorder. The demographic details are presented in

TABLE 1 | Subject demographics for the bipolar study presented as mean \pm standard deviation.

	Control	Bipolar disorder type 1
Number	10	10
Age	32.8 \pm 9	33.3 \pm 7
Education (years)	15.8 \pm 2	16.2 \pm 3
Height (inches)	64.7 \pm 3	65.1 \pm 3
Weight (pounds)	141 \pm 34	157 \pm 24
BMI (kg/m ²)	23.7 \pm 5	26.1 \pm 3
Smoker	3	4
Duration of illness (years)	N/A	17.0 \pm 7
Number of manic episodes	N/A	7.0 \pm 5
Number of depressive episodes	N/A	15.2 \pm 9
Number of mixed episodes	N/A	1.6 \pm 3
Number of hypomanic episodes	N/A	9.3 \pm 8
Age of first episode (years)	N/A	15.2 \pm 6

Table 2.1: Subject demographics for the bipolar study presented as mean \pm standard deviation.

2.2.2 Imaging

Images were acquired on a 3T General Electric scanner (Software Version 22.0) using a 32-channel receive-only coil for the head (MR Instruments) and a transmit body coil (GE).

2.2.2.1 Anatomical Reference Image

A 3D T_1 -weighted whole-head image with 1 mm isotropic resolution was made using a 3D inversion-recovery gradient echo sequence (GE 3D BRAVO) [Inversion time = 450ms, TE = 3.2 ms, TR in acquisition block = 8.4 ms, flip angle in acquisition block = 12° , field of view (FOV) = $25.6 \times 25.6 \times 25.6$ cm, matrix = $256 \times 256 \times 256$, linear phase encoding, Autocalibrating Reconstruction for Cartesian imaging (ARC) parallel imaging factor of 2 in the second phase encode direction, Number of averages = 1, time = 5min 32 s]. This image served as an anatomical reference for image registration.

2.2.2.2 High Intracortical Contrast T_1 -weighted Image

Another 3D T_1 -weighted whole-head image with 1 mm isotropic resolution and increased intracortical contrast was made from four separate images collected with an inversion-recovery gradient echo sequence (GE 3D BRAVO) [Inversion time = 1100 ms, Time between end of acquisition block and next 180° pulse (TD) = 1000 ms, TE = 3.2 ms, TR in acquisition block = 8.4ms, flip angle in acquisition block = 12° , FOV = 24.0×10.0 (selective slab in left/right direction) $\times 24.0$ cm, matrix = $240 \times 100 \times 240$, centric phase encoding, ARC factor 2 in second phase-encoding direction, Number of averages = 1, time = 5 min 53s]. To increase intracortical contrast, each hemisphere was imaged separately. That reduced the matrix dimension in the first phase-encoding direction in the sequence, which in turn shortened the acquisition block following the inversion pulse. This is akin to using multiple segments in a magnetization- prepared rapidly-acquired

gradient echo sequence (MP-RAGE; (Mugler & Brookeman, 1990)), where the shorter acquisition block improves contrast. A true MP-RAGE sequence was not available on our scanner, so we took this reduced-FOV approach instead, employing a long TD to increase intracortical contrast (Bock et al., 2013). Finally, to increase the contrast-to-noise ratio further, each hemisphere was imaged twice. Overall, this image took 24 min to acquire.

Each of the four separate images was registered to the anatomical reference image via a 6-parameter rigid transformation with sinc resampling using the FLIRT tool in FSL (Jenkinson, Beckmann, Behrens, Woolrich, & Smith, 2012) version 5.0 (fsl.fmrib.ox.ac.uk/fsl/). The magnitude images were then summed to create the final image of the whole head. This image for each individual was visually inspected for artifacts arising from improper registration, and none were found.

2.2.2.3 Ratio Image

A final 3D highly proton density-weighted whole-head image at 1mm isotropic resolution was collected to correct B_1 inhomogeneity artifacts in the T_1 -weighted image. The image was made with a 3D gradient-echo sequence (GE 3D SPGR) [parameters: TE = 3.1 ms, TR = 7.9 ms, flip angle = 4° , FOV = $24.0 \times 17.4 \times 24.0$ cm, matrix = $240 \times 174 \times 240$, Number of averages = 1, time = 5 min 29 s].

The proton-density weighted image was registered to the T_1 -weighted image using a 6-parameter rigid transform (FSL) and filtered with a 3D median filter with a $5 \times 5 \times 5$

mm kernel size. The T_1 -weighted image was then divided by the filtered proton-density weighted image to create the ratio image, which is a highly T_1 -weighted image with B_1^- and some B_1^+ inhomogeneities removed (Marques et al., 2010; van de Moortele et al., 2009; Wang, Qiu, & Constable, 2005).

2.2.3 Image Processing

Image processing was performed predominantly in MIPAV v7.0.1 software (mipav.cit.nih.gov) using the JIST v3.0 (www.nitrc.org/projects/jist/), TOADS-CRUISE vR3c (www.nitrc.org/projects/toads-cruise/), and CBS High-Res Brain Processing Tools Version v3.0 (www.nitrc.org/projects/cbs-tools/) plug-ins, and Amira v5.2 software (Visage Imaging).

The first step in processing was to generate labels identifying the cerebrum in an individual's brain. The T_1 -weighted image was used as input to the SPECTER 2010 algorithm (Carass et al., 2011) in MIPAV, which created a mask identifying the brain and dura matter based on a combination of atlas-based segmentation, tissue classification and region growing. The T_1 -weighted image was used for this skull stripping rather than the Ratio image because the background in the Ratio image had a high mean value that made it difficult to identify air-tissue boundaries. The mask was then used to skull strip the Ratio image.

The skull-stripped Ratio image was used as input to the Multiple Object

Geometric Deformable Model (MGDM) Multi-contrast Brain Segmentation algorithm (Bazin et al., 2014; Bogovic, Prince, & Bazin, 2013) in MIPAV to generate initial probabilistic labels for tissue classes in the brain. This algorithm evolves multiple boundary surfaces simultaneously according to competing forces derived from a prior intensity, shape and topology model to label the entire brain. The resulting probability labels for cerebral gray matter and white matter were then used as input to the CRUISE algorithm (Han et al., 2004) in MIPAV, which generated smoothed, topologically correct labels for the cerebrum using nested geometric deformable models and an anatomically consistent enhancement of sulcal CSF. This was performed in each hemisphere separately.

Subcortical structures and ventricles (as identified by the MGDM algorithm) were then removed from the labels for the left and right cerebrums and their labels were combined. This label for the entire cerebrum without the subcortical structures was then used to mask the Ratio image such that it contained only the cerebral cortex and underlying white matter tracts.

The cerebrum-masked Ratio image was then segmented into three tissue classes using the FANTASM algorithm (Pham, 2001) in MIPAV, which is based on a fuzzy c-means clustering algorithm with additional spatial regularization. This produced membership images for each tissue class, whose voxel values described the probability of that voxel belonging to a particular class. For instance, a value of 0.5 or greater for a

membership function would mean there was a greater than 50% probability of that voxel belonging to the given class. In order to define nested boundaries for the WM, mGM and GM, the membership functions were binarized with a series of thresholds: the first label, for the innermost mGM/WM boundary, was initially created to include all voxels with a given WM fuzzy membership threshold above 0.5. This was later refined to include all voxels with a given WM fuzzy membership threshold above 0.1 to reduce partial volume effects at the boundary with the WM. This refinement was performed to match more closely the WM segmentation that would result from a two-class tissue segmentation (see Section Results). Note that the fuzzy classification is independent of this adjustment, which only affects the location of the WM boundary. The mGM/GM boundary and unmyelinated thickness both remain unchanged. The second label, for the GM/mGM boundary, included the remaining voxels with an mGM fuzzy membership above 0.5, and finally the last label for the CSF/GM boundary included the remaining voxels again with a GM fuzzy membership above 0.5. All labels were split back into left and right hemispheres for subsequent processing. The mGM/WM-boundary labels were morphologically processed to remove all tissue not connected to the largest mass. The GM/mGM-boundary labels were slightly smoothed in Amira using 3D morphological smoothing with a kernel size of $2 \times 2 \times 2$ mm. Voxels identified at the outermost surface of the cortex in these labels were removed using a mask made from a 1- voxel morphologically eroded version of the CSF/GM-boundary labels.

For distance measurements, signed distance levelset functions were calculated for

the CSF/GM, GM/mGM and mGM/WM tissue boundaries using the Distance Field algorithm from the JIST plugins in MIPAV. Distances between boundaries were calculated as follows:

$$G = \varphi_{CSF/GM} - \varphi_{GM/mGM} \quad (2)$$

$$T = \varphi_{CSF/GM} - \varphi_{mGM/WM} \quad (3)$$

where φ is the levelset (the signed distance function perpendicular from a given surface) for a given boundary, T is the total cortical thickness, and G is the unmyelinated cortical thickness. These distances were measured at the CSF/GM (pial) surface and embedded in a 3D image of the same dimensions as the input images. This allowed sampling of the values at a surface generated at the pial surface.

The myelinated cortical thickness was calculated from these distance images as:

$$M = T - G \quad (4)$$

such that M was also defined at the pial surface and propagated similarly.

Finally, the proportional myelinated thickness was calculated from the distance images according to Equation (1).

The distance images for individual subjects were visualized on the pial surface in Amira. This surface mesh was created from the CSF/GM boundary labels and the distance images were projected on it using nearest-neighbor interpolation.

2.2.4 Average Atlas Generation

To create average atlases of T , G , M , and P , the distance images for each individual were registered to the ICBM 152 atlas space (Fonov et al., 2011) with FSL Version 5.0. The necessary warp was determined by non-linearly registering the T_1 -Weighted image to the ICBM 152 atlas using the parameters provided in the `T1_2_MNI152_2 mm.cnf` file, which is packaged with FSL. This warp was then applied to each distance file with sinc resampling to transform it to the atlas. The individual registered images were combined in Matlab (Mathworks) into a single average atlas image for each metric.

The registered atlas distance images were visualized in Amira using a surface mesh created from the pial surface of the MNI 152 atlas. This surface with the distance maps displayed on it was also inflated in Caret ((Van Essen et al., 2001); www.nitrc.org/projects/caret/) to show the pattern of myelinated thickness within the cortical folds. The cortical surface was inflated using 500 iterations with smoothing every 10 iterations and an inflation factor of 1.02.

2.2.5 Histology

Postmortem brain tissue from a 43 year old male with a past history of depression and substance abuse was obtained from the Stanley Medical Research Institute's Brain Collection (Chevy Chase, MD). The tissue consisted of 10 μm thick paraffin embedded coronal sections of the dorsal lateral prefrontal cortex. For staining, sections were

deparafinized and hydrated in 95% ethanol. They were then soaked overnight in Luxol fast blue solution and differentiated until there was good gray/white matter contrast with light staining remaining in the gray matter. It was important not to differentiate overly the sections and remove all stain in the gray matter, since then the myelinated intracortical axons would not be visible. Whole stained sections were digitized using a Pentax K5 DSLR (Ricoh) with an SMC-A 50mm f 2.8 macro lens. Captured color images were converted into grayscale in Adobe Photoshop CS4 using only the red channel, to enhance contrast. Magnified views of sections were captured on an EVOS FL Cell Imaging System (Life Technologies) in gray scale using the Texas Red filter, again to enhance contrast.

2.2.6 Region of Interest Analysis

For the bipolar study, average atlases of T , G , and M were created for control and bipolar groups. T , G , and M were then measured bilaterally in each individual's registered images in a region-of-interest (ROI) corresponding to the cortical ribbon in the middle frontal gyrus (MFG) and precentral gyrus (PCG). A statistical analysis was performed with the software Minitab 17 (Minitab, Inc.) separately on T , G , and M between control and bipolar groups in the MFG and PCG. A two-sided ANOVA tested for significant differences between groups at the $p < 0.05$ level, following confirmation that the data were normal (using an Anderson–Darling test) and that groups had equal variances. This was followed by a Tukey pairwise comparison test at a significance level of $p < 0.05$. A

power analysis was also performed using the ROI data from the control subjects in Minitab to estimate effect size.

2.3 Results

The myelinated cortical thickness technique relies on data- driven clustering of MRI intensity in the voxels of the cerebrum to obtain the three tissue classes: GM, mGM, and WM. The FANTASM technique in our study is based on fuzzy c-means clustering, which means that each voxel can be assigned to multiple tissue classes. In our initial data analysis approach, we chose a fuzzy c-means membership threshold of greater than 0.5 for each tissue class, meaning that each contained voxels predominantly assigned to that class (Figure 2.2). We found, however, that this threshold underestimated the volume of the WM tissue class in the cerebrum because the additional mGM tissue class resulted in a displaced WM/mGM boundary compared to a two-tissue classification. This underestimation was especially prevalent in the thin gyral blades of white matter where partial voluming effects are strongest (see white arrow in Figure 2.2). Thus, we used a fuzzy c-means membership of greater than 0.1 for the WM class only, which we found to preserve better the geometry of the original WM boundary (see histograms in Figure 2.2). This had no effect on the GM/mGM boundary, as can be seen in Figure 2.2.

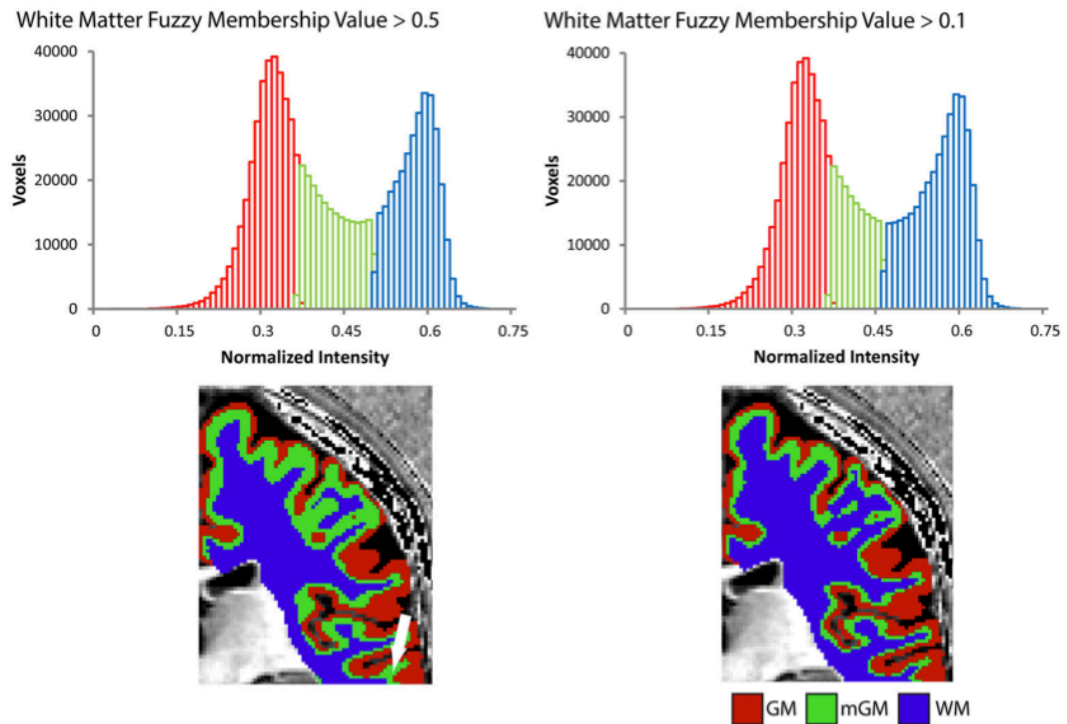


Figure 2.2: Tissue segmentation results shown for a representative individual for WM fuzzy c-means threshold values greater than 0.5 or 0.1. Each histogram plots the number of voxels assigned to each class in the cerebrum against normalized MRI signal intensity and each image shows the resulting segmentation superimposed on a 2D slice from the 3D Ratio MRI. Note the improved definition of the mGM/WM boundary in the thin gyral blade of white matter located at the white arrow.

Figure 2.3 shows dorsal views of representative atlases of myelinated cortical thickness measurements in 20 healthy female subjects. It illustrates that the pattern of G over the cortex largely follows that of T , suggesting that cortical regions with the greatest total thickness also have the greatest thickness in their unmyelinated layers. The pattern

of M does not follow G as closely and some regions that have the smallest total thickness, such as the postcentral gyrus and the calcarine fissure, in fact have the thickest myelinated layers. The figure also shows the atlas for P , which is a summary metric describing the proportion of the cortical thickness that is myelinated. It is interesting to note that regions showing the largest values for M and P are the same regions that have been identified as having high myelin contents from previous MRI studies of intracortical myelin using the MR signal for mapping (Cohen-Adad et al., 2012; Glasser & Van Essen, 2011; Lutti et al., 2014). This is shown comprehensively in Figure 2.4 in views of the average atlas for P over the entire cortex, where the proportional depth of the cortex that is highly myelinated is greatest in the precentral gyrus (the location of M1 and associated motor areas), the postcentral gyrus (S1), Heschel's gyri (A1), around the calcarine fissure in the occipital cortex (the primary visual cortex, V1, and associated visual areas) and in the posterior cingulate gyrus. These regions are also described in the literature as having the highest myelin content as measured from histology (Hopf, 1956; Nieuwenhuys, 2013) (Nieuwenhuys, 2012).

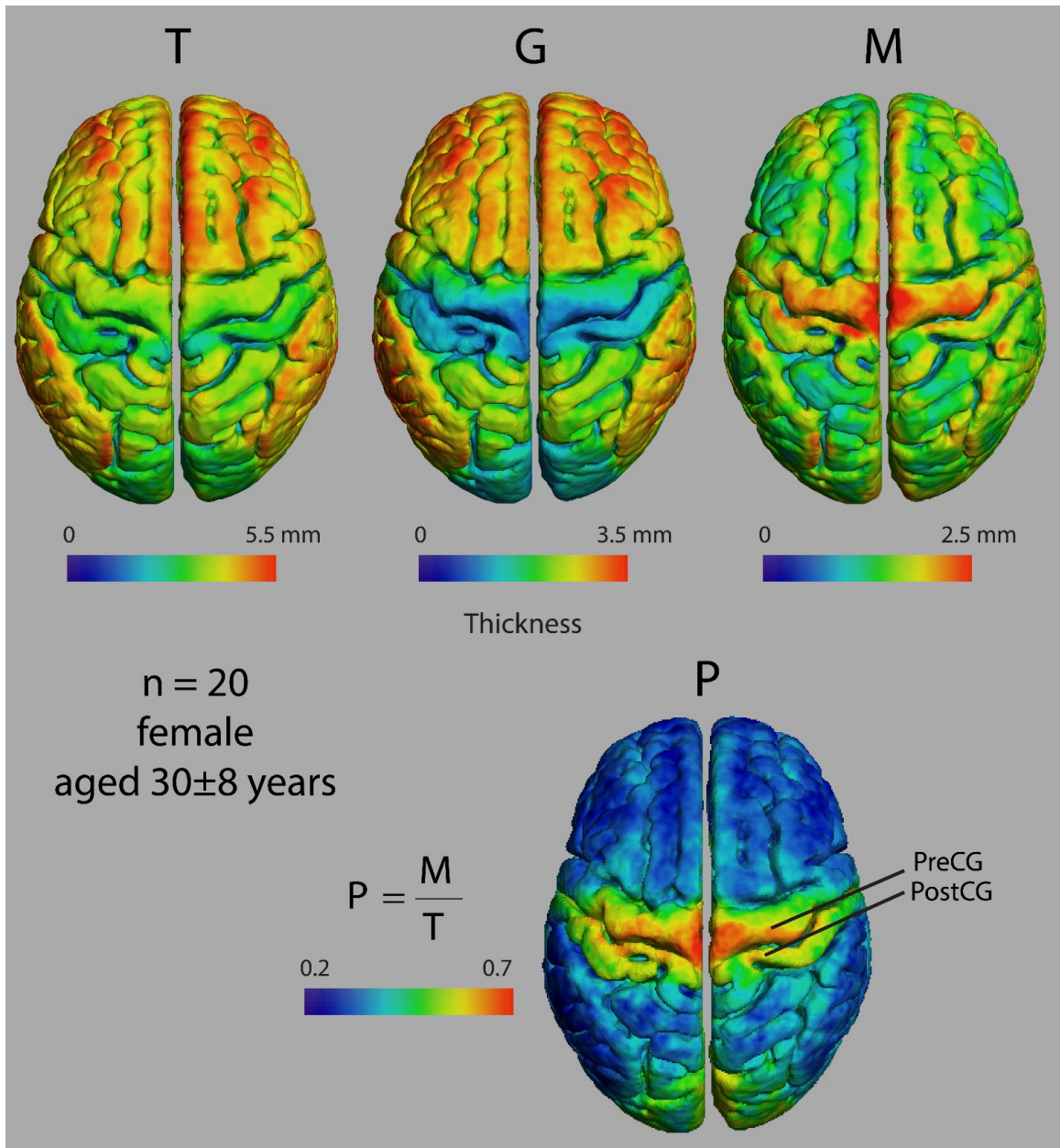


Figure 2.3: Dorsal views of four thickness measures in an atlas made from 20 female subjects. T, total cortical thickness; G, unmyelinated cortical thickness; M, myelinated cortical thickness; P, proportional myelinated thickness; PreCG, precentral gyrus;

PostCG, postcentral gyrus.

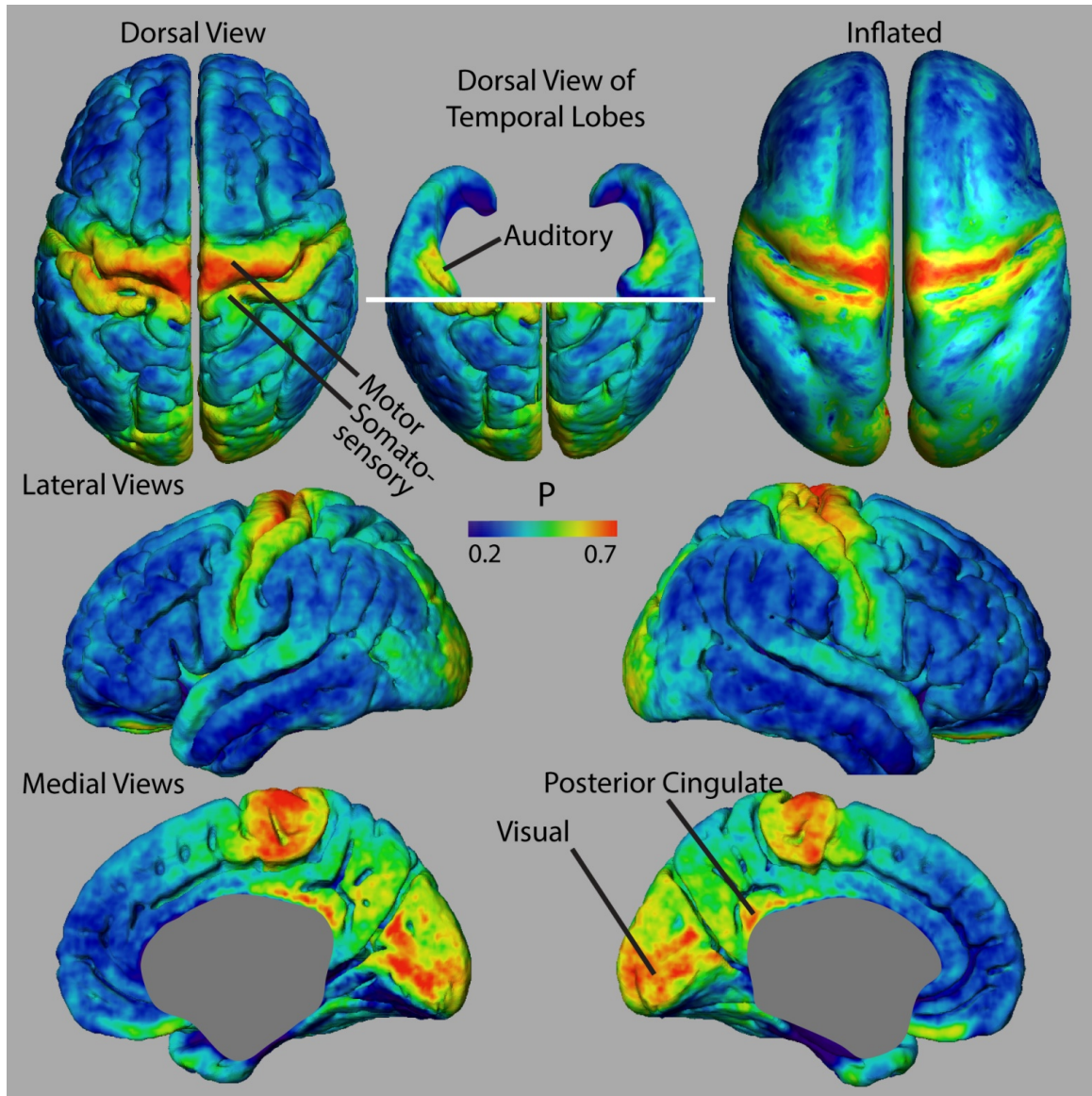


Figure 2.4: Views of proportional myelinated thickness, P , in an atlas made from 20 female subjects.

Figure 2.5A shows a representative distribution of myelinated fibers from histology in an individual in the dorsal frontal cortex. On the middle frontal gyrus (MFG), a dense distribution of myelinated fibers extends substantially through the cortical depth, implying that M would be thick in this region. That is confirmed in the M average atlas, which shows the MFG as having the greatest thickness of myelinated cortex in the dorsal frontal cortex (Figure 2.5A bottom). Figure 2.5B shows the myeloarchitecture in the MFG at a 10X magnification, revealing that most myelinated fibers exist in small bundles through the cortex. On the nearby anterior cingulate gyrus, the dense distribution of myelinated fibers does not extend as far over the cortical depth, implying that M is thinner in this region, which we also note in the average atlas. Finally, the dense distribution of myelinated fibers in the inferior frontal sulcus is closely localized at the WM boundary, suggesting that M is very thin in this region. Such is generally true of the depths of sulci in the cortex, which have been shown to contain far fewer myelinated fibers than the gyral crowns (Annese et al., 2004) and is again confirmed by low values for M in our average atlas.

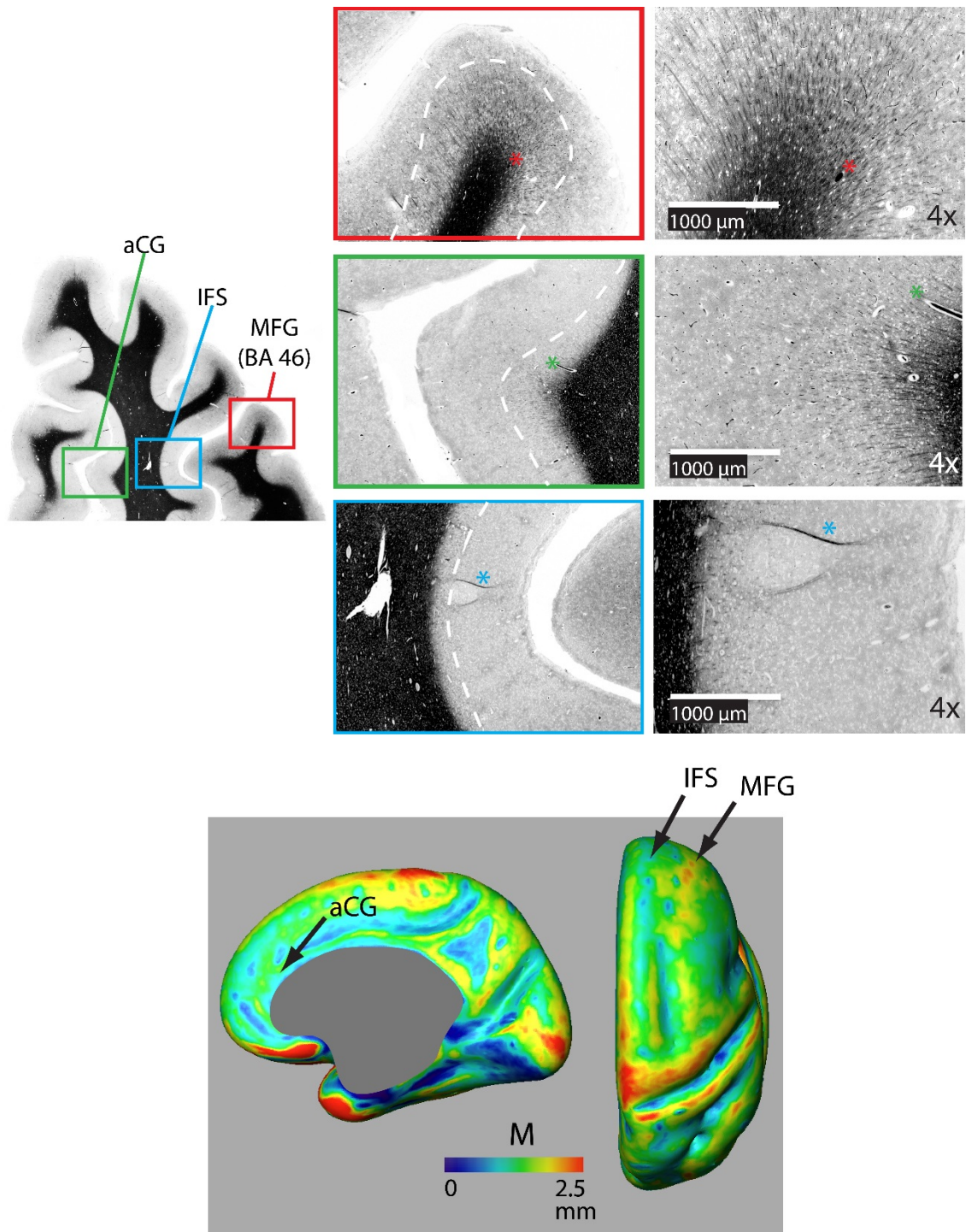


Figure 2.5A: Representative coronal section of the dorsal frontal cortex stained for

myelin showing the distribution of bundles of myelinated fibers on the middle frontal gyrus (MFG) [Brodman's area 46 (BA 46)], on the anterior cingulate gyrus (aCG), and in the inferior frontal sulcus (IFS). The white dotted line shows the rough extent of bundles over the three regions. The asterisk denotes the same blood vessel at each magnification. The bottom panel shows the location of regions on an inflated atlas of M in the right hemisphere in healthy controls on medial and dorsal views, respectively, pCG, posterior cingulate gyrus.

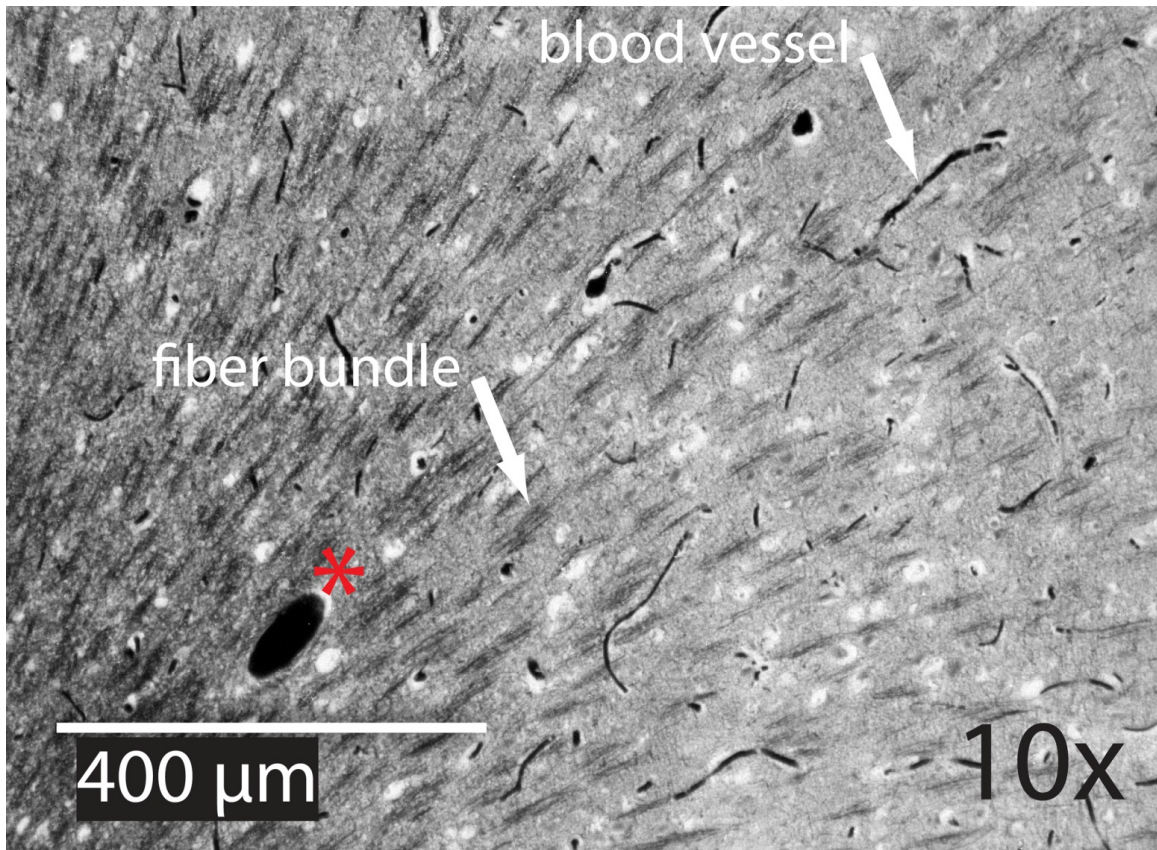


Figure 2.5B: 10X magnification in the MFG illustrating bundles of myelinated fibers and

distinctly darker blood vessels.

Figure 2.6 shows average atlases for T , G , and M in 10 control and 10 bipolar subjects from a preliminary study of myelinated cortical thickness in bipolar disorder. We did not include P in the analysis, because it includes both M and T , and thus is not an independent metric. The small sample size in this study does not produce adequate power for whole-brain statistical parametric mapping, but the trend in the maps of T suggests that total thickness is generally thinner in the bipolar subjects— more so in the association regions of the cortex than in the primary motor and sensory regions. The maps for G show largely the same trend, with visible decreases again generally in the association regions. The maps for M also show a trend toward thinner myelinated cortex in the bipolar subjects, although the decreases appear more regionally confined than for T and G .

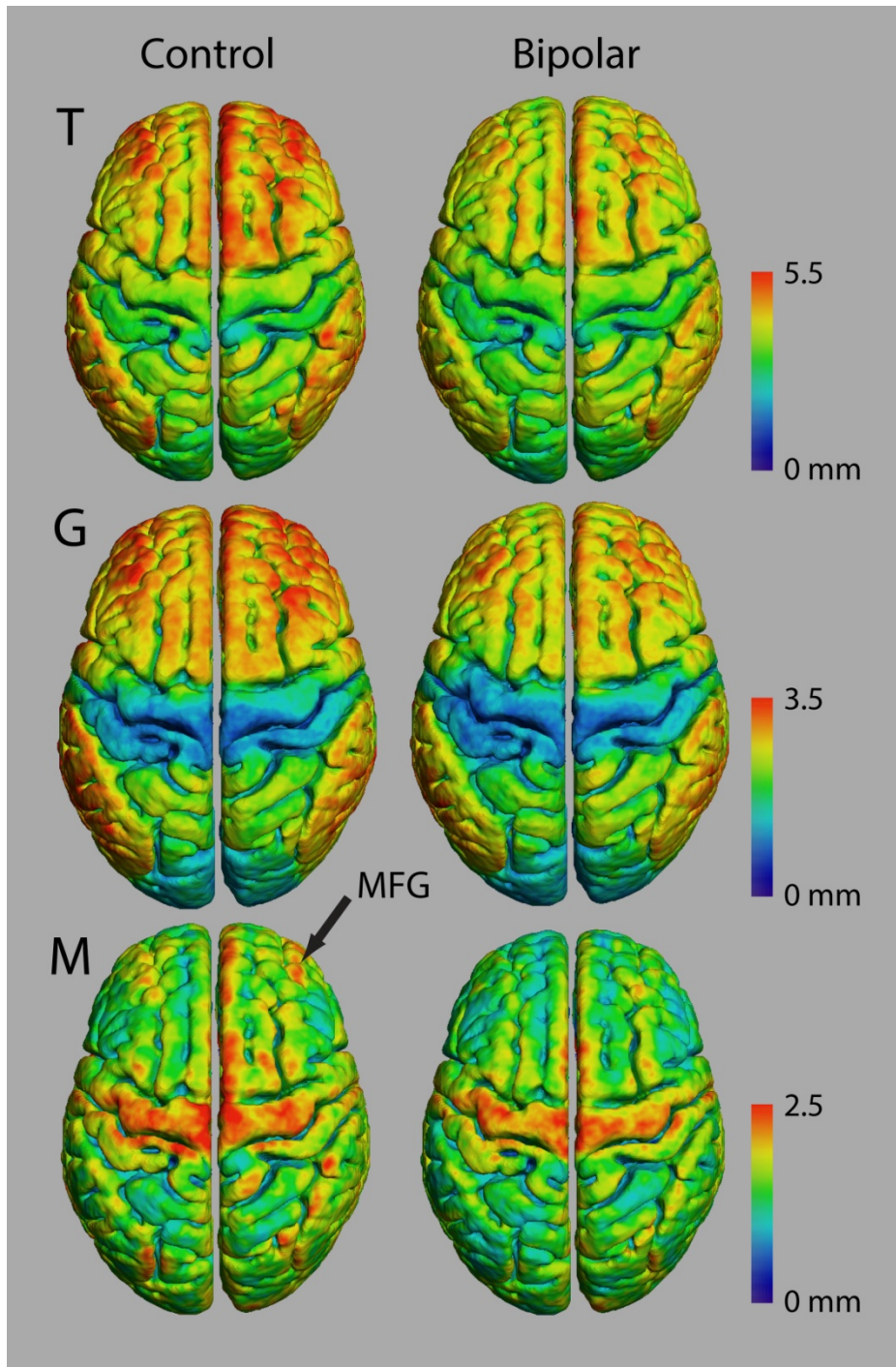


Figure 2.6: Thickness measurements in controls and bipolar disorder type-I subjects ($n =$

10 in each group).

Since the MFG in the dorsal lateral prefrontal cortex was shown to be highly myelinated in our normal average atlas of *M* and our histology study, we investigated changes there in a region of interest (ROI) analysis study of *T*, *G*, and *M* (Figure 2.7, and Supplemental Figure 2.8). We also investigated changes in the precentral gyrus (PCG), a region that contains the primary motor cortex and is not thought to be involved in bipolar disorder. We found statistically significant decreases in all three metrics in bipolar subjects in both the left and right MFG ($p < 0.05$), but not in the PCG. Our observations of a reduced total cortical thickness in the MFG are consistent with other reports of cortical thinning in the DLPFC in bipolar disorder (Elvsåshagen et al., 2013; Hartberg et al., 2011; Lyoo et al., 2006). Interestingly, the percentage difference change was largest for *M* of all the metrics, which could suggest that disruptions in intracortical myelin are implicated in the overall cortical thinning observed in other studies of the MFG in bipolar disorder.

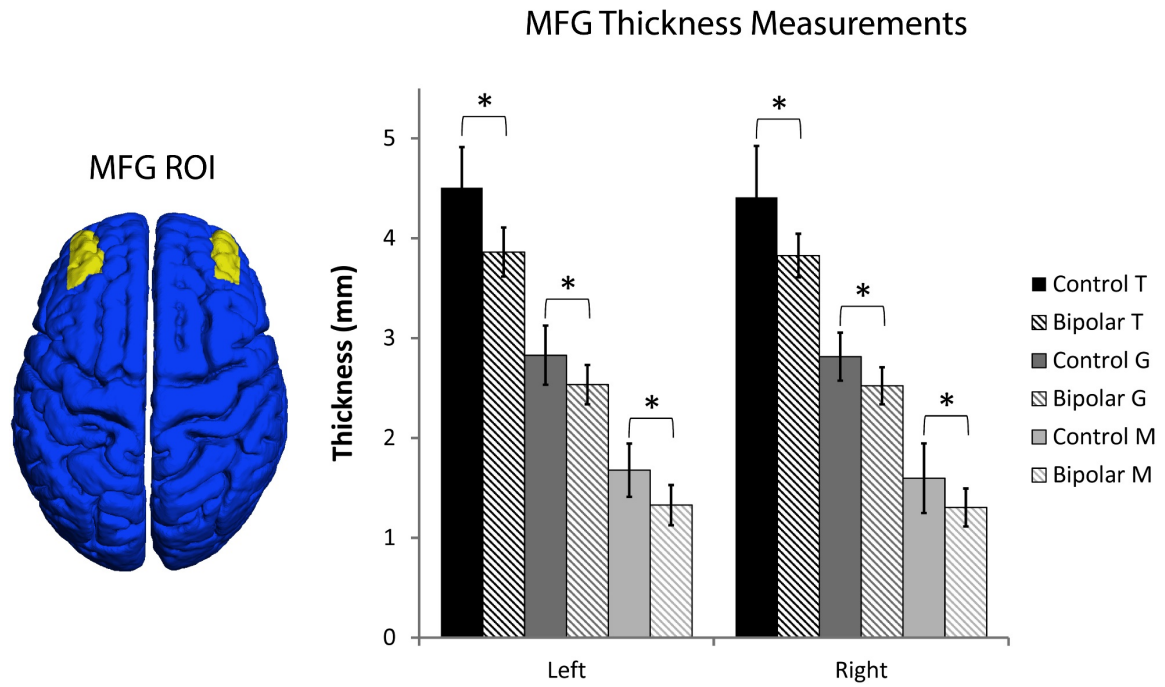
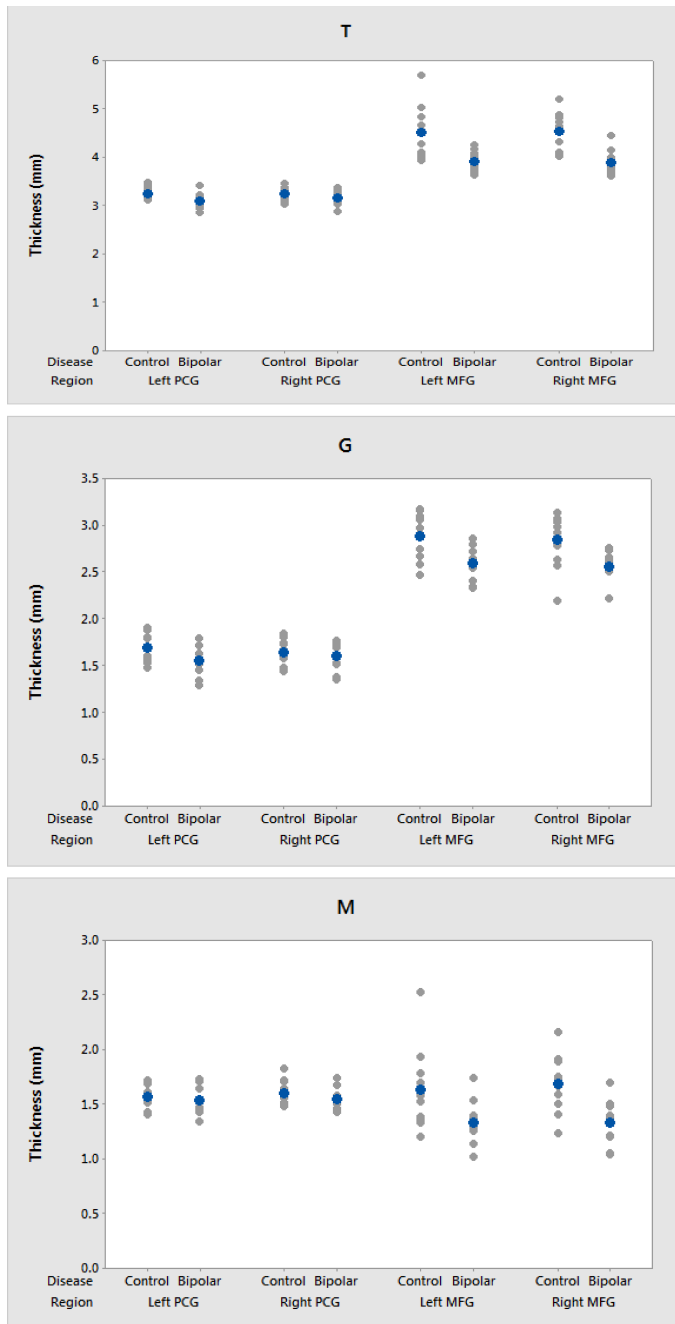


Figure 2.7: Region-of-interest thickness measurements ($\mu \pm \sigma$, $n = 10$ in each group) in the middle frontal gyrus (MFG) and precentral gyrus (PCG). An asterisk denotes statistical significance between control and bipolar groups at $p < 0.05$.



Supplementary Figure 2.8: Individual region-of-interest thickness measures in the middle frontal gyrus (MFG) and precentral gyrus (PCG). The blue colored dot indicates

the mean for each group.

Finally, we used the data from the ROI analysis for the 10 control subjects to estimate effect sizes for the myelinated cortical thickness technique. In the MFG, with a two-way *t*-test at a significance level of 0.05 and a power of 0.8, one could detect significant differences in mean *T* of 6%, *G* of 7%, and *M* of 11%. In the PCG, one could detect significant differences in the mean of *T* of 3%, of *G* of 6%, and of *M* of 5%. This suggests that the technique produces useful effect sizes for clinical studies, even in relatively small groups of individuals, provided the variance in thickness metrics in the clinical subjects was the same as the controls. We were actually able to detect smaller significant effect sizes in this study because the variance of the thickness values in the bipolar subjects was actually lower than in controls.

2.4 Discussion and Conclusion

Here we demonstrate that the cerebrum in an MRI image with high intracortical contrast can be segmented into three tissue classes using a clustering algorithm, which, based on brain histology, we hypothesize to represent lightly myelinated gray matter (GM), heavily myelinated gray matter (mGM), and white matter (WM). The mGM tissue class appears continuous across the deeper portion of the cortex at our imaging resolution of 1mm isotropic resolution. Thus, with our technique we could define two unique thickness measures for shallower, unmyelinated gray matter and deeper, myelinated gray matter. This myelinated cortical thickness measurement provides a new approach to

complement traditional cortical thickness studies where it is now possible to ascribe changes in cortical thickness in disease studies to one or both of the two tissue classes in the cerebral cortex.

Although 1mm isotropic resolution may seem low for measuring meaningful changes in cortical thickness (since the cortex itself is only a few millimeters thick), it is still assumed to be possible to measure sub-millimeter changes in cortical thickness on 3D MRIs (Fischl & Dale, 2000). This is because the true underlying pial and white matter surfaces in the brain are smooth. Thus, if the radius of curvature of these surfaces and the thickness of the tissue classes is greater than the size of the imaging resolution, then the reconstructed surfaces can be interpolated to achieve sub-voxel accuracy in thickness measurements. The same argument holds true for myelinated thickness measurements, even though the unmyelinated and myelinated portions of the cortex are thinner than the overall cortex. This was validated by the power analysis in our study which showed similar effect sizes for measurements of T , G , and M .

The thickness of the myelinated layers, M , may be specific to changes in cortical myelination, and changes in this metric may indicate intracortical myelin involvement in brain diseases. For instance, M could change if either the number of myelinated fibers in the cortex, or the amount of myelin ensheathing their axons changed. Recent studies in mice have demonstrated the later, with socially isolated animals having thinner myelin sheaths around axons in the prefrontal cortex than control animals (Liu et al., 2012;

Makinodan et al., 2012). Interestingly, the thinning of the myelin sheaths preceded changes in behavior, suggesting that changes in intracortical myelin represent plasticity in the cortex of isolated mice that leads to abnormal behavior. We confirmed reports of overall cortical thinning in the MFG in bipolar disorder, and further showed that the largest percentage change in thickness occurs in the myelinated depths of that region. The MFG area is located in the dorsal lateral prefrontal cortex, and is known to be associated with executive function. Since a number of meta-analyses have shown that individuals with bipolar disorder display poor performance in executive function even during periods of clinical remission of symptoms (Robinson et al., 2006; Bora et al., 2009; Bourne et al., 2013), these findings raise the possibility that disruptions in intracortical myelin may underlie in part the neurocognitive deficits seen in bipolar patients. With future studies in larger numbers of subjects, it will be possible to perform whole-brain analyses to see if other brain regions show similar thinning of *M* in the bipolar population. It will also be interesting to extend myelinated cortical thickness measurements to other brain diseases with noted changes in overall cortical thickness. Our preliminary findings of decreased intracortical myelin in bipolar disorder are in line with several studies using a variety of brain imaging techniques such as diffusion-tension imaging (Nortje et al., 2013), quantitative T1 ρ mapping (Johnson et al., 2015), and magnetization transfer ratio (Lewandowski et al., 2015) showing abnormalities in the structure and myelin content of subcortical white matter in bipolar disorder. Because previous studies have found an association between white matter tracts and cognitive performance in bipolar disorder

(Linke et al., 2013; Poletti et al., 2015), we speculate that changes in intracortical myelin in bipolar disorder may also reflect cortical plasticity that underlies some of the behavioral deficits and disorganized thought seen in bipolar disorder. A prospective study with repeated measures of intracortical myelin and clinical assessments over time would be necessary to test this hypothesis. While the underlying mechanisms of decreased intracortical myelin are yet to be determined, proposed mechanisms include increased oxidative stress, inflammation, loss of oligodendrocytes and blood-brain barrier dysfunction (Konradi et al., 2012; Andreazza et al., 2013; Patel and Frey, 2015).

The validity of the myelinated cortical thickness measurement technique depends on two main premises: (1) whether discrete boundaries between the proposed tissue classifications GM, mGM, and WM actually exist in the cortex and (2) whether one can image those boundaries accurately. Currently, there is no dataset in the literature quantifying the myelin content over the layers for the entire cortex to confirm the first point. A few studies exist, however, that measured the optical density of a myelin stain over the layers of the cortex in selected regions of the brain to quantify myelin content (Braitenberg, 1962; Hopf, 1968, 1969, 1970). These suggest that, for the examined regions of the brain, there is a division between unmyelinated and myelinated layers of the cortex that would approximately segregate into two discrete voxel intensities when imaged with MRI at least at a coarse resolution of 1mm isotropic. We observed a similar division in our histology in the frontal cortex, where myelinated fibers were only seen to extend at a high density to a specific depth in each region. Whether this holds over the

entire cortex is not clear, and there may be regions where the boundaries between unmyelinated and myelinated cortical layers are diffuse, making the proposed description of two cortical tissue classes too simplistic. The approximation of two classes of cortical tissue is worth exploring here, however, as a first step toward characterizing cortical myelination at clinically relevant resolutions in MRI. More elaborate models to describe cortical myelination are possible (Dinse et al., 2015), but currently these require sub-millimeter resolutions achievable only with ultra- high field MRI systems.

Even if discrete boundaries between tissue classes are present, the low image resolution in MRI leads to a mixing of tissue classifications, causing a partial voluming artifact in studies of cortical thickness. While partial voluming can cause any tissue boundary in thickness measurements to be incorrectly identified, the error is most pronounced at the mGM/WM boundary because of its high curvature and the thin geometric features of the WM volume. These effects can be lessened in sub-1 mm isotropic resolution images acquired with high field MRI (Lüsebrink, Wollrab, & Speck, 2013; Tardif et al., 2015). It would also be useful in future implementations of myelinated cortical thickness mapping to correct for partial volume effects using more sophisticated strategies than simply changing the WM fuzzy c-means membership function, as we did in this study (Duché et al., 2014; Pham & Bazin, 2004; Shafee et al., 2015).

There is also potential to refine further the myelinated cortical thickness technique and improve the quality of the thickness maps. For instance, although in this study we

used an MRI protocol that was optimized to produce strong intracortical contrast, it was not specifically optimized for myelinated cortical thickness measures. Any segmentation routine based on clustering will perform more robustly the better the contrast- to-noise ratio (CNR) is between the three tissue classes; thus, different MR contrasts that are sensitive to myelin should be investigated to find the one that produces the best intracortical CNR.

Overall, measurements of myelinated cortical thickness provide a new description of intracortical myelination which can be measured at 3 Tesla in clinically achievable times. With the outlined methods, we were able to separate the cortex into lightly and heavily myelinated portions and this has the potential to disentangle changes in cortical myelination and overall cortical thickness in studies of aging, disease, and plasticity.

Funding

This project was supported by a 2014 NARSAD Independent Investigator Grant from the Brain & Behavior Research Foundation (Dr. B. Frey), and an AFP Innovations Award, Department of Psychiatry and Behavioural Neurosciences, McMaster University (Dr. L. Minuzzi). This work was partially supported by the Marie Curie IRG grant 276684 (HIRESBRAIN7T).

Acknowledgements

The authors are grateful to the Stanley Foundation for postmortem tissue donations and to

Dr. David Chettle for editing the manuscript.

Supplementary Material

The Supplementary Material for this article can be found online at:

<http://journal.frontiersin.org/article/10.3389/fnins.2015.00396>

References

Andreazza, A. C., Wang, J. F., Salmasi, F., Shao, L., and Young, L. T. (2013). Specific subcellular changes in oxidative stress in prefrontal cortex from patients with bipolar disorder. *J. Neurochem.* 127, 552–561. doi: 10.1111/jnc.12316

Annese, J., Pitiot, A., Dinov, I. D., and Toga, A. W. (2004). A myelo-architectonic method for the structural classification of cortical areas. *Neuroimage* 21, 15–26. doi: 10.1016/j.neuroimage.2003.08.024

Bartzokis, G., Lu, P. H., Raven, E. P., Amar, C. P., Detore, N. R., Couvrette, A. J., et al. (2012). Impact on intracortical myelination trajectory of long acting injection versus oral risperidone in first-episode schizophrenia. *Schizophr. Res.* 140, 122–128. doi: 10.1016/j.schres.2012.06.036

Bartzokis, G., Lu, P. H., Stewart, S. B., Oluwadara, B., Lucas, A. J., Pantages, J., et al. (2009). *In vivo* evidence of differential impact of typical and atypical antipsychotics on intracortical myelin in adults with schizophrenia. *Schizophr. Res.* 113, 322–331. doi:

10.1016/j.schres.2009.06.014

Bazin, P. L., Weiss, M., Dinse, J., Schafer, A., Trampel, R., and Turner, R. (2014). A computational framework for ultra-high resolution cortical segmentation at 7 Tesla. *Neuroimage* 93(Pt 2), 201–209. doi: 10.1016/j.neuroimage.2013.03.077

Bock, N. A., Hashim, E., Janik, R., Konyer, N. B., Weiss, M., Stanisiz, G. J., et al. (2013). Optimizing T1-weighted imaging of cortical myelin content at 3.0 T. *Neuroimage* 65, 1–12. doi: 10.1016/j.neuroimage.2012.09.051

Bock, N. A., Kocharyan, A., Liu, J. V., and Silva, A. C. (2009). Visualizing the entire cortical myelination pattern in marmosets with magnetic resonance imaging. *J. Neurosci. Methods* 185, 15–22. doi: 10.1016/j.jneumeth.2009.08.022

Bogovic, J. A., Prince, J. L., and Bazin, P. L. (2013). A multiple object geometric deformable model for image segmentation. *Comput. Vis. Image Underst.* 117, 145–157. doi: 10.1016/j.cviu.2012.10.006

Bora, E., Yucel, M., and Pantelis, C. (2009). Cognitive endophenotypes of bipolar disorder: a meta-analysis of neuropsychological deficits in euthymic patients and their first-degree relatives. *J. Affect. Disord.* 113, 1–20. doi: 10.1016/j.jad.2008.06.009

Bourne, C., Aydemir, Ö., Balanzá-Martínez, V., Bora, E., Brissos, S., Cavanagh, J. T., et al. (2013). Neuropsychological testing of cognitive impairment in euthymic bipolar

disorder: an individual patient data meta-analysis. *Acta Psychiatr. Scand.* 128, 149–162.

doi: 10.1111/acps.12133

Braitenberg, V. (1962). A note on myeloarchitectonics. *J. Comp. Neurol.* 118, 114–156.

doi: 10.1002/cne.901180202

Carass, A., Cuzzocreo, J., Wheeler, M. B., Bazin, P. L., Resnick, S. M., and Prince, J. L. (2011). Simple paradigm for extra-cerebral tissue removal: algorithm and analysis.

Neuroimage 56, 1982–1992. doi: 10.1016/j.neuroimage.2011.03.045

Cohen-Adad, J., Polimeni, J. R., Helmer, K. G., Benner, T., McNab, J. A., Wald, L. L., et al. (2012). T_2^* mapping and B_0 orientation-dependence at 7 T reveal cyto- and myeloarchitecture organization of the human cortex. *Neuroimage* 60, 1006–1014. doi:

10.1016/j.neuroimage.2012.01.053

De Martino, F., Moerel, M., Xu, J., van de Moortele, P. F., Ugurbil, K., Goebel, R., et al. (2014). High-resolution mapping of myeloarchitecture *in vivo*: localization of auditory areas in the human brain. *Cereb. Cortex* 10, 3394–3405. doi: 10.1093/cercor/bhu150

Dinse, J., Hartwich, N., Waehnert, M. D., Tardif, C. L., Schäfer, A., Geyer, S., et al. (2015). A cytoarchitecture-driven myelin model reveals area-specific signatures in human primary and secondary areas using ultra-high resolution *in-vivo* brain MRI. *Neuroimage* 114, 71–87. doi: 10.1016/j.neuroimage.2015.04.023

Duche, Q. R. P., Egan, G., Acosta, O., Gambarota, G., Salvado, O., and Saint-Jalmes, H. (2014). New partial volume estimation methods for MRI MP2RAGE. *Med. Image Comput. Comput. Assist. Interv.* 17, 129–136. doi: 10.1007/978-3-319-10443-0_17

Elvsåshagen, T., Westlye, L. T., Bøen, E., Hol, P. K., Andreassen, O. A., Boye, B., et al. (2013). Bipolar II disorder is associated with thinning of prefrontal and temporal cortices involved in affect regulation. *Bipolar Disord.* 15, 855–864. doi: 10.1111/bdi.12117

First, M. B., Spitzer, R. L., Gibbon, M., and Williams, J. B. W. (2002). *SCID-I/P (for DSM-IV-TR) Patient Edition*. New York, NY: Biometrics Research, New York State Psychiatric Institute.

Fischl, B., and Dale, A. M. (2000). Measuring the thickness of the human cerebral cortex from magnetic resonance images. *Proc. Natl. Acad. Sci. U.S.A.* 97, 11050–11055. doi: 10.1073/pnas.200033797

Fonov, V., Evans, A. C., Botteron, K., Almli, C. R., McKinstry, R. C., Collins, D. L., et al. (2011). Unbiased average age-appropriate atlases for pediatric studies. *Neuroimage* 54, 313–327. doi: 10.1016/j.neuroimage.2010.07.033

Glasser, M. F., and van Essen, D. C. (2011). Mapping human cortical areas *in vivo* based on myelin content as revealed by T1- and T2-weighted MRI. *J. Neurosci.* 31, 11597–11616. doi: 10.1523/JNEUROSCI.2180-11.2011

Grydeland, H., Walhovd, K. B., Tamnes, C. K., Westlye, L. T., and Fjell, A. M. (2013). Intracortical myelin links with performance variability across the human lifespan: results from T1- and T2-weighted MRI myelin mapping and diffusion tensor imaging. *J. Neurosci.* 33, 18618–18630. doi: 10.1523/JNEUROSCI.2811-13.2013

Grydeland, H., Westlye, L. T., Walhovd, K. B., and Fjell, A. M. (2015). Intracortical posterior cingulate myelin content relates to error processing: results from T1- and T2-weighted MRI myelin mapping and electrophysiology in healthy adults. *Cereb. Cortex*. doi: 10.1093/cercor/bhv065. [Epub ahead of print].

Han, X., Pham, D. L., Tosun, D., Rettmann, M. E., Xu, C., and Prince, J. L. (2004). CRUISE: cortical reconstruction using implicit surface evolution. *Neuroimage* 23, 997–1012. doi: 10.1016/j.neuroimage.2004.06.043

Haroutunian, V., Katsel, P., Roussos, P., Davis, K. L., Altshuler, L. L., and Bartzokis, G. (2014). Myelination, oligodendrocytes, and serious mental illness. *Glia* 62, 1856–1877. doi: 10.1002/glia.22716

Hartberg, C. B., Sundet, K., Rimol, L. M., Haukvik, U. K., Lange, E. H., Nesvåg, R., et al. (2011). Brain cortical thickness and surface area correlates of neurocognitive performance in patients with schizophrenia, bipolar disorder, and healthy adults. *J. Int. Neuropsychol. Soc.* 17, 1080–1093. doi: 10.1017/S1355617711001081

Hopf, A. (1956). [Distribution of myeloarchitectonic marks in the frontal cerebral cortex

in man]. *J. Hirnforsch.* 2, 311–333.

Hopf, A. (1968). Photometric studies on the myeloarchitecture of the human temporal lobe. *J. Hirnforsch.* 10, 285–297.

Hopf, A. (1969). Photometric studies on the myeloarchitecture of the human parietal lobe. I. Parietal region. *J. Hirnforsch.* 11, 253–265.

Hopf, A. (1970). Photometric studies on the myeloarchitecture of the human parietal lobe. II. Postcentral region. *J. Hirnforsch.* 12, 135–141.

Jenkinson, M., Beckmann, C. F., Behrens, T. E., Woolrich, M. W., and Smith, S. M. (2012). Fsl. *Neuroimage* 62, 782–790. doi: 10.1016/j.neuroimage.2011.09.015 Johnson, C. P., Follmer, R. L., Oguz, I., Warren, L. A., Christensen, G. E.,

Fiedorowicz, J. G., et al. (2015). Brain abnormalities in bipolar disorder detected by quantitative T1rho mapping. *Mol. Psychiatry* 20, 201–206. doi: 10.1038/mp.2014.157

Konradi, C., Sullivan, S. E., and Clay, H. B. (2012). Mitochondria, oligodendrocytes and inflammation in bipolar disorder: evidence from transcriptome studies points to intriguing parallels with multiple sclerosis. *Neurobiol. Dis.* 45, 37–47. doi: 10.1016/j.nbd.2011.01.025

Lan, M. J., Chhetry, B. T., Oquendo, M. A., Sublette, M. E., Sullivan, G., Mann, J. J., et al. (2014). Cortical thickness differences between bipolar depression and major

depressive disorder. *Bipolar Disord.* 16, 378–388. doi: 10.1111/bdi. 12175

Lewandowski, K. E., Ongur, D., Sperry, S. H., Cohen, B. M., Sehovic, S., Goldbach, J. R., et al. (2015). Myelin vs axon abnormalities in white matter in bipolar disorder. *Neuropsychopharmacology* 40, 1243–1249. doi: 10.1038/npp.2014.310

Linke, J., King, A. V., Poupon, C., Hennerici, M. G., Gass, A., and Wessa, M. (2013). Impaired anatomical connectivity and related executive functions: differentiating vulnerability and disease marker in bipolar disorder. *Biol. Psychiatry* 74, 908–916. doi: 10.1016/j.biopsych.2013.04.010

Liu, J., Dietz, K., DeLoyht, J. M., Pedre, X., Kelkar, D., Kaur, J., et al. (2012). Impaired adult myelination in the prefrontal cortex of socially isolated mice. *Nat. Neurosci.* 15, 1621–1623. doi: 10.1038/nn.3263

Lüsebrink, F., Wollrab, A., and Speck, O. (2013). Cortical thickness determination of the human brain using high resolution 3T and 7T MRI data. *Neuroimage* 70, 122–131. doi: 10.1016/j.neuroimage.2012.12.016

Lutti, A., Dick, F., Sereno, M. I., and Weiskopf, N. (2014). Using high-resolution quantitative mapping of R1 as an index of cortical myelination. *Neuroimage* 93(Pt 2), 176–188. doi: 10.1016/j.neuroimage.2013. 06.005

Lyoo, I. K., Sung, Y. H., Dager, S. R., Friedman, S. D., Lee, J. Y., Kim, S. J., et al.

(2006). Regional cerebral cortical thinning in bipolar disorder. *Bipolar Disord.* 8, 65–74.

doi: 10.1111/j.1399-5618.2006.00284.x

Makinodan, M., Rosen, K. M., Ito, S., and Corfas, G. (2012). A critical period for social experience-dependent oligodendrocyte maturation and myelination. *Science* 337, 1357–

1360. doi: 10.1126/science. 1220845

Mangeat, G., Govindarajan, S. T., Mainero, C., and Cohen-Adad, J. (2015). Multivariate combination of magnetization transfer, T* and B0 orientation to study the myelo-

architecture of the *in vivo* human cortex. *Neuroimage* 119, 89–102. doi:

10.1016/j.neuroimage.2015.06.033

Marlinge, E., Bellivier, F., and Houenou, J. (2014). White matter alterations in bipolar disorder: potential for drug discovery and development. *Bipolar Disord.* 16, 97–112. doi:

10.1111/bdi.12135

Marques, J. P., and Gruetter, R. (2013). New developments and applications of the MP2RAGE sequence—focusing the contrast and high spatial resolution R1 mapping. *PLoS*

ONE 8:e69294. doi: 10.1371/journal.pone. 0069294

Marques, J. P., Kober, T., Krueger, G., van der Zwaag, W., van de Moortele, P. F., and Gruetter, R. (2010). MP2RAGE, a self bias-field corrected sequence for improved

segmentation and T1-mapping at high field. *Neuroimage* 49, 1271–1281. doi:

10.1016/j.neuroimage.2009.10.002

Mugler, J. P. III, and Brookeman, J. R. (1990). Three-dimensional magnetization-prepared rapid gradient-echo imaging (3D MP RAGE). *Magn. Reson. Med.* 15, 152–157. doi: 10.1002/mrm.1910150117

Nieuwenhuys, R. (2013). The myeloarchitectonic studies on the human cerebral cortex of the Vogt-Vogt school, and their significance for the interpretation of functional neuroimaging data. *Brain Struct. Funct.* 218, 303–352. doi: 10.1007/s00429-012-0460-z

Nortje, G., Stein, D. J., Radua, J., Mataix-Cols, D., and Horn, N. (2013). Systematic review and voxel-based meta-analysis of diffusion tensor imaging studies in bipolar disorder. *J. Affect. Disord.* 150, 192–200. doi: 10.1016/j.jad.2013. 05.034

Patel, J. P., and Frey, B. N. (2015). Disruption in the blood-brain barrier: the missing link between brain and body inflammation in bipolar disorder? *Neural Plast.* 2015:708306. doi: 10.1155/2015/708306

Pham, D. L. (2001). “Robust fuzzy segmentation of magnetic resonance images,” in *Proceedings of the 14th IEEE Symposium on Computer-based Medical Systems* (Bethesda, MD), 127–131.

Pham, D. L., and Bazin, P.-L. (2004). “Simultaneous boundary and partial volume estimation in medical images,” in *Proceedings of the 7th International Conference on Medical Image Computing and Computer-Assisted Intervention (MICCAI’04)* (Rennes, FR), 119–126.

Poletti, S., Bollettini, I., Mazza, E., Locatelli, C., Radaelli, D., Vai, B., et al. (2015). Cognitive performances associate with measures of white matter integrity in bipolar disorder. *J. Affect. Disord.* 174, 342–352. doi: 10.1016/j.jad.2014.12.030

Regenold, W. T., Phatak, P., Marano, C. M., Gearhart, L., Viens, C. H., and Hisley, K. C. (2007). Myelin staining of deep white matter in the dorsolateral prefrontal cortex in schizophrenia, bipolar disorder, and unipolar major depression. *Psychiatry Res.* 151, 179–188. doi: 10.1016/j.psychres.2006.12.019

Robinson, L. J., Thompson, J. M., Gallagher, P., Goswami, U., Young, A. H., Ferrier, I. N., et al. (2006). A meta-analysis of cognitive deficits in euthymic patients with bipolar disorder. *J. Affect. Disord.* 93, 105–115. doi: 10.1016/j.jad.2006.02.016

Savitz, J. B., Price, J. L., and Drevets, W. C. (2014). Neuropathological and neuromorphometric abnormalities in bipolar disorder: view from the medial prefrontal cortical network. *Neurosci. Biobehav. Rev.* 42, 132–147. doi: 10.1016/j.neubiorev.2014.02.008

Sereno, M. I., Lutti, A., Weiskopf, N., and Dick, F. (2013). Mapping the human cortical surface by combining quantitative T(1) with retinotopy. *Cereb. Cortex* 23, 2261–2268. doi: 10.1093/cercor/bhs213

Shafee, R., Buckner, R. L., and Fischl, B. (2015), Gray matter myelination of 1555 human brains using partial volume corrected MRI images. *Neuroimage* 105, 473–485.

doi: 10.1016/j.neuroimage.2014.10.054

Tardif, C. L., Schäfer, A., Waehnert, M., Dinse, J., Turner, R., and Bazin, P. L. (2015). Multi-contrast multi-scale surface registration for improved alignment of cortical areas. *Neuroimage* 111, 107–122. doi:10.1016/j.neuroimage.2015.02.005

Uranova, N. A., Vostrikov, V. M., Orlovskaya, D. D., and Rachmanova, V. I. (2004). Oligodendroglial density in the prefrontal cortex in schizophrenia and mood disorders: a study from the Stanley Neuropathology Consortium. *Schizophr. Res.* 67, 269–275. doi: 10.1016/S0920-9964(03)00181-6

Van de Moortele, P. F., Auerbach, E. J., Olman, C., Yacoub, E., Ugurbil, K., and Moeller, S. (2009). T1 weighted brain images at 7 Tesla unbiased for Proton Density, T2* contrast and RF coil receive B1 sensitivity with simultaneous vessel visualization. *Neuroimage* 46, 432–446. doi: 10.1016/j.neuroimage.2009. 02.009

Van Essen, D. C., Drury, H. A., Dickson, J., Harwell, J., Hanlon, D., and Anderson, C. H. (2001). An integrated software suite for surface-based analyses of cerebral cortex. *J. Am. Med. Inform. Assoc.* 8, 443–459. doi: 10.1136/jamia.2001. 0080443

Voss, P., Pike, B. G., and Zatorre, R. J. (2014). Evidence for both compensatory plastic and disuse atrophy-related neuroanatomical changes in the blind. *Brain* 137(Pt 4), 1224–1240. doi: 10.1093/brain/awu030

Wang, J., Qiu, M., and Constable, R. T. (2005). *In vivo* method for correcting transmit/receive nonuniformities with phased array coils. *Magn. Reson. Med.* 53, 666–674. doi: 10.1002/mrm.20377

Zatorre, R. J., Fields, R. D., and Johansen-Berg, H. (2012). Plasticity in gray and white: neuroimaging changes in brain structure during learning. *Nat. Neurosci.* 15, 528–536. doi: 10.1038/nn.3045

Chapter 3: Age-related mapping of intracortical myelin from late adolescence to middle adulthood using T₁-weighted MRI

Preamble

It is well known that the cortex changes structurally with age. Cortical thickness decreases linearly with age through adulthood (Fjell et al., 2009; Thambisetty et al., 2010), with the decline starting as early as the fifth year of age (Ducharme et al., 2016). While synaptic density decreases significantly during early development, it remains constant through adulthood (Huttenlocher, 1979). There also appears to be no change in the density or number of neurons in the cortex (Haug & Eggers, 1991; Terry, DeTeresa, & Hansen, 1987). It is conceivable that cortical thickness is tracking the neuronal cell body shrinkage with aging (Haug & Eggers, 1991; Terry et al., 1987) in addition to a decrease in oligodendrocytes (Pelvig, Pakkenberg, Stark, & Pakkenberg, 2008).

Myelin's structural integrity is known to be interconnected with age through adulthood. It has been found that oligodendrocytes decrease in number with age, where other glial cells do not show the same rate of age-related decline (Pelvig et al., 2008). Most of the work investigating the effects of aging on structural integrity of myelin has been performed in rhesus monkeys. Myelin has been found to increase in diameter, despite axonal diameter remaining constant with aging (Peters, Sethares, & Killiany, 2001). Other age-related myelin alterations include ballooning of sheaths, splitting of dense lines to accommodate dense oligodendrocyte cytoplasm, the formation of redundant myelin and the creation of double sheaths, where one sheath is surrounded by

another (Peters, Moss, & Sethares, 2000). Ultimately, these processes are increasing the amount of myelin surrounding the axons with age.

Middle adulthood marks an important period of development, as this is generally where the brain begins to see both structural and functional declines. Thus, a thorough characterization of the age-related changes that occur during this period of life may lead to interventions that will improve a person's quality of life through late adulthood and old age. At the opposing end of the range, early adulthood is a period of interest to mental health research, as it is the typical onset for many major mental disorders (Kessler et al., 2005). Understanding how the brain is changing during this period will inevitably help researchers better understand changes in many mental illnesses, ultimately leading to better treatment options. In **Chapter 3**, we aim to characterize intracortical myelin through middle adulthood to map the association of ICM with age. To map this age-related trajectory, methodology has moved from that of Chapter 2 involving myelinated cortical thickness, to intracortical signal analysis. A primary driver of this change was the evidence that intracortical signal is more sensitive to age related changes (Grydeland et al., 2013) compared to cortical thickness (Fjell et al., 2009). Fortunately, methods for the group analysis of signal on the cortical surface also became available over the course of this study (Tardif et al., 2015). The research presented in this Chapter thus continues to use T₁W imaging with enhanced ICM contrast, with a new processing pipeline to directly use the image intensity to make inferences about changing myelin levels with cortical maturation.

References

- Ducharme, S., Albaugh, M. D., Nguyen, T.-V., Hudziak, J. J., Mateos-Pérez, J. M., Labbe, A., et al. (2016). Trajectories of cortical thickness maturation in normal brain development--The importance of quality control procedures. *NeuroImage*, 125, 267–279. <http://doi.org/10.1016/j.neuroimage.2015.10.010>
- Grydeland, H., Walhovd, K. B., Tamnes, C. K., Westlye, L. T., & Fjell, A. M. (2013). Intracortical Myelin Links with Performance Variability across the Human Lifespan: Results from T1- and T2-Weighted MRI Myelin Mapping and Diffusion Tensor Imaging. *Journal of Neuroscience*, 33(47), 18618–18630. <http://doi.org/10.1523/JNEUROSCI.2811-13.2013>
- Haug, H., & Eggers, R. (1991). Morphometry of the human cortex cerebri and corpus striatum during aging. *Neurobiology of Aging*, 12(4), 336–8– discussion 352–5.
- Huttenlocher, P. R. (1979). Synaptic density in human frontal cortex - developmental changes and effects of aging. *Brain Research*, 163(2), 195–205.
- Fjell, A. M., Westlye, L. T., Amlien, I., Espeseth, T., Reinvang, I., Raz, N., et al. (2009). High Consistency of Regional Cortical Thinning in Aging across Multiple Samples. *Cerebral Cortex*, 19(9), 2001–2012. <http://doi.org/10.1093/cercor/bhn232>
- Kessler, R. C., Berglund, P., Demler, O., Jin, R., Merikangas, K. R., & Walters, E. E. (2005). Lifetime prevalence and age-of-onset distributions of DSM-IV disorders in the National Comorbidity Survey Replication. *Archives of General Psychiatry*, 62(6), 593–602. <http://doi.org/10.1001/archpsyc.62.6.593>

- Pelvig, D. P., Pakkenberg, H., Stark, A. K., & Pakkenberg, B. (2008). Neocortical glial cell numbers in human brains. *Neurobiology of Aging*, 29(11), 1754–1762.
<http://doi.org/10.1016/j.neurobiolaging.2007.04.013>
- Peters, A., Moss, M. B., & Sethares, C. (2000). Effects of aging on myelinated nerve fibers in monkey primary visual cortex. *The Journal of Comparative Neurology*, 419(3), 364–376.
- Peters, A., Sethares, C., & Killiany, R. J. (2001). Effects of age on the thickness of myelin sheaths in monkey primary visual cortex. *The Journal of Comparative Neurology*, 435(2), 241–248.
- Terry, R. D., DeTeresa, R., & Hansen, L. A. (1987). Neocortical cell counts in normal human adult aging. *Annals of Neurology*, 21(6), 530–539.
<http://doi.org/10.1002/ana.410210603>
- Thambisetty, M., Wan, J., Carass, A., An, Y., Prince, J. L., & Resnick, S. M. (2010). Longitudinal changes in cortical thickness associated with normal aging. *NeuroImage*, 52(4), 1215–1223. <http://doi.org/10.1016/j.neuroimage.2010.04.258>

The material presented in this chapter is a representation of the following publication with permission from Wiley to reprint.

Rowley CD, Sehmbi M, Bazin PL, Tardif CL, Minuzzi L, Frey BN, Bock NA. Age-related mapping of intracortical myelin from late adolescence to middle adulthood using T1-weighted MRI. *Human brain mapping*. 2017 Jul 1;38(7):3691-703.

The only changes made were for thesis formatting and continuity purposes and copy editing.

Author List Contributions:

CD Rowley conducted image processing and analysis, and wrote the manuscript.

M Sehmbi recruited and imaged subjects for the experiment

PL Bazin provided code for the analysis of images

CL Tardif also provided code for image analysis

L Minuzzi contributed to the statistical analysis

BN Frey assisted in study design

NA Bock contributed to study design and writing of the manuscript

Christopher D. Rowley^{1*}, Manpreet Sehmbi¹, Pierre-Louis Bazin², Christine L. Tardif³,

Luciano Minuzzi^{1,4,5}, Benicio N. Frey^{1,4,5}, Nicholas A. Bock^{1,6}

¹McMaster Integrative Neuroscience Discovery and Study Program, McMaster
University, Canada, L8S 4K1

²Department of Neurology, Max Planck Institute for Human Cognitive and Brain
Sciences, Leipzig, Germany, 04103

³Brain Imaging Centre, Douglas Mental Health Institute; Department of Psychiatry,
McGill University, Montreal, QC, Canada, H4H 1R3

⁴Department of Psychiatry and Behavioural Neurosciences, McMaster University,
Hamilton, Ontario, Canada, L8S 4K1

⁵Mood Disorders Program and Women's Health Concerns Clinic, St. Joseph's
Healthcare, Hamilton, ON, Canada, L8K 3K7

⁶Department of Psychology, Neuroscience & Behaviour, McMaster University,
Hamilton, Ontario, Canada, L8S 4K1

* Corresponding Author

rowleycd@mcmaster.ca

1280 Main Street West,

Hamilton, Ontario, Canada

L8S4K1

Conflict of Interest: The authors declare no competing financial interests.

Funding: This project was supported by the Independent Investigator Award, Brain & Behaviour Research Foundation (Dr. Frey) and the AFP Innovations Award, Department of Psychiatry and Behavioural Neurosciences, McMaster University (Dr. Minuzzi).

Abstract

Magnetic resonance imaging (MRI) studies in humans have reported that the T_1 -weighted signal in the cerebral cortex follows an inverted “U” trajectory over the lifespan. Here, we investigated the T_1 -weighted signal trajectory from late adolescence to middle adulthood in humans to characterize the age-range when mental illnesses tend to present, and efficacy of treatments are evaluated. We compared linear to quadratic predictors of age on signal in 67 healthy individuals, 17-45 years old. We investigated 1/4, 1/2, and 3/4 depths in the cortex representing intracortical myelin (ICM), in the superficial white matter (SWM), and in a reference deep white matter tract. We found the quadratic fit was superior in all regions of the cortex, while signal in the SWM and deep white matter showed no global dependence on age over this range. The signal trajectory in any region followed a similar shape regardless of cortical depth. The quadratic fit was analyzed in 70 cortical regions to obtain the age of maximum signal intensity. We found that visual, cingulate and left ventromedial prefrontal cortices peak first around 34 years old, whereas motor and premotor areas peak latest at approximately 38 years. Our analysis suggests that ICM trajectories over this range can be modelled well in small cohorts of subjects using quadratic functions, which are amenable to statistical analysis, thus suitable for investigating regional changes in ICM with disease. This study highlights a novel approach to map ICM trajectories using an age range that coincides with the onset of many mental illnesses.

Highlights

- Evaluate modeling the T₁-weighted signal trajectory from 17-45 years of age using quadratic fits against age across the cortex at varying depths
- Show that the age-trajectory of T₁-weighted signal can be detected in clinically-feasible sample sizes
- Show using quadratic fit parameters that the signal peaks during the mid-late 30's across the cortex, but has no age dependence in superficial or deep white matter
- No statistical differences were found in the shape of the age-trajectory of T₁-weighted signal for any region at three different cortical depths
- K-means clustering was used to summarize development trends across the cortex

Keywords

Intracortical myelin; Aging; Magnetic Resonance Imaging; Cerebral Cortex

Abbreviations

AIC – Akaike Information Criterion

ARC - Autocalibrating Reconstruction for Cartesian imaging

BD – Bipolar Disorder

DSM – Diagnostic and Statistical Manual

FOV – Field of View

GLM – General Linear Model

GM – Grey Matter

ICM – Intracortical Myelin

RF – Radiofrequency

SLF – Superior Longitudinal Fasciculus

SWM – Superficial White Matter

WM – White Matter

3.1: Introduction

Myelin is a crucial substance in the nervous system that speeds the conduction of neural signals and has been suggested to play an important role in functional plasticity in the grey matter (GM) of the cerebral cortex (Gibson et al., 2014; Xiao et al., 2016). Multiple studies using high resolution magnetic resonance imaging (MRI) and matched histology have shown that it is possible to investigate intracortical myelin (ICM) in vivo using MRI (Bock, Kocharyan, Liu, & Silva, 2009; Dinse et al., 2015; Eickhoff et al., 2005; Fracasso, van Veluw, Visser, Luijten, Spliet, Zwanenburg, Dumoulin, & Petridou, 2016b; 2016a; Stüber et al., 2014). Myelin affects many MR tissue properties, and changes in a given MR parameter are taken as a surrogate marker for changes in the ICM content. While several different MR parameters have been demonstrated to effectively map ICM, we use strongly T1-weighted signal optimized for increased dynamic range within the cerebral cortex (Bock et al., 2013). We further divide the T1-weighted image by a proton density-weighted image to fully remove bias in the ICM map resulting from B1- inhomogeneity and reduce the bias resulting from B1+ inhomogeneity (Marques & Gruetter, 2013). This optimized protocol can potentially detect significant changes ICM in clinical studies in small cohorts of subjects better than protocols that have not been explicitly optimized for intracortical contrast. Finally, we use this MR contrast as a matched in vivo MRI and histology study in non-human primates showed that this image contrast is spatially correlated with the presence of ICM across the entire cortex (Bock et al., 2009) while another study extended this finding to postmortem human brains at 7T

(Fracasso, van Veluw, Visser, Luijten, Spliet, Zwanenburg, Dumoulin, & Petridou, 2016a).

MRI has long been used to visualize the myelin content of the cortex (Clark, Courchesne, & Grafe, 1992). Within the past decade, however, there has been an increased interest in using the MRI signal to study ICM. This includes studies that map the location and boundaries of cortical regions (De Martino et al., 2015; Dinse et al., 2015; Glasser & Van Essen, 2011; Lutti, Dick, Sereno, & Weiskopf, 2014; Sereno, Lutti, Weiskopf, & Dick, 2013), correlate ICM with cognitive measures (Grydeland, Walhovd, Tamnes, Westlye, & Fjell, 2013; Grydeland, Westlye, Walhovd, & Fjell, 2016; Vidal-Piñeiro et al., 2016; Westlye, Walhovd, Dale, Bjørnerud, et al., 2010b), and investigate changes in ICM in disease populations (Iwatani et al., 2015; Schnack et al., 2016).

Myelination in the cortex develops into adulthood and the age-related trajectory of myelination differs across brain areas depending on their function (Bartzokis et al., 2001; 2004; Grydeland et al., 2013; Miller et al., 2012). It has been previously shown that ICM follows an inverted ‘U’ trajectory with normal aging with a rapid increase during childhood development, a slower increase into adulthood, and a decline with advanced age (Bartzokis, 2004; Grydeland et al., 2013). Using MRI methods that are sensitive to ICM, it is now possible to investigate this trajectory in vivo over the entire cortex.

The present study examines ICM in living humans from late adolescence to middle adulthood. Our intent is to characterize healthy ICM trajectories using a framework that allows future disease studies in this crucial age range where many severe mental diseases emerge and are treated in humans (Kessler et al., 2005). By using T1-

weighted images with strong ICM contrast, we investigate the myelin content of the cortex and explore the best fitting options to map the trajectory with age of intracortical myelin across the cortex. Characterizing the trajectory of ICM over the entire human lifespan requires fitting functions with complex shapes, such as splines (Fjell et al., 2010; Grydeland et al., 2013). However, we hypothesize that the limited age range we are characterizing in this study can be modelled using parametric linear (Shafee, Buckner, & Fischl, 2015) or quadratic fits, which allows age effects to be incorporated in statistical models using limited numbers of parameters. We also explore whether voxel-wise trajectories can be averaged over regions-of-interest (ROIs) across cortex without losing information. The advantage of investigating trajectories using ROIs is that it reduces the number of statistical tests one needs to compare signal trajectories in healthy and diseased groups across the cortex. Previous work has shown that it is possible to detect variations in signal across cortical depths (Fracasso, van Veluw, Visser, Luijten, Spliet, Zwanenburg, Dumoulin, & Petridou, 2016a; Sereno et al., 2013; Waehnert et al., 2016). We expand on this to investigate the trajectory of T1-weighted signal at three cortical depths ($\frac{1}{4}$, $\frac{1}{2}$ and $\frac{3}{4}$), as well as in the SWM to examine if the effects of ageing on this population are depth dependent. This is important to establish whether trajectories in ICM differ over depths of the cortex with differing myeloarchitecture, and whether the SWM follows a trajectory closer to ICM or myelin in deep white matter tracts. Finally, we explore development patterns by using k-means clustering to group the signal data based on commonalities in the age of maximum signal intensity across different regions of the

cortex. We determine and appropriate number of clusters to best represent and summarize general trends in ICM trajectory with age.

3.2: Methods

3.2.1: Subjects

This study was approved by the Hamilton Integrated Research Ethics Board and informed consent was obtained from each volunteer before enrolment. Images were collected in 67 right-handed, healthy individuals (30 males, 37 females) aged 17-45. All female subjects were pre-menopausal. Additional exclusion criteria included: unstable medical or general inflammatory conditions, alcohol/substance abuse within the last year (excluding caffeine or nicotine), past or current history of neurological disorders (including head trauma and migraines), and any MRI contraindications. Participants completed the Structured Clinical Interview for DSM-IV (SCID-I) to rule out current or lifetime psychiatric conditions.

3.2.2: Imaging

Images were acquired on a 3 T General Electric scanner (Software Version 22.0) using a 32-channel receive-only radiofrequency (RF) coil for the head (MR Instruments) and a transmit RF body coil (GE). All images were acquired with 1mm isotropic resolution. Images were acquired for anatomical reference, and to produce a T1-weighted image with optimized intracortical contrast for ICM analysis (Bock et al., 2013; Rowley et al., 2015).

3.2.2.1: Anatomical Reference Image

A 3D T_1 -weighted whole-head image was made using a 3D inversion-recovery gradient echo sequence (GE 3D BRAVO) [Inversion time = 450 ms, TE = 3.2 ms, TR in acquisition block = 8.4 ms, flip angle in acquisition block = 12° , field of view (FOV) = 25.6 x 25.6 x 25.6 cm, linear phase encoding, Autocalibrating Reconstruction for Cartesian imaging (ARC) parallel imaging factor of 2 in the second phase encode direction, Number of averages = 1, time = 5 min 32 s]. This image served as an anatomical reference for image registration.

3.2.2.2: T_1 -weighted Image

Another 3D T_1 -weighted whole-head image with strong intracortical contrast was made from four separate images collected with an inversion-recovery gradient echo sequence (GE 3D BRAVO) [Inversion time = 1100 ms, Time between end of acquisition block and next 180° pulse (TD) = 1000 ms, TE = 3.2 ms, TR in acquisition block = 8.4 ms, flip angle in acquisition block = 12° , FOV = 24.0 x 10 (selective slab in left/right direction) x 24.0 cm, centric phase encoding, ARC factor 2 in second phase-encoding direction, Number of averages = 1, time = 5 min 53 s]. Each hemisphere was imaged separately to increase intracortical contrast as this reduced the matrix dimension in the first phase-encoding direction in the sequence allowing for a shortened acquisition block following the inversion pulse. This is analogous to using multiple segments in a magnetization-prepared rapidly-acquired gradient echo sequence (MP-RAGE) (Deichmann, Good, Josephs, Ashburner, & Turner, 2000), where the shorter acquisition block improves contrast. The reduced-FOV was applied in this study since a true MP-

RAGE sequence was not available on our scanner. The long TD in the sequence provided increased intracortical contrast (Bock et al., 2013). Each hemisphere was imaged twice to increase the contrast-to-noise ratio. The four images took 24 minutes in total to acquire. Each of the four separate images was registered to the anatomical reference image via a 6-parameter rigid transformation with sinc resampling using the FLIRT tool in FSL (Jenkinson, Beckmann, Behrens, Woolrich, & Smith, 2012) Version 5.0 (fsl.fmrib.ox.ac.uk/fsl/, RRID:SCR_002823). The magnitude images were then summed to create the final image of the whole head.

3.2.2.3: Ratio Image

A final 3D proton density-weighted whole-head image was collected to correct intensity inhomogeneity in the T1-weighted image. This image was made with a 3D gradient-echo sequence (GE 3D SPGR) [parameters: TE = 3.1 ms, TR = 7.9 ms, flip angle = 4°, FOV = 24.0 x 17.4 x 24.0 cm, Number of averages = 1, time = 5 min 29 s].

The proton-density weighted image was registered to the T₁-weighted image using a 6-parameter rigid transform (FSL) and filtered with a 3D median filter with a 5 x 5 x 5 mm kernel size. The T1-weighted image was then divided by the filtered proton-density weighted image to create the ratio image, which is a strongly T1-weighted image with B1- and some B1+ inhomogeneities removed (Marques & Gruetter, 2013; van de Moortele et al., 2009; Wang, Qiu, & Constable, 2005).

3.2.3: Processing

Image processing was performed predominantly in MIPAV v7.0.1 software (mipav.cit.nih.gov, RRID:SCR_007371) using the JIST v3.0 (www.nitrc.org/projects/jist/, RRID:SCR_008887), TOADS-CRUISE vR3c (www.nitrc.org/projects/toads-cruise/, RRID:SCR_005977), and CBS High-Res Brain Processing Tools Version v3.0 (www.nitrc.org/projects/cbs-tools/, RRID:SCR_009452) plug-ins, and Amira v5.2 software (Visage Imaging, RRID:SCR_014305).

Processing began by creating a mask of the cerebrum using the T1-weighted image as an input to the SPECTRE 2010 algorithm (Carass et al., 2011) in MIPAV. This mask identifying the brain and dura matter was used to skull strip the Ratio image. The skull-stripped Ratio image was used as input to the Multiple Object Geometric Deformable Model (MGDM) Multi-contrast Brain Segmentation algorithm (Bazin et al., 2014; Bogovic, Prince, & Bazin, 2013) in MIPAV to generate initial probabilistic labels for tissue classes for each hemisphere of the brain. The probability labels generated for cerebral GM and white matter (WM) were used as input to the CRUISE algorithm (Han et al., 2004) to generate smoothed, topologically correct labels for the cerebrum, which was performed in each hemisphere separately.

Subcortical structures and ventricles (as identified by the MGDM algorithm) were then removed from the labels for the left and right cerebrums and the remaining labels combined. At this point, all GM segmentations were inspected and manual edits were made to replace missing cortex and to remove remaining dura mater arising from potential errors in the MGDM and CRUISE algorithms to ensure an accurate pial surface.

This label for the entire cerebrum without the subcortical structures was then used to mask the Ratio image such that it only contained the cerebral cortex and underlying major white matter tracts.

This corrected, cerebrum-masked Ratio image was next segmented into two main tissue classes: WM and GM, taking into account lightly and heavily myelinated components of GM (Rowley et al., 2015) using the FANTASM algorithm (Pham, 2001) in MIPAV. This yields a more accurate WM label for ICM analysis than the output from CRUISE. The hemispheres were segmented together to avoid potential hemispheric bias, such that the algorithm used the entire cerebrum for its classification. Following segmentations, labels for each tissue class were split back into left and right hemispheres for subsequent processing. The labels near the GM/WM-boundary were morphologically processed to remove all WM tissue not connected to the largest WM mass.

The corrected GM labels from CRUISE representing the pial surface, and WM labels from FANTASM representing the GM/WM boundary surface were used as inputs to a volume-preserving cortical depth model to generate intracortical surfaces at $\frac{1}{4}$, $\frac{1}{2}$ and $\frac{3}{4}$ cortical depths to sample the T1-weighted image signal (Waehnert et al., 2014) (Figure 3.1). An additional surface was generated 1mm from the GM/WM boundary into the WM to sample superficial white matter (SWM) intensity. Each surface was registered to the equivalent depth surface generated from the MNI-152 atlas using a multi-contrast multi-scale surface registration approach (Tardif et al., 2015). The signal was first sampled onto the individual subject's surface, which was then deformed to be in register with the MNI-152 equivalent surface.

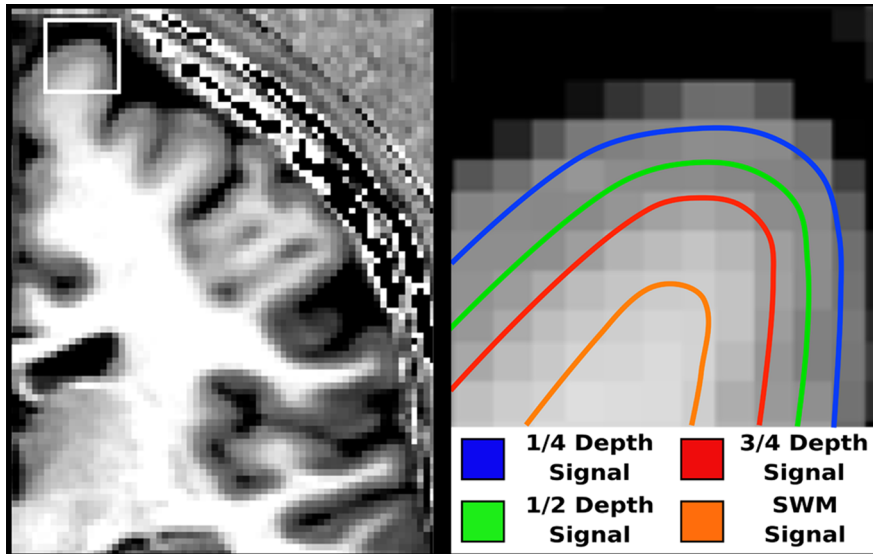


Figure 3.1: Representative illustration of measured T1-weighted signal at four depths.

Left: 1mm isotropic T1-weighted scan with high intracortical myelin contrast. Right: Four depth-dependent surfaces in and beneath the cortex, which sample the MRI signal. (SWM = superficial white matter)

3.2.4: Statistics

The MarsAtlas (Auzias, Coulon, & Brovelli, 2016) was used to parcellate the cortex into 82 regions-of-interest (ROIs) for analysis. The ICBM DTI-81 Atlas (Mori et al., 2008) was used to define an ROI in the superior longitudinal fasciculus, a deep WM tract that lies near the cortex. Statistical analysis was completed using R (<https://www.r-project.org>, RRID:SCR_001905) and cortical maps were created using Surfstat (<http://www.math.mcgill.ca/keith/surfstat/>, RRID:SCR_007081) in Matlab (v R2015a, RRID:SCR_001622). Signal intensity as a function of age was investigated for the ROIs using two general linear models (GLM) to compare linear to quadratic fits. The linear fit

used the predictors: Depth + Age + Gender, and the quadratic fit: Depth + Age + Age² + Gender, where Depth was the cortical depth of the sampling surface. A chi-square test was used to determine if there was a significant difference between the GLMs, and the Akaike information criterion (AIC) was used to determine which model provided a higher quality fit (Akaike, 1998). Six ROIs per hemisphere (twelve total) were not analyzed due to poor signal intensity profiles arising from topological errors in segmentations. These corresponded to the isthmus of the cingulate, the insula and regions of occipital and temporal lobes. The remaining 70 regions were used in the analysis to predict temporal shift of the quadratic model of signal intensity with age in all depths. The signal was averaged across each ROI and then fitted with predictors: Age + Age², to generate coefficients for a quadratic equation in the form: $y = Ax^2 + Bx + C$. The temporal shift, or the age where the maximum signal occurs is where $x = -B/2A$, which is obtained by taking the first derivative of the quadratic. The averaged ROI values were also fit with a smoothing spline using ggplot2 in R (using default values of stat_smooth with third order polynomial b-spline, loess fitting and span = 0.75), where the maximum signal and age at the signal of the fit were calculated. A k-means clustering algorithm was performed in MATLAB using four clusters to cluster the ROIs based on commonalities in the age of peak signal intensity in the middle depth. This was used to group the signal data to reduce the number of ROIs to show general trends of ICM trajectory with age across the cortex. The number of clusters was decided upon using the elbow method, such that adding additional clusters provided a diminishing change on the summed distance of the points to the centroids.

3.3 Results

3.3.1: Linear Versus Quadratic Fit

Gender was not found to be a significant predictor in either model in any ROI ($p > 0.05$) so it was not included for the remainder of the analysis. Quadratic models with age satisfied the conditions in all areas for the GLMs. GLMs also satisfied the conditions in nearly all regions (conditions satisfied if p of the model, normalized residuals tested with the Shapiro-Wilk test and homoscedasticity tests were all < 0.05).

A chi-square test was used to compare fit models in the ROIs for the $\frac{1}{2}$ depth signal and suggested a significant difference between the two general linear models ($p < 0.05$, Bonferonni corrected for 70 tests). AIC was used to test which model provided a higher quality fit. For all regions, AIC was lower in the quadratic model, signifying that the quadratic fit with Age was better than the linear fit. The two models are compared in Figure 3.2. A higher degree of variance, as shown by an increase in r^2 , is explained by the quadratic model across the cortex relative to the linear model. The p -value maps show similar significance for the models across the cortex, except for regions in the visual cortex where the linear model no longer fits significantly ($p > 0.05$). These maps were also created for the $\frac{1}{4}$ and $\frac{3}{4}$ cortical depths, and the quadratic fit universally provided a better data fit. SWM was the only sampling surface where neither the linear nor quadratic models provided a significant data fit across the brain.

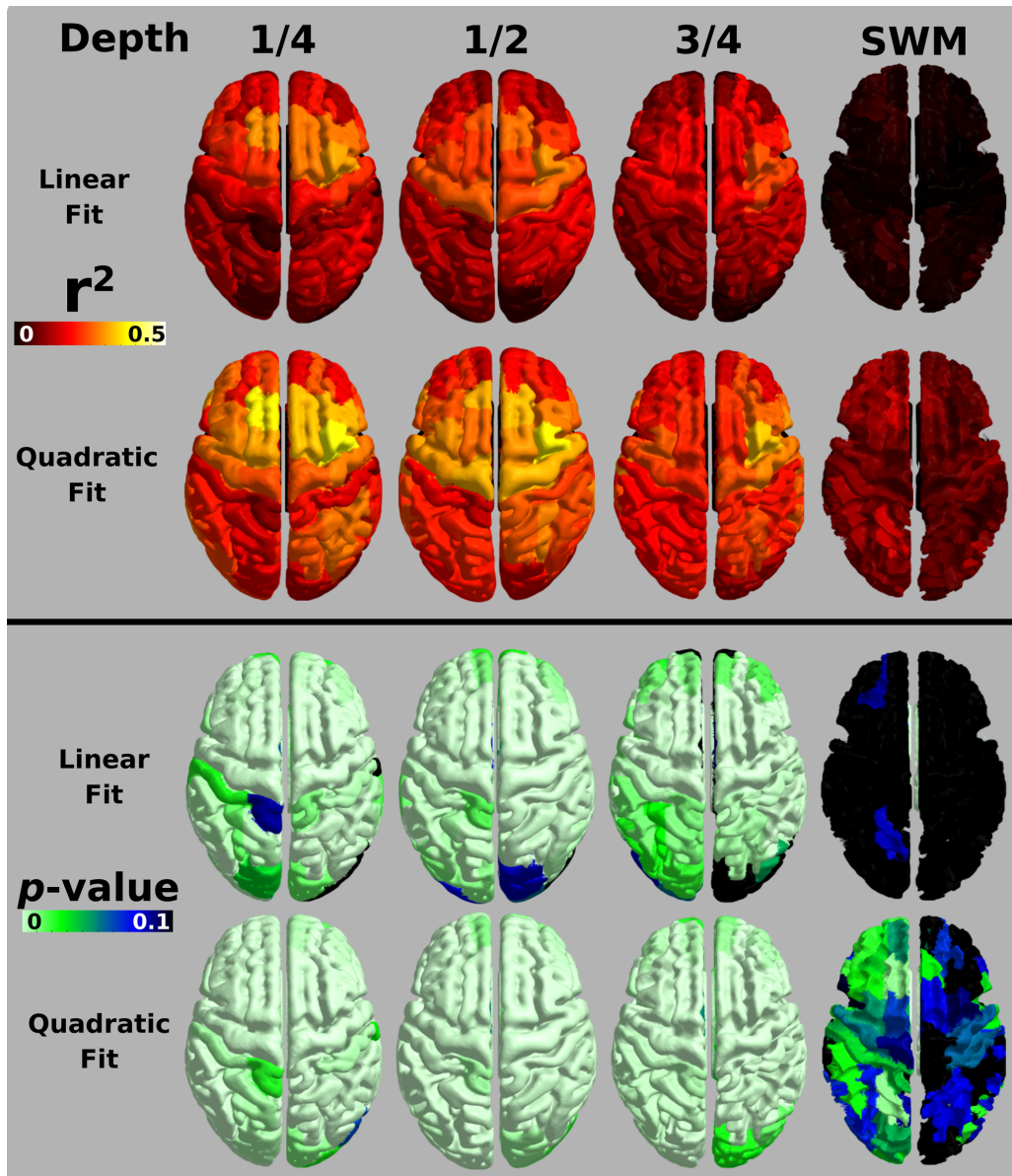


Figure 3.2: GLM fit metrics mapped across the brain. Top: r^2 values for MARS atlas ROIs with signal for the half-depth regressed against Age (linear) and Age² (quadratic). An increasing yellow hue in the map values indicates more variability is explained by the model fit. Bottom: p-value for the fit models. An increasing green hue in the map values depicts a more significant model fit.

Figure 3.3 illustrates the quadratic fit to the signal data points in the ROI defining the Caudal Dorsomedial Prefrontal Cortex. T₁-weighted signal across the age span is referenced against the signal found in the superior longitudinal fasciculus (SLF) in deep WM, which was found not to be correlated with age over the range used in this study.

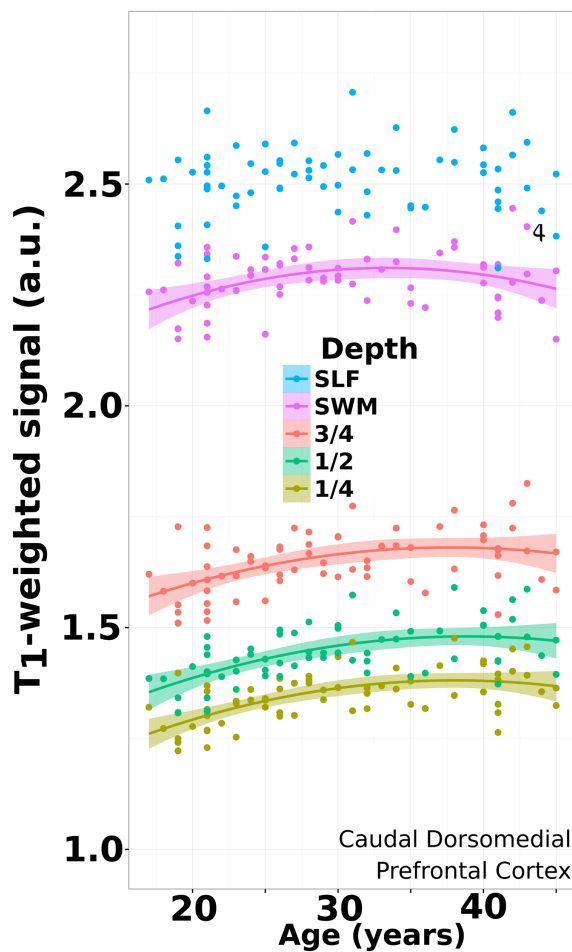


Figure 3.3: Age trajectory from superficial cortex to deep WM.

Data plotted for an ROI (Caudal Dorsomedial Prefrontal Cortex) in all subjects where the quadratic model fit the signal data at all depths. This is contrasted against the signal of a

volumetric ROI placed in the superior longitudinal fasciculus (SLF) in deep white matter, which demonstrated no significant effect with age over this range. Shaded regions denote the 95% confidence interval.

3.3.2: Estimating Maximum Value From Fits

Intercept values and coefficients for Age and Age² were calculated using the parameters estimated from the general linear model for all ROIs. This equation can be transformed into vertex form:

$$Ax^2 + Bx + C = A(x - h)^2 + k$$

where x is Age, h is the age where the maximum T1-weighted signal occurs, k is the maximal signal value reached, and A describes the shape of the trajectory. The graphical interpretation of h and k is illustrated in Figure 3.4 in the top left plot, and can be visualized in three additional ROIs at the three cortical depths. Figure 3.5 maps these values across the cortex both from vertex-wise fits and from fits of signal averaged over the ROIs. The signal maximum plots (k) resemble previously reported myelin maps derived from MRI (Bock et al., 2013; Dinse et al., 2015; Glasser & Van Essen, 2011; Lutti et al., 2014; Rowley et al., 2015; Waehnert et al., 2016), with high signal intensity in primary cortical areas, and lower intensity in association regions. The age where the signal reaches a maximum in the fit shows that the visual regions, cingulate and left ventromedial prefrontal cortex peak first, and the premotor and primary motor cortices peak last. Both maps of signal peak age (h) and peak signal value (k) show considerable regional variation, although the two metrics have distinct spatial patterns. The bottom

panel allows the visual comparison of h and k values extracted using a smoothing spline as an alternate fit. Over the age range we investigated, the quadratic and smoothing spline fits provide very similar maps of h and k over the cortex. A benefit of describing the trajectory using a quadratic model is the parameters can be incorporated into linear models for performing inferential statistics between populations of subjects. The benefit of a smoothing spline is that it would better capture trajectory if the age range were expanded beyond 17-45 years old (Fjell et al., 2010).

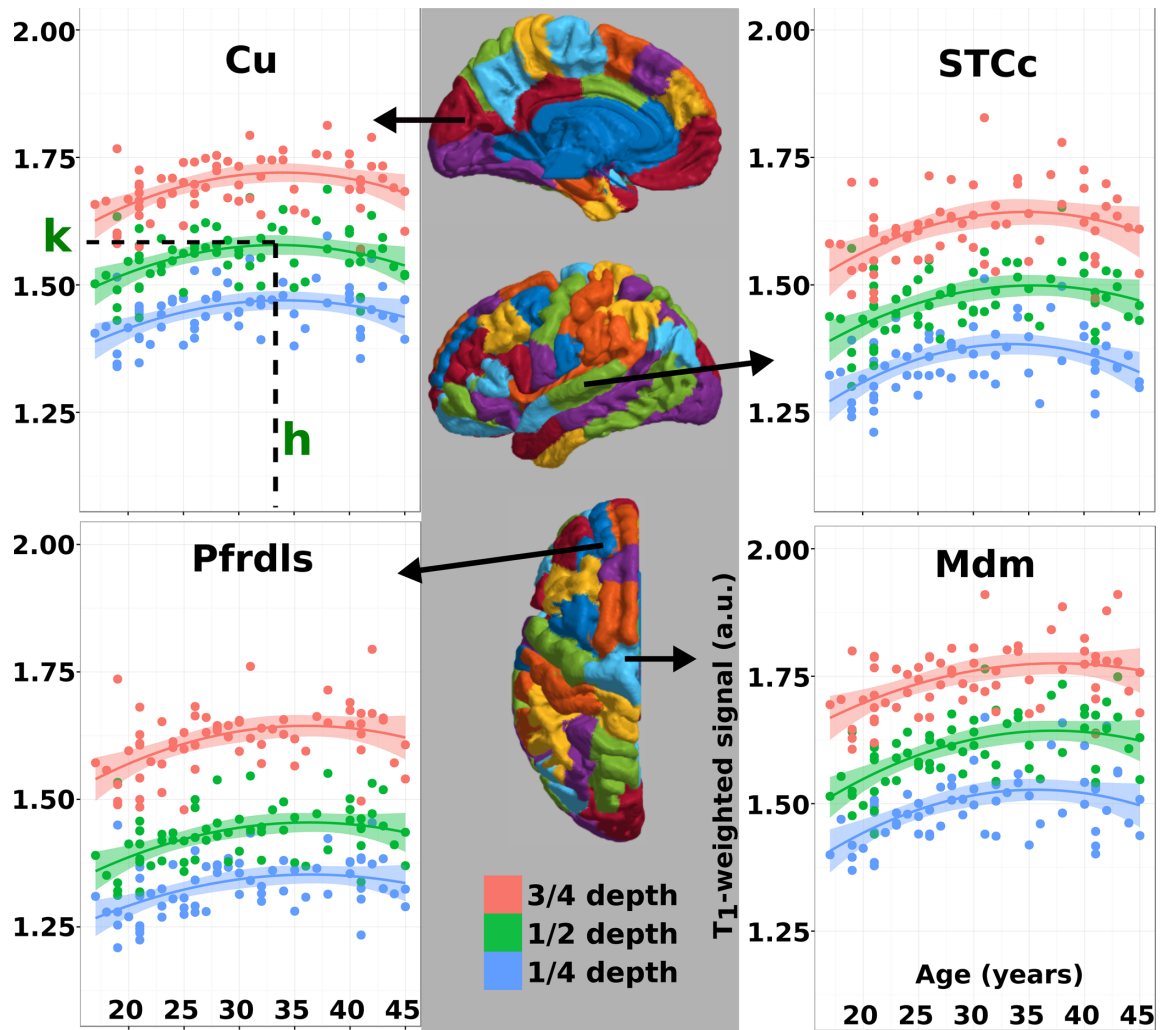


Figure 3.4: Four sample ROIs displaying the T1-weighted signal intensity values fit against age. Shading surrounding the quadratic fit line denotes the 95% confidence interval. Top left: Cuneus. Parameters extracted from the quadratic for further analysis are highlighted on this plot. ‘h’ is the age where the maximum signal occurs based on the quadratic fit. ‘k’ is the maximal signal achieved in this brain region. Top right: Caudal Superior Temporal Cortex. Bottom left: Rostral Dorsolateral Superior Prefrontal Cortex. Bottom right: Dorsomedial Motor Cortex.

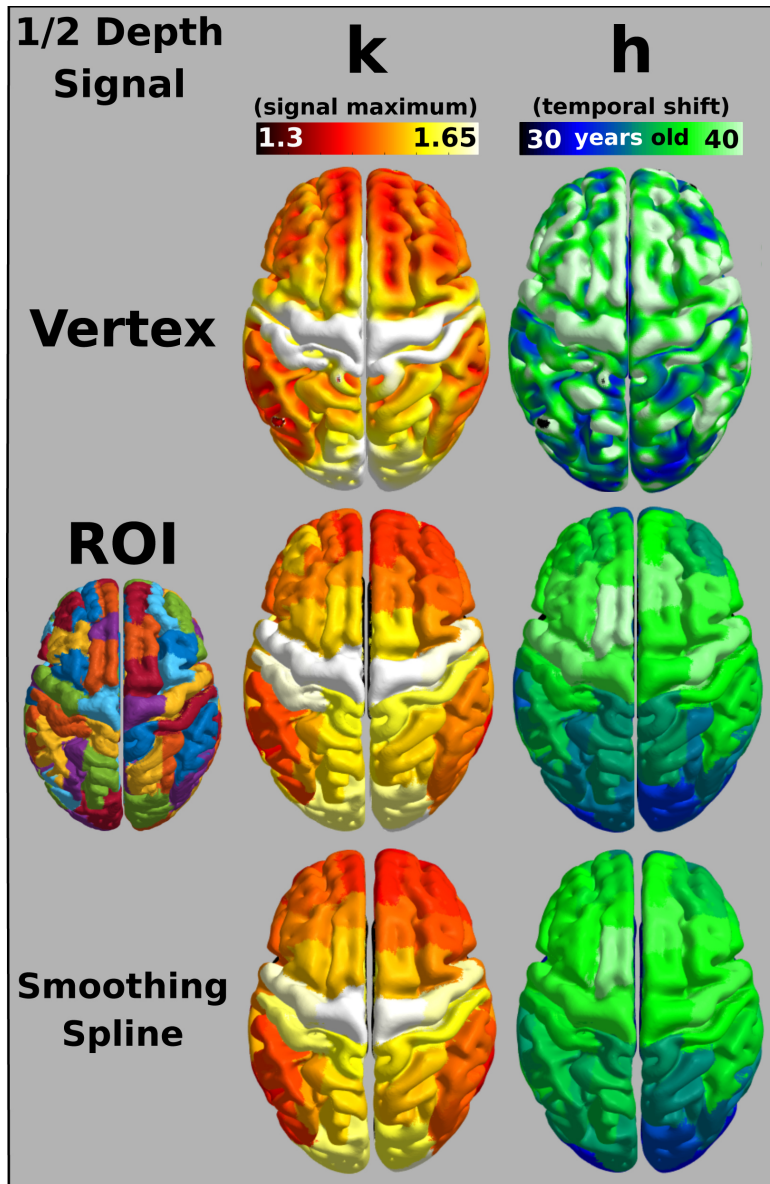


Figure 3.5: Mapping quadratic parameters across the cortex. Quadratic parameters calculated from the GLM fit shown for vertex-wise calculations and with signal first averaged across an ROI. Left: The maximum signal reached across the cortex as predicted by the quadratic model or using a smoothing spline (bottom). Right: The temporal shift of

the maximum signal value as estimated by the quadratic model, or by the smoothing spline (bottom), is mapped across the cortex.

The quadratic fit parameters were investigated across three different cortical depths and are summarized in Figure 3.6. An interaction term was added to the general linear model between Depth and Age to determine if there was a significant difference in the change of signal across age at the different depths. None of the interaction terms were found to be significant (all $p > 0.05$). The same maturation trend tracks across the cortex at the three cortical depths with visual areas and cingulate cortex reaching their fitted maximum first, and motor areas achieving their peak last. This suggests that ICM at different depths of the cortex follows the same age-related trajectory. The lack of a significant fit of either model across the SWM and SLF suggests myelination does not vary with age over the age range we investigated.

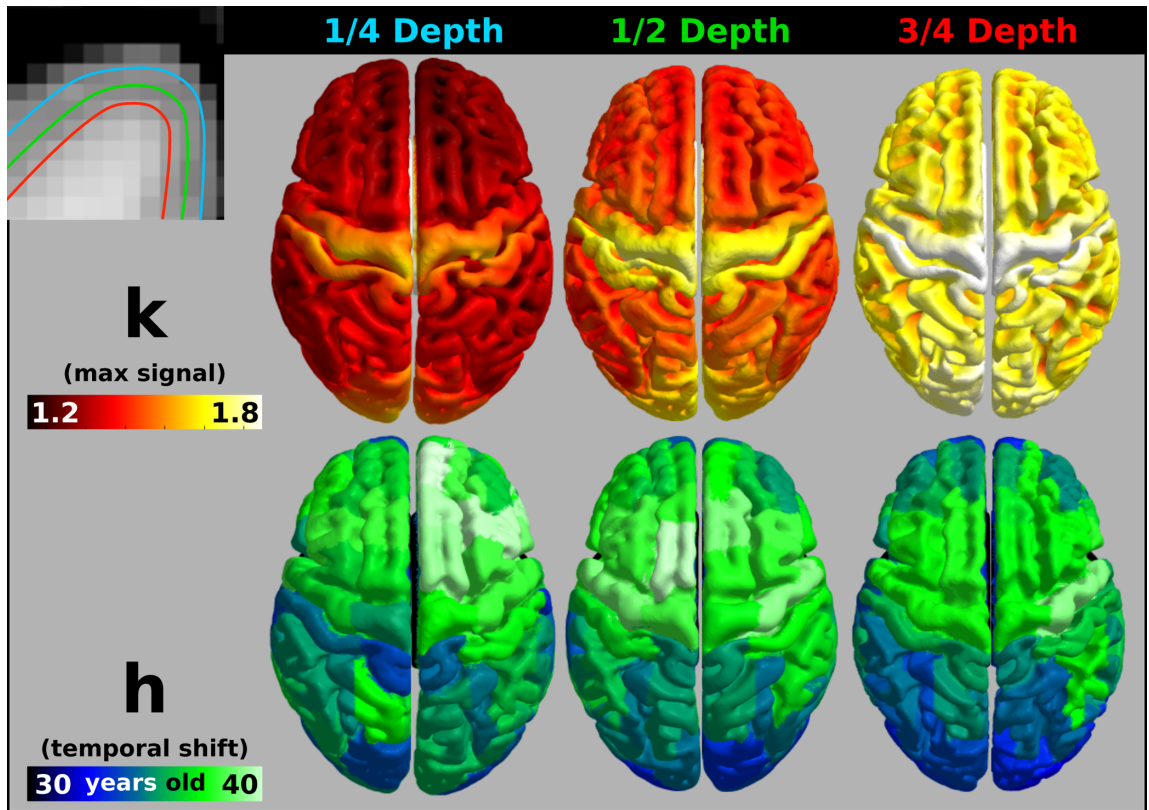


Figure 3.6: Calculated quadratic parameters across three cortical depths.

Top left: Illustration of the cortical sampling surfaces overlaid on the T_1 -weighted image.

Top row: The maximum signal for each vertex at each depth (voxel-wise). Bottom row: The temporal shift of the quadratic fit of the signal intensity with age (averaged over ROI).

3.3.3: Summarizing Trajectories Across the Cortex Using K-Means Clustering

The age of the peak signal, h , for the ROIs was analyzed using a k-means algorithm with four clusters to visualize regional commonalities across the cortex. Four clusters were chosen for our analysis using the elbow method by plotting the summed distance to the centroids against the number of clusters, and selecting the cluster where adding additional clusters provided little increase in explained variance in the data

(Supplementary Figure 3.8). We also found that this number qualitatively best summarized global trends in ROIs across the cortex. The results of the clustering are illustrated in Figure 3.7. Interestingly, the four clusters localized fairly well to the visual and cingulate cortices, frontal pole and parietal and temporal cortices, prefrontal cortex, and pre-motor and motor cortices. Signal values were then z-scored within the cluster to allow a better visualization of a shift along the age axis, and to display the relative variance seen within each cluster. The plot reveals the earliest peaking cluster is the one that includes the visual, cingulate and left ventromedial prefrontal cortices, which reaches its maximum value around age 34. The next cluster to peak contains the frontal pole, parietal and temporal cortices and occurs around 35 years of age. Subsequently, the cluster containing prefrontal and primary sensory cortices peaks just following 36 years of age, and the cluster containing the motor and premotor areas reach a maximum at age 38.

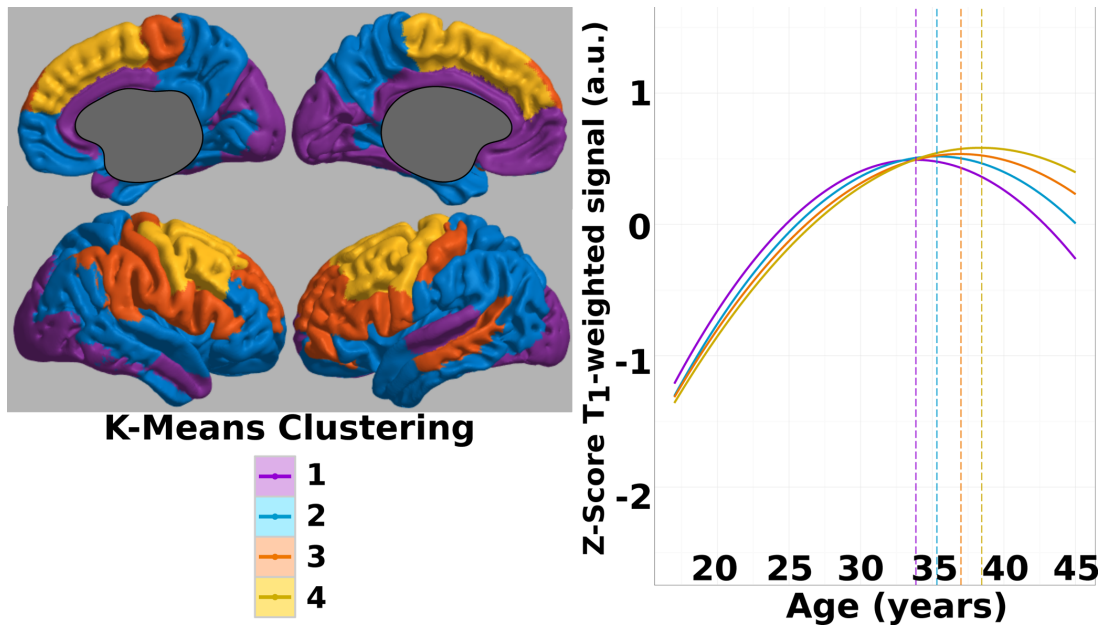
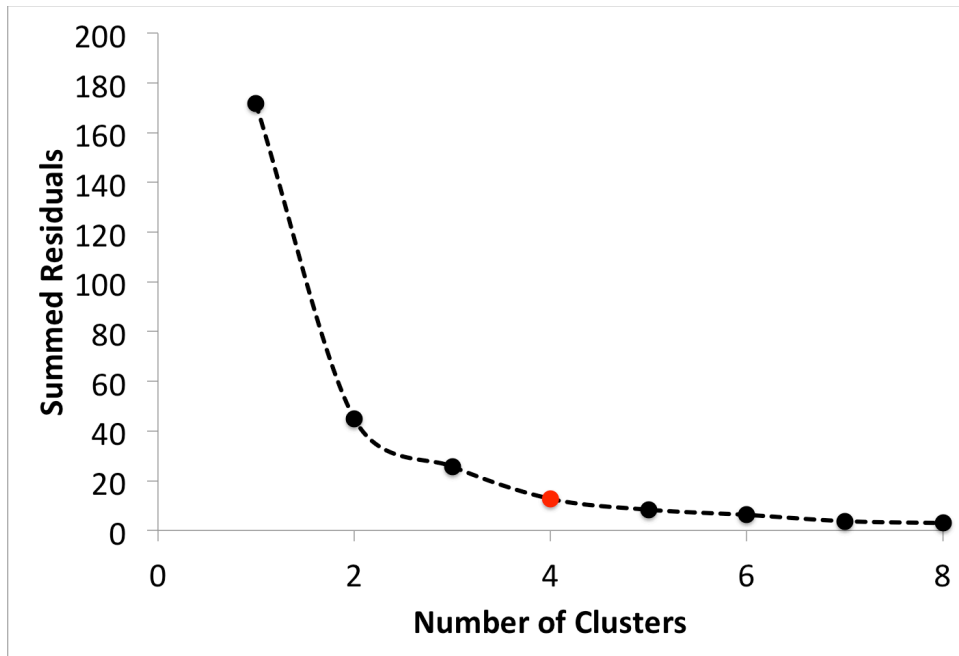


Figure 3.7: K-means clustering on peak age signal. Left: K-means clustering of ROIs into four clusters based on the age when the maximal T_1 -weighted signal is reached. Right: The signal values in all ROIs within each cluster were averaged, then Z-scores were calculated within each cluster to visualize the signal trajectory. Plotted solid lines highlight the quadratic fit for the half cortical depth signal. Temporal shift (vertical dotted line) increases from cluster 1 to cluster 4.



Supplementary Figure 3.8: The number of clusters used in the k-means ROI grouping, and the resulting summed distance to the centroids from each data point. The summed residuals was used as a marker of explained variance. Four clusters was chosen using the elbow method, such that adding more clusters provided a very small decrease in explained variance, and removing clusters added much more.

3.4 Discussion

We have demonstrated that the T_1 -weighted signal in cortical regions follows a trajectory that can be consistently modeled as a quadratic function of age over all regions of the cortex in subjects aged 17-45. Furthermore, we show that age-related trajectories can be observed in a relatively small cohort of healthy controls making the technique suitable for future clinical studies. If one takes changes in T_1 -weighted MRI signal to represent changes in ICM, then one can summarize ICM trajectories using two estimates

from the fit: signal peak age (h) and peak signal value (k). The map of peak signal value (k) over the cortex corresponds well with maps from a number of studies of MR parameters thought to be correlated with ICM amounts. The map of signal peak age (h) paints an important picture of how ICM develops from late adolescence, through early and into middle adulthood in humans. ICM development is important to examine in this range, as it coincides with the age of onset of many psychiatric disorders and subsequent treatment, such that developing atlases depicting h in large numbers of subjects would create a useful comparative data set.

Overall, we found that the trajectory in T_1 -weighted signal with age was similar over the depths of the cortex we investigated ($\frac{1}{4}$, $\frac{1}{2}$, and $\frac{3}{4}$ depths), despite the fact that myelin amounts differ significantly over the cortical layers. Specifically, the density of myelinated fibres is much higher in the deepest layers of the cortex (Layers IV-VI) relative to the shallower layers. This can be seen in our maps of the peak signal intensity, k , which increases in value over all regions when moving from the $\frac{1}{4}$ to the $\frac{3}{4}$ depth, which compares to the three cortical depth T_1 maps reported by Waehnert et al. (Waehnert et al., 2016). This depth-dependent analysis is dependent on accurate GM and WM surfaces in order to define the appropriate intracortical surfaces. We manually inspected all GM segmentations and made corrections where required to ensure accurate tissue classification. Accurate segmentations decreases the observed variance and helps to increase statistical power, which would be increasingly important when trying to compare different populations. The lack of depth dependence in our age trajectories suggests that ICM is gained and lost globally in the same manner over all depths of the cortex,

regardless of their underlying myeloarchitecture. We also investigated the T_1 -weighted signal in the SWM representing myelinated short association fibres, and found no correlation with age, which suggests that the myelin in SWM matures before ICM and is thus similar to myelinated long association fibres in deep white matter tracts.

In Figure 5, we show maps of k and h calculated from quadratic fits to vertex-wise trajectories and from fits to trajectories averaged first in 70 ROIs. There is little loss in specificity in the k ROI maps and some loss of specificity in the h ROI maps; however, it would be advantageous in future studies comparing k and h between healthy and diseased groups using ROIs because the number of statistical comparisons is reduced versus vertex-wise studies.

It was previously shown that over an age range of 18-35 years old, the T_1 -weighted/ T_2 -weighted signal follows a linear trajectory with age (Shafee et al., 2015). Our age range is extended to 45 years old, revealing a middle-adulthood plateau in the signal trajectory; thus we found that a quadratic model fit our T_1 -weighted signal significantly better than a linear model. If the age range of subjects extends from childhood to late adulthood, however, then simple linear or quadratic functions no longer accurately fit the T_1 -weighted signal trajectory with age in all regions. This is because a quadratic fit fails to capture steep increases in ICM in the early period of neurodevelopment (Barkovich, Kjos, Jackson, & Norman, 1988; Brody, Kinney, Kloman, & Gilles, 1987), the middle age plateau, and sharp declines during neurodegeneration in old age (Vidal-Piñeiro et al., 2016; Westlye, Walhovd, Dale, Bjørnerud, et al., 2010a; Westlye, Walhovd, Dale, Bjørnerud, et al., 2010b). In fact, Fjell et al. have warned of the interpretation of quadratic

fits to signal data over the entire lifespan as a large signal decrease in old age biases the fit and the following calculated metrics derived from the fit (Fjell et al., 2010). The ICM trajectory over the entire lifespan is undeniably better fit with functions comprising greater numbers of parameters, such as splines, which can better capture the shape. As such, previous MRI studies of ICM trajectories over a broader human age range have used spline functions to describe age effects. Although splines fit data well over the entire life span, their use makes regional or group-group comparisons difficult, and statistically expensive due to their piece-wise nature; therefore, it is preferable to use a simpler fit function if it is warranted. Here we have displayed that from the age range of 17-45, we collect very similar results using fewer fitting parameters.

In comparing our results to other work on cortical development and maturation, a previous study using T₁-weighted MRI in subjects aged 8-85 found a peak age roughly between 20-30 years of age by fitting the signal data with splines (Westlye, Walhovd, Dale, Bjørnerud, et al., 2010b). Despite the differences in imaging, data fitting and subject demographics, the development pattern was consistent with our findings with visual areas peaking earliest, cingulate cortices following shortly after, and motor and premotor areas peaking latest. In our study, where age was limited and didn't include childhood development or neurodegeneration, we have illustrated a framework that allows for statistical comparisons of trajectories between regions based on quadratic fitting and a simple comparison of h . We did not see any significant regional differences between cortical depths in estimated peak myelin age at the resolution we used for imaging. This suggests that myelination over the different depths of the cortex follows a

common trajectory with age, although this finding could be reinforced using higher resolution imaging more specific to the fine structural layering of the cortex.

The increase in T_1 -weighted signal we observed over late adolescence and early adulthood may be tracking an increase in myelin density per voxel – this could either arise from an increase in the number of myelinated axons in the cortex, or an increase in the caliber of existing sheaths. There is no comprehensive data in humans describing which features of myeloarchitecture in specific cortical regions change over the lifespan. In rhesus monkeys, however, it has been shown that oligodendrocytes show greater change with age than neurons (Peters et al., 2000), and although cortical axons do not change in size with age, the myelin sheath surrounding them increases in diameter (Peters et al., 2001). Thus, the increase in T_1 -weighted signal we observe could be reflecting increases in sheath thickness. The peak age observed in our data could reflect a turning point where myelin starts to degrade faster than it is produced. Our calculated peak age agrees with a previous study in humans looking at peak glucose consumption in the brain with age (Pardo et al., 2007). While myelin is known to be important in providing energy to the axons they insulate (Fünfschilling et al., 2013; Lee et al., 2013; Morrison, Lee, & Rothstein, 2013; Rinholm et al., 2011), it also requires large amounts of energy to build and maintain (Harris & Attwell, 2012), such that a slowing of myelin production would coincide with a reduction in glucose consumption. Xi et al. previously reported a significant decrease in conduction velocity of pyramidal tract neurons in aged cats, compared to young controls (Xi, Liu, Engelhardt, Morales, & Chase, 1999). Since myelin is important in speeding the conduction of neural signals, this finding could be reporting a

decrease in the quantity or quality of myelin on those neurons. These studies suggest that the T_1 -weighted signal trajectories are reporting ICM amounts over the age range we investigated, however, more histology work is needed to confirm how the specific features of myeloarchitecture evolve with age in the human cerebral cortex.

Our study suggests that ICM matures earliest in visual and cingulate cortices, with the rest of the cortex maturing up to four years later. While we found ICM to be globally dependent on age, SWM was not. Visual inspection of T_1 -weighted/ T_2 -weighted signal plots by Grydeland et al., depict a larger plateau in signal at middle age adulthood in the SWM in many regions compared to intracortical plots (Grydeland et al., 2013), reinforcing our findings in this narrowed age range. A study using diffusion tensor imaging (DTI) parameters to investigate SWM from 18-74 years of age noted that effects were prominently linear with age, with some quadratic effects, potentially due to a middle age plateau (O. R. Phillips et al., 2013). A cross sectional examination investigating white matter maturation with MRI-based DTI showed that fractional anisotropy (FA) increases at least up until 30 years of age (Lebel, Walker, Leemans, Phillips, & Beaulieu, 2008), while an additional study uncovered data peaks around 30 years of age in white matter DTI measurements (Westlye, Walhovd, Dale, Bjornerud, et al., 2010a). More recently, Nazeri et al., found a widespread age association with fractional anisotropy in SWM (Nazeri et al., 2015), but we believe our selected age range was too narrow to uncover this using our method. In humans, a histological investigation on the myelin in the stria of Gennari found a similar peak of myelin into the third decade of life (Lintl & Braak, 1983). Together, this evidence suggests that the cortex may continue to myelinate after

the adjacent WM has finished or plateaued. Also this suggests that a larger age range may be necessary to investigate changes in SWM age trajectories.

We observed a rostro-caudal maturation pattern in the prefrontal cortex (PFC), which was reinforced with our k-means clustering; regions near the frontal pole belong to the earliest peaking clusters, 1 and 2, regions near the dorsolateral prefrontal cortex peak later in cluster 3, and motor, premotor and regions in the superior medial prefrontal cortex peak latest and belong to cluster 4 (Figure 7). This matches a known structural gradient that exists in the rostral-caudal orientation of the PFC, such that in moving from caudodorsal to rostroventral, there is a gradual decrease in the number of fibres, in the calibre of fibres, and in cortical width (Nieuwenhuys, 2012). There is also an increase in myelination in the rostro-caudal direction (Thiebaut de Schotten et al., 2016). The functional significance of this gradient was extensively reviewed previously (Badre & D'Esposito, 2009) and it was suggested that hierarchical processing exists in the PFC, with more abstract thoughts being processed rostrally, and more concrete thoughts that are closer to producing a motor output being processed caudally. It is possible that the sequential processing is reflected in the myelination process as the circuits more rostral myelinate to completion before their downstream targets.

3.5 Conclusion

We have demonstrated that T_1 -weighted signal maps the trajectory with age of ICM in healthy young adults using a quadratic model. Considering that this age range coincides with the age of onset of major psychiatric disorders (Kessler et al., 2005), our

method may be useful to detect potential changes in ICM trajectories in disorders thought to be involved with abnormalities in myelin/oligodendrocyte maturation such as schizophrenia (Bartzokis et al., 2012; 2009), depression (Lake et al., 2016), and bipolar disorder (Rowley et al., 2015). It may be also useful to link the development of specific cortical regions with behavioural/cognitive functioning in humans over the range from late adolescence to middle adulthood. Early work has been done to correlate a T_1 -/ T_2 -weighted ratio signal, another contrast correlated with ICM, and intraindividual variability and error processing (Grydeland et al., 2013; 2016). Such combined studies could shed light on the functional impact of the myelin trajectory, and provide a biological mechanism to support different cognitive processes and patterns (Craik & Bialystok, 2006).

References

- Akaike, H. (1998). Information Theory and an Extension of the Maximum Likelihood Principle. In *Selected Papers of Hirotugu Akaike* (pp. 199–213). New York, NY: Springer New York. http://doi.org/10.1007/978-1-4612-1694-0_15
- Auzias, G., Coulon, O., & Brovelli, A. (2016). MarsAtlas: A cortical parcellation atlas for functional mapping. *Human Brain Mapping, 37*(4), 1573–1592. <http://doi.org/10.1002/hbm.23121>
- Badre, D., & D'Esposito, M. (2009). Is the rostro-caudal axis of the frontal lobe hierarchical? *Nature Reviews. Neuroscience, 10*(9), 659–669. <http://doi.org/10.1038/nrn2667>

- Barkovich, A. J., Kjos, B. O., Jackson, D. E., & Norman, D. (1988). Normal maturation of the neonatal and infant brain: MR imaging at 1.5 T. *Radiology*, *166*(1 Pt 1), 173–180. <http://doi.org/10.1148/radiology.166.1.3336675>
- Bartzokis, G. (2004). Quadratic trajectories of brain myelin content: unifying construct for neuropsychiatric disorders. *Neurobiology of Aging*, *25*(1), 49–62. <http://doi.org/10.1016/j.neurobiolaging.2003.08.001>
- Bartzokis, G., Beckson, M., Lu, P. H., Nuechterlein, K. H., Edwards, N., & Mintz, J. (2001). Age-related changes in frontal and temporal lobe volumes in men: a magnetic resonance imaging study. *Archives of General Psychiatry*, *58*(5), 461–465. <http://doi.org/10.1001/archpsyc.58.5.461>
- Bartzokis, G., Lu, P. H., Raven, E. P., Amar, C. P., Detore, N. R., Couvrette, A. J., et al. (2012). Impact on intracortical myelination trajectory of long acting injection versus oral risperidone in first-episode schizophrenia. *Schizophrenia Research*, *140*(1-3), 122–128. <http://doi.org/10.1016/j.schres.2012.06.036>
- Bartzokis, G., Lu, P. H., Stewart, S. B., Oluwadara, B., Lucas, A. J., Pantages, J., et al. (2009). In vivo evidence of differential impact of typical and atypical antipsychotics on intracortical myelin in adults with schizophrenia. *Schizophrenia Research*, *113*(2-3), 322–331. <http://doi.org/10.1016/j.schres.2009.06.014>
- Bartzokis, G., Sultzer, D., Lu, P. H., Nuechterlein, K. H., Mintz, J., & Cummings, J. L. (2004). Heterogeneous age-related breakdown of white matter structural integrity: implications for cortical “disconnection” in aging and Alzheimer’s disease.

Neurobiology of Aging, 25(7), 843–851.

<http://doi.org/10.1016/j.neurobiolaging.2003.09.005>

Bazin, P.-L., Weiss, M., Dinse, J., Schäfer, A., Trampel, R., & Turner, R. (2014). A computational framework for ultra-high resolution cortical segmentation at 7Tesla.

NeuroImage, 93(Part 2), 201–209. <http://doi.org/10.1016/j.neuroimage.2013.03.077>

Bock, N. A., Hashim, E., Janik, R., Konyer, N. B., Weiss, M., Stanisiz, G. J., et al. (2013).

Optimizing T1-weighted imaging of cortical myelin content at 3.0T. *NeuroImage*, 65, 1–12. <http://doi.org/10.1016/j.neuroimage.2012.09.051>

Bock, N. A., Kocharyan, A., Liu, J. V., & Silva, A. C. (2009). Visualizing the entire

cortical myelination pattern in marmosets with magnetic resonance imaging. *Journal of Neuroscience Methods*, 185(1), 15–22.

<http://doi.org/10.1016/j.jneumeth.2009.08.022>

Bogovic, J. A., Prince, J. L., & Bazin, P.-L. (2013). A Multiple Object Geometric

Deformable Model for Image Segmentation. *Computer Vision and Image*

Understanding : CVIU, 117(2), 145–157. <http://doi.org/10.1016/j.cviu.2012.10.006>

Brody, B. A., Kinney, H. C., Kloman, A. S., & Gilles, F. H. (1987). Sequence of central

nervous system myelination in human infancy. I. An autopsy study of myelination.

Journal of Neuropathology and Experimental Neurology, 46(3), 283–301.

Carass, A., Cuzzocreo, J., Wheeler, M. B., Bazin, P.-L., Resnick, S. M., & Prince, J. L.

(2011). Simple paradigm for extra-cerebral tissue removal: Algorithm and analysis.

NeuroImage, 56(4), 1982–1992. <http://doi.org/10.1016/j.neuroimage.2011.03.045>

- Clark, V. P., Courchesne, E., & Grafé, M. (1992). In vivo myeloarchitectonic analysis of human striate and extrastriate cortex using magnetic resonance imaging. *Cerebral Cortex*, 2(5), 417–424.
- De Martino, F., Moerel, M., Xu, J., van de Moortele, P.-F., Ugurbil, K., Goebel, R., et al. (2015). High-Resolution Mapping of Myeloarchitecture In Vivo: Localization of Auditory Areas in the Human Brain. *Cerebral Cortex*, 25(10), 3394–3405.
<http://doi.org/10.1093/cercor/bhu150>
- Deichmann, R., Good, C. D., Josephs, O., Ashburner, J., & Turner, R. (2000). Optimization of 3-D MP-RAGE Sequences for Structural Brain Imaging. *NeuroImage*, 12(1), 112–127. <http://doi.org/10.1006/nimg.2000.0601>
- Dinse, J., Härtwich, N., Waehnert, M. D., Tardif, C. L., Schäfer, A., Geyer, S., et al. (2015). A cytoarchitecture-driven myelin model reveals area-specific signatures in human primary and secondary areas using ultra-high resolution in-vivo brain MRI. *NeuroImage*, 114(C), 71–87. <http://doi.org/10.1016/j.neuroimage.2015.04.023>
- Eickhoff, S., Walters, N. B., Schleicher, A., Kril, J., Egan, G. F., Zilles, K., et al. (2005). High-resolution MRI reflects myeloarchitecture and cytoarchitecture of human cerebral cortex. *Human Brain Mapping*, 24(3), 206–215.
<http://doi.org/10.1002/hbm.20082>
- Fjell, A. M., Walhovd, K. B., Westlye, L. T., Østby, Y., Tamnes, C. K., Jernigan, T. L., et al. (2010). When does brain aging accelerate? Dangers of quadratic fits in cross-sectional studies. *NeuroImage*, 50(4), 1376–1383.

<http://doi.org/10.1016/j.neuroimage.2010.01.061>

Fracasso, A., van Veluw, S. J., Visser, F., Luijten, P. R., Spliet, W., Zwanenburg, J. J. M.,

Dumoulin, S. O., & Petridou, N. (2016a). Lines of Baillarger in vivo and ex vivo:

Myelin contrast across lamina at 7T MRI and histology. *NeuroImage*, *133*(C), 163–

175. <http://doi.org/10.1016/j.neuroimage.2016.02.072>

Fracasso, A., van Veluw, S. J., Visser, F., Luijten, P. R., Spliet, W., Zwanenburg, J. J. M.,

Dumoulin, S. O., & Petridou, N. (2016b). Myelin contrast across lamina at 7T, ex-

vivo and in-vivo dataset. *Data in Brief*, *8*(C), 990–1003.

<http://doi.org/10.1016/j.dib.2016.06.058>

Fünfschilling, U., Supplie, L. M., Mahad, D., Boretius, S., Saab, A. S., Edgar, J., et al.

(2013). Glycolytic oligodendrocytes maintain myelin and long-term axonal integrity.

Nature, *485*(7399), 517–521. <http://doi.org/10.1038/nature11007>

Gibson, E. M., Purger, D., Mount, C. W., Goldstein, A. K., Lin, G. L., Wood, L. S., et al.

(2014). Neuronal activity promotes oligodendrogenesis and adaptive myelination in

the mammalian brain. *Science (New York, N.Y.)*, *344*(6183), 1252304–1252304.

<http://doi.org/10.1126/science.1252304>

Glasser, M. F., & Van Essen, D. C. (2011). Mapping Human Cortical Areas In Vivo

Based on Myelin Content as Revealed by T1- and T2-Weighted MRI. *Journal of*

Neuroscience, *31*(32), 11597–11616. <http://doi.org/10.1523/JNEUROSCI.2180->

11.2011

Grydeland, H., Walhovd, K. B., Tamnes, C. K., Westlye, L. T., & Fjell, A. M. (2013).

- Intracortical Myelin Links with Performance Variability across the Human Lifespan: Results from T1- and T2-Weighted MRI Myelin Mapping and Diffusion Tensor Imaging. *Journal of Neuroscience*, 33(47), 18618–18630.
<http://doi.org/10.1523/JNEUROSCI.2811-13.2013>
- Grydeland, H., Westlye, L. T., Walhovd, K. B., & Fjell, A. M. (2016). Intracortical Posterior Cingulate Myelin Content Relates to Error Processing: Results from T1- and T2-Weighted MRI Myelin Mapping and Electrophysiology in Healthy Adults. *Cerebral Cortex*, 26(6), 2402–2410. <http://doi.org/10.1093/cercor/bhv065>
- Han, X., Pham, D. L., Tosun, D., Rettmann, M. E., Xu, C., & Prince, J. L. (2004). CRUISE: Cortical reconstruction using implicit surface evolution. *NeuroImage*, 23(3), 997–1012. <http://doi.org/10.1016/j.neuroimage.2004.06.043>
- Harris, J. J., & Attwell, D. (2012). The Energetics of CNS White Matter. *Journal of Neuroscience*, 32(1), 356–371. <http://doi.org/10.1523/JNEUROSCI.3430-11.2012>
- Iwatani, J., Ishida, T., Donishi, T., Ukai, S., Shinosaki, K., Terada, M., & Kaneoke, Y. (2015). Use of T1-weighted/T2-weighted magnetic resonance ratio images to elucidate changes in the schizophrenic brain. *Brain and Behavior*, 5(10), n/a–n/a. <http://doi.org/10.1002/brb3.399>
- Jenkinson, M., Beckmann, C. F., Behrens, T. E. J., Woolrich, M. W., & Smith, S. M. (2012). FSL. *NeuroImage*, 62(2), 782–790.
<http://doi.org/10.1016/j.neuroimage.2011.09.015>
- Lake, E. M. R., Steffler, E. A., Rowley, C. D., Sehmbi, M., Minuzzi, L., Frey, B. N., &

- Bock, N. A. (2016). Altered intracortical myelin staining in the dorsolateral prefrontal cortex in severe mental illness. *European Archives of Psychiatry and Clinical Neuroscience*, 1–8. <http://doi.org/10.1007/s00406-016-0730-5>
- Lebel, C., Walker, L., Leemans, A., Phillips, L., & Beaulieu, C. (2008). Microstructural maturation of the human brain from childhood to adulthood. *NeuroImage*, 40(3), 1044–1055. <http://doi.org/10.1016/j.neuroimage.2007.12.053>
- Lee, Y., Morrison, B. M., Li, Y., Lengacher, S., Farah, M. H., Hoffman, P. N., et al. (2013). Oligodendroglia metabolically support axons and contribute to neurodegeneration. *Nature*, 487(7408), 443–448. <http://doi.org/10.1038/nature11314>
- Lintl, P., & Braak, H. (1983). Loss of intracortical myelinated fibers: a distinctive age-related alteration in the human striate area. *Acta Neuropathologica*, 61(3-4), 178–182.
- Lutti, A., Dick, F., Sereno, M. I., & Weiskopf, N. (2014). Using high-resolution quantitative mapping of R1 as an index of cortical myelination. *NeuroImage*, 93(Part 2), 176–188. <http://doi.org/10.1016/j.neuroimage.2013.06.005>
- Marques, J. P., & Gruetter, R. (2013). New Developments and Applications of the MP2RAGE Sequence - Focusing the Contrast and High Spatial Resolution R1 Mapping. *PLoS ONE*, 8(7), e69294–11. <http://doi.org/10.1371/journal.pone.0069294>
- Miller, D. J., Duka, T., Stimpson, C. D., Schapiro, S. J., Baze, W. B., McArthur, M. J., et al. (2012). Prolonged myelination in human neocortical evolution. *Proceedings of the National Academy of Sciences of the United States of America*, 109(41), 16480–16485. <http://doi.org/10.1073/pnas.1117943109>

- Mori, S., Oishi, K., Jiang, H., Jiang, L., Li, X., Akhter, K., et al. (2008). Stereotaxic white matter atlas based on diffusion tensor imaging in an ICBM template. *NeuroImage*, *40*(2), 570–582. <http://doi.org/10.1016/j.neuroimage.2007.12.035>
- Morrison, B. M., Lee, Y., & Rothstein, J. D. (2013). Oligodendroglia: metabolic supporters of axons. *Trends in Cell Biology*, *23*(12), 644–651. <http://doi.org/10.1016/j.tcb.2013.07.007>
- Nazeri, A., Chakravarty, M. M., Rajji, T. K., Felsky, D., Rotenberg, D. J., Mason, M., et al. (2015). Superficial white matter as a novel substrate of age-related cognitive decline. *Neurobiology of Aging*, *36*(6), 2094–2106. <http://doi.org/10.1016/j.neurobiolaging.2015.02.022>
- Nieuwenhuys, R. (2012). The myeloarchitectonic studies on the human cerebral cortex of the Vogt–Vogt school, and their significance for the interpretation of functional neuroimaging data. *Brain Structure and Function*, *218*(2), 303–352. <http://doi.org/10.1007/s00429-012-0460-z>
- Pardo, J. V., Lee, J. T., Sheikh, S. A., Surerus-Johnson, C., Shah, H., Munch, K. R., et al. (2007). Where the brain grows old: decline in anterior cingulate and medial prefrontal function with normal aging. *NeuroImage*, *35*(3), 1231–1237. <http://doi.org/10.1016/j.neuroimage.2006.12.044>
- Pham, D. L. (2001). Robust fuzzy segmentation of magnetic resonance images. *Computer-Based Medical Systems*.
- Phillips, O. R., Clark, K. A., Luders, E., Azhir, R., Joshi, S. H., Woods, R. P., et al.

- (2013). Superficial White Matter: Effects of Age, Sex, and Hemisphere. *Brain Connectivity*, 3(2), 146–159. <http://doi.org/10.1089/brain.2012.0111>
- Rinholm, J. E., Hamilton, N. B., Kessaris, N., Richardson, W. D., Bergersen, L. H., & Attwell, D. (2011). Regulation of Oligodendrocyte Development and Myelination by Glucose and Lactate. *Journal of Neuroscience*, 31(2), 538–548. <http://doi.org/10.1523/JNEUROSCI.3516-10.2011>
- Rowley, C. D., Bazin, P.-L., Tardif, C. L., Sehmbi, M., Hashim, E., Zaharieva, N., et al. (2015). Assessing intracortical myelin in the living human brain using myelinated cortical thickness. *Frontiers in Neuroscience*, 9, 396. <http://doi.org/10.3389/fnins.2015.00396>
- Schnack, H. G., van Haren, N. E. M., Nieuwenhuis, M., Hulshoff Pol, H. E., Cahn, W., & Kahn, R. S. (2016). Accelerated Brain Aging in Schizophrenia: A Longitudinal Pattern Recognition Study. *American Journal of Psychiatry*, 173(6), 607–616. <http://doi.org/10.1176/appi.ajp.2015.15070922>
- Sereno, M. I., Lutti, A., Weiskopf, N., & Dick, F. (2013). Mapping the Human Cortical Surface by Combining Quantitative T1 with Retinotopy. *Cerebral Cortex*, 23(9), 2261–2268. <http://doi.org/10.1093/cercor/bhs213>
- Shafee, R., Buckner, R. L., & Fischl, B. (2015). Gray matter myelination of 1555 human brains using partial volume corrected MRI images. *NeuroImage*, 105(C), 473–485. <http://doi.org/10.1016/j.neuroimage.2014.10.054>
- Stüber, C., Morawski, M., Schäfer, A., Labadie, C., Wähnert, M., Leuze, C., et al. (2014).

- Myelin and iron concentration in the human brain: A quantitative study of MRI contrast. *NeuroImage*, *93*, 95–106. <http://doi.org/10.1016/j.neuroimage.2014.02.026>
- Tardif, C. L., Schäfer, A., Waehnert, M., Dinse, J., Turner, R., & Bazin, P.-L. (2015). Multi-contrast multi-scale surface registration for improved alignment of cortical areas. *NeuroImage*, *111*(C), 107–122. <http://doi.org/10.1016/j.neuroimage.2015.02.005>
- Thiebaut de Schotten, M., Urbanski, M., Batrancourt, B., Levy, R., Dubois, B., Cerliani, L., & Volle, E. (2016). Rostro-caudal Architecture of the Frontal Lobes in Humans. *Cerebral Cortex*, 1–15. <http://doi.org/10.1093/cercor/bhw215>
- van de Moortele, P.-F., Auerbach, E. J., Olman, C., Yacoub, E., Ugurbil, K., & Moeller, S. (2009). T1 weighted brain images at 7 Tesla unbiased for Proton Density, T2* contrast and RF coil receive B1 sensitivity with simultaneous vessel visualization. *NeuroImage*, *46*(2), 432–446. <http://doi.org/10.1016/j.neuroimage.2009.02.009>
- Vidal-Piñeiro, D., Walhovd, K. B., Storsve, A. B., Grydeland, H., Rohani, D. A., & Fjell, A. M. (2016). Accelerated longitudinal gray/white matter contrast decline in aging in lightly myelinated cortical regions. *Human Brain Mapping*, 1–16. <http://doi.org/10.1002/hbm.23267>
- Waehnert, M. D., Dinse, J., Schäfer, A., Geyer, S., Bazin, P.-L., Turner, R., & Tardif, C. L. (2016). A subject-specific framework for in vivo myeloarchitectonic analysis using high resolution quantitative MRI. *NeuroImage*, *125*(C), 94–107. <http://doi.org/10.1016/j.neuroimage.2015.10.001>

- Waehnert, M. D., Dinse, J., Weiss, M., Streicher, M. N., Waehnert, P., Geyer, S., et al. (2014). Anatomically motivated modeling of cortical laminae. *NeuroImage*, *93*(P2), 210–220. <http://doi.org/10.1016/j.neuroimage.2013.03.078>
- Wang, J., Qiu, M., & Constable, R. T. (2005). In vivo method for correcting transmit/receive nonuniformities with phased array coils. *Magnetic Resonance in Medicine*, *53*(3), 666–674. <http://doi.org/10.1002/mrm.20377>
- Westlye, L. T., Walhovd, K. B., Dale, A. M., Bjørnerud, A., Due-Tønnessen, P., Engvig, A., et al. (2010a). Life-Span Changes of the Human Brain White Matter: Diffusion Tensor Imaging (DTI) and Volumetry. *Cerebral Cortex*, *20*(9), 2055–2068. <http://doi.org/10.1093/cercor/bhp280>
- Westlye, L. T., Walhovd, K. B., Dale, A. M., Bjørnerud, A., Due-Tønnessen, P., Engvig, A., et al. (2010b). Differentiating maturational and aging-related changes of the cerebral cortex by use of thickness and signal intensity. *NeuroImage*, *52*(1), 172–185. <http://doi.org/10.1016/j.neuroimage.2010.03.056>
- Xi, M. C., Liu, R. H., Engelhardt, J. K., Morales, F. R., & Chase, M. H. (1999). Changes in the axonal conduction velocity of pyramidal tract neurons in the aged cat. *Neuroscience*, *92*(1), 219–225.
- Xiao, L., Ohayon, D., McKenzie, I. A., Sinclair-Wilson, A., Wright, J. L., Fudge, A. D., et al. (2016). Rapid production of new oligodendrocytes is required in the earliest stages of motor-skill learning. *Nature Neuroscience*, *19*(9), 1210–1217. <http://doi.org/10.1038/nn.4351>

Chapter 4: Altered Intracortical T₁-weighted/T₂-weighted ratio signal in Huntington's Disease

Preamble

This study investigated the utility of commonly-collected T₁W and T₂W images for ICM mapping in a clinical study of Huntington's disease (HD).

HD is neurodegenerative disorder caused by a polyglutamate repeat on the huntingtin (*HTT*) gene (MacDonald, Ambrose, Duyao, & Myers, 1993). *HTT* is required for development as was demonstrated in a study that knocked out the *HTT* gene homolog in mice, which proved lethal on embryonic day 8.5 (Nasir et al., 1995). The embryonic death can be prevented with the availability of huntingtin gene (White et al., 1997). The timing of the *in utero* death has lead to the suggestion that the protein plays a critical role in the embryonic development of the nervous system (Nasir et al., 1995; White et al., 1997).

The neurodegeneration of the striatum in HD is a characteristic feature of the progressive disease (Vonsattel et al., 1985). Structurally, this is a primary input to the basal ganglia, which is involved in regulating movement and cognitive functions (Han, You, Kordower, Brady, & Morfini, 2010). In the striatum, the medium spiny neurons (MSNs) are primarily affected by the mutant *HTT* (Reiner et al., 1988). MSNs are projection neurons that signal to other brain regions. It has also been noted that the cerebral cortex undergoes degeneration in HD. Pyramidal projection neurons, which are similar in morphology to MSNs, have been shown to be more vulnerable than other

cortical cells (Cudkowicz & Kowall, 1990). The vulnerability of these far-reaching projection cells in HD may explain the vast range of symptoms associated with the disease.

MRI is currently being used to study how the brain changes in HD prior to symptom onset. Degeneration of the striatum and WM have been shown to begin well before clinical diagnosis, using MRI (Bourbon-Teles et al., 2017; Dumas, van den Bogaard, et al., 2012a; Fennema-Notestine, Archibald, & Jacobson, 2004; Rosas et al., 2010). More recently, cortical thickness studies have shown this degeneration is mirrored in the cortex as well (Rosas et al., 2002; Tabrizi, Langbehn, Leavitt, & Roos, 2009). These findings suggest that the plasticity of the brain has a limited ability to compensate for the on-going brain atrophy in order to maintain functionality in affected patients (Dumas, van den Bogaard, et al., 2012a).

Numerous studies have suggested that myelin may play a part in the pathogenesis of HD. It was hypothesized that there is an early myelin breakdown, and subsequent overactive myelination (Bartzokis et al., 2007). This was suggested through work showing increased iron levels in the brain's of HD patients (Bartzokis et al., 2007; Bartzokis, Cummings, Perlman, Hance, & Mintz, 1999; Di Paola et al., 2013; Dumas, Versluis, et al., 2012b; Sánchez-Castañeda et al., 2014), and elevated oligodendrocyte densities (Myers et al., 1991; Rajkowska, Selemon, & Goldman-Rakic, 1998). Recently, a study combined DTI and quantitative magnetization transfer imaging to show a breakdown of myelin in the deep white matter in HD (Bourbon-Teles et al., 2017). Thus

in **Chapter 4**, I aimed to test the T₁W/T₂W ‘myelin’ mapping technique, using the imaging pipeline developed from the work in Chapter 3, in this HD population to investigate disease related changes in intracortical myelin. T₁W/T₂W imaging was utilized for this study as it uses commonly collected structural scans that often exist in neuroimaging databanks. This work also provides knowledge about the utility of using structural images that have not been specifically optimized for ICM contrast, to characterize changes in cortical composition.

References

- Bartzokis, G., Cummings, J., Perlman, S., Hance, D. B., & Mintz, J. (1999). Increased basal ganglia iron levels in Huntington disease. *Archives of Neurology*, *56*(5), 569–574.
- Bartzokis, G., Lu, P. H., Tishler, T. A., Fong, S. M., Oluwadara, B., Finn, J. P., et al. (2007). Myelin Breakdown and Iron Changes in Huntington’s Disease: Pathogenesis and Treatment Implications. *Neurochemical Research*, *32*(10), 1655–1664.
<http://doi.org/10.1007/s11064-007-9352-7>
- Bourbon-Teles, J., Bells, S., Jones, D. K., Coulthard, E., Rosser, A., & Metzler-Baddeley, C. (2017). Myelin breakdown in human Huntington's disease: Multi-modal evidence from diffusion MRI and quantitative magnetization transfer. *Neuroscience*.
<http://doi.org/10.1016/j.neuroscience.2017.05.042>
- Cudkovicz, M., & Kowall, N. W. (1990). Degeneration of pyramidal projection neurons in Huntington's disease cortex. *Annals of Neurology*, *27*(2), 200–204.

<http://doi.org/10.1002/ana.410270217>

Di Paola, M., Phillips, O. R., Sanchez-Castaneda, C., Di Pardo, A., Maglione, V., Caltagirone, C., et al. (2013). MRI measures of corpus callosum iron and myelin in early Huntington's disease. *Human Brain Mapping*, *35*(7), 3143–3151.

<http://doi.org/10.1002/hbm.22391>

Dumas, E. M., van den Bogaard, S. J. A., Ruber, M. E., Reilman, R. R., Stout, J. C., Craufurd, D., et al. (2012a). Early changes in white matter pathways of the sensorimotor cortex in premanifest Huntington's disease. *Human Brain Mapping*, *33*(1), 203–212. <http://doi.org/10.1002/hbm.21205>

Dumas, E. M., Versluis, M. J., van den Bogaard, S. J. A., van Osch, M. J. P., Hart, E. P., van Roon-Mom, W. M. C., et al. (2012b). Elevated brain iron is independent from atrophy in Huntington's Disease. *NeuroImage*, *61*(3), 558–564.

<http://doi.org/10.1016/j.neuroimage.2012.03.056>

Fennema-Notestine, C., Archibald, S. L., & Jacobson, M. W. (2004). In vivo evidence of cerebellar atrophy and cerebral white matter loss in Huntington disease. *Neurology*.

Han, I., You, Y., Kordower, J. H., Brady, S. T., & Morfini, G. A. (2010). Differential vulnerability of neurons in Huntington's disease: the role of cell type-specific features. *Journal of Neurochemistry*, *113*(5), 1073–1091.

<http://doi.org/10.1111/j.1471-4159.2010.06672.x>

MacDonald, M. E., Ambrose, C. M., Duyao, M. P., & Myers, R. H. (1993). A novel gene containing a trinucleotide repeat that is expanded and unstable on Huntington's

disease chromosomes. *Cell*, 72(6), 971–983. [http://doi.org/10.1016/0092-8674\(93\)90585-E](http://doi.org/10.1016/0092-8674(93)90585-E)

Myers, R. H., Vonsattel, J. P., Paskevich, P. A., Kiely, D. K., Stevens, T. J., Cupples, L. A., et al. (1991). Decreased neuronal and increased oligodendroglial densities in Huntington's disease caudate nucleus. *Journal of Neuropathology and Experimental Neurology*, 50(6), 729–742.

Nasir, J., Floresco, S. B., O'Kusky, J. R., Diewert, V. M., Richman, J. M., Zeisler, J., et al. (1995). Targeted disruption of the Huntington's disease gene results in embryonic lethality and behavioral and morphological changes in heterozygotes. *Cell*, 81(5), 811–823.

Rajkowska, G., Selemon, L. D., & Goldman-Rakic, P. S. (1998). Neuronal and glial somal size in the prefrontal cortex: a postmortem morphometric study of schizophrenia and Huntington disease. *Archives of General Psychiatry*, 55(3), 215–224.

Reiner, A., Albin, R. L., Anderson, K. D., D'Amato, C. J., Penney, J. B., & Young, A. B. (1988). Differential loss of striatal projection neurons in Huntington disease. *Proceedings of the National Academy of Sciences of the United States of America*, 85(15), 5733–5737.

Rosas, H. D., Lee, S. Y., Bender, A. C., Zaleta, A. K., Vangel, M., Yu, P., et al. (2010). Altered white matter microstructure in the corpus callosum in Huntington's disease: Implications for cortical 'disconnection'. *NeuroImage*, 49(4), 2995–3004.

<http://doi.org/10.1016/j.neuroimage.2009.10.015>

Rosas, H. D., Liu, A. K., Hersch, S., Glessner, M., Ferrante, R. J., Salat, D. H., et al. (2002). Regional and progressive thinning of the cortical ribbon in Huntington's disease. *Neurology*, *58*(5), 695–701. <http://doi.org/10.1212/WNL.58.5.695>

Sánchez-Castañeda, C., Squitieri, F., Di Paola, M., Dayan, M., Petrollini, M., & Sabatini, U. (2014). The role of iron in gray matter degeneration in Huntington's disease: A magnetic resonance imaging study. *Human Brain Mapping*, *36*(1), 50–66.

<http://doi.org/10.1002/hbm.22612>

Tabrizi, S. J., Langbehn, D. R., Leavitt, B. R., & Roos, R. (2009). Biological and clinical manifestations of Huntington's disease in the longitudinal TRACK-HD study: cross-sectional analysis of baseline data. *The Lancet*. [http://doi.org/10.1016/S1474-4422\(09\)70170-X](http://doi.org/10.1016/S1474-4422(09)70170-X)

Vonsattel, J. P., Myers, R. H., Stevens, T. J., Ferrante, R. J., Bird, E. D., & Richardson, E. P. (1985). Neuropathological classification of Huntington's disease. *Journal of Neuropathology and Experimental Neurology*, *44*(6), 559–577.

White, J. K., Auerbach, W., Duyao, M. P., Vonsattel, J. P., Gusella, J. F., Joyner, A. L., & MacDonald, M. E. (1997). Huntingtin is required for neurogenesis and is not impaired by the Huntington's disease CAG expansion. *Nature Genetics*, *17*(4), 404–410. <http://doi.org/10.1038/ng1297-404>

The material presented in this chapter is a representation of the following publication with permission to reprint.

Rowley CD, Tabrizi SJ, Scahill RI, Leavitt BR, Roos RA, Durr A, Bock NA (2018)
Altered Intracortical T₁-weighted/T₂-weighted ratio signal in Huntington's Disease.
Frontiers in Neuroscience. Submitted.

The only changes made were for thesis formatting and continuity purposes and copy editing.

Author List Contributions:

CD Rowley conducted image processing and analysis, and wrote manuscript.

SJ Tabrizi conducted original TRACK-HD study from which data was obtained

RI Scahill conducted original TRACK-HD study from which data was obtained

BR Leavitt conducted original TRACK-HD study from which data was obtained

RA Roos conducted original TRACK-HD study from which data was obtained

A Durr conducted original TRACK-HD study from which data was obtained

NA Bock contributed to study design and writing of the manuscript

Altered Intracortical T₁-weighted/T₂-weighted ratio signal in Huntington's Disease

Authors: Christopher D Rowley¹, Sarah J Tabrizi², Rachael I Scahill², Blair R Leavitt³,
Raymund A C Roos⁴, Alexandra Durr⁵, Nicholas A Bock⁶

¹McMaster Integrative Neuroscience Discovery and Study Program, McMaster
University, Canada, L8S 4K1

²Huntington's Disease Centre, University College London Institute of Neurology,
National Hospital for Neurology and Neurosurgery, London, UK, WC1N 3BG

³Department of Medical Genetics, University of British Columbia, Vancouver, British
Columbia, Canada, V6T 1Z4

⁴Department of Neurology, Leiden University Medical Centre, Leiden, The Netherlands

⁵ICM - Institut du Cerveau et de la Moelle Epinière, INSERM U1127, CNRS UMR7225,
Sorbonne Universités – UPMC Université Paris VI UMR_S1127 and APHP, Genetic
department, Pitié-Salpêtrière University Hospital, Paris, France

⁶Department of Psychology, Neuroscience & Behaviour, McMaster University,
Hamilton, Ontario, Canada, L8S 4K1

Keywords: Huntington's Disease, MRI, Cerebral Cortex, Myelin

Declaration of Interest: none

Abbreviations:

ACC – anterior cingulate cortex

CSF – cerebral spinal fluid

GM – grey matter

HD – Huntington’s Disease

HTT – huntingtin

MRI – magnetic resonance imaging

ROI – region of interest

T₁W – T₁-weighted

T₂W – T₂-weighted

WM – white matter

Acknowledgements:

We thank the TRACK-HD investigators, study participants and their families.

Funding Sources:

TRACK-HD was supported by the CHDI Foundation, a not-for-profit organization dedicated to finding treatments for Huntington's disease.

Abstract:

Huntington's disease (HD) is a genetic neurodegenerative disorder that is characterized by neuronal cell death. Although medium spiny neurons in the striatum are predominantly affected, other brain regions including the cerebral cortex also degenerate. Previous imaging studies have reported decreases in cortical thickness in HD, which could indicate changes in a broad number of microstructural features of the cerebral cortex. To more specifically investigate changes in cortical tissue composition in Huntington's, we analyzed intracortical T_1 -weighted/ T_2 -weighted magnetic resonance images (MRIs) collected in a cohort of 321 subjects from the TRACK-HD dataset representing various stages of HD and healthy controls. Significant T_1 -weighted/ T_2 -weighted signal increases were found in the most advanced HD group studied and were located in the pars opercularis, pars triangularis, superior temporal gyrus, medial temporal gyral pole, and cuneus. This may reflect disease-related increases in myelin and/or iron in the cortex or a change in the underlying cytoarchitecture.

4.1 Introduction

Huntington's disease (HD) is an autosomal dominant neurodegenerative disorder that is caused by a CAG repeat expansion in the huntingtin (*HTT*) gene (MacDonald, Ambrose, Duyao, & Myers, 1993). This repeat expansion leads to disrupted signaling in cortico-striatal circuits, followed by a loss of projection neurons in the striatum (Rangel-Barajas & Rebec, 2016). The neuronal loss and disrupted communication within the brain lead to the characteristic traits of the disease: progressive motor dysfunction, cognitive

decline, and behavioural deterioration (Walker, 2007),(Ross & Tabrizi, 2011). Given that symptomology extends beyond basic motor dysfunction into mood and cognition, the cerebral cortex may be implicated in the pathology of HD. In fact, postmortem studies have suggested that neuronal losses are prevalent in the cortex (Hedreen, Peyser, Folstein, & Ross, 1991; Kim et al., 2014; Mehrabi et al., 2016; Selemon, Rajkowska, & Goldman-Rakic, 2003) which warrants *in vivo* investigations in patients.

Since HD is progressive, *in vivo* imaging methods are invaluable for identifying disturbances in brain structure or function over the course of the disease. Magnetic resonance imaging (MRI) specifically has shown alterations in the brains of HD patients. These findings have primarily been structural in nature, with decreases in volume reported in the striatum, thalamus, cortical grey matter (GM), and major subcortical white matter (WM) tracts (Aylward et al., 1998; Fennema-Notestine, Archibald, & Jacobson, 2004; Paulsen et al., 2010; Rosas et al., 2003; Stoffers et al., 2010; Tabrizi, Langbehn, Leavitt, & Roos, 2009; Tabrizi, Reilmann, Roos, & Durr, 2012; Tabrizi, Scahill, Durr, Roos, & Leavitt, 2011; Thieben, Duggins, Good, & Gomes, 2002). Cortical thickness studies have further revealed a widespread thinning of the cortex that progresses as the disease advances (Rosas et al., 2002; 2008; Tabrizi et al., 2009). In terms of cerebral tissue composition, MRI has revealed increases in iron levels in the striatum in HD (Bartzokis, Cummings, Perlman, Hance, & Mintz, 1999; Bartzokis et al., 2007) and most recently, diffusion MRI and quantitative magnetization imaging have suggested a breakdown of myelin in deep WM tracts in HD (Bourbon-Teles et al., 2017).

While the cortical thickness studies suggest cortical involvement in HD, cortical thickness is a surrogate measure of cortical pathology that is sensitive to a broad range of microstructural features including angiogenesis, dendritic branching, axonal sprouting, myelin remodeling, and changes in neuronal and glial counts and sizes (Zatorre, Fields, & Johansen-Berg, 2012). The aim of this study is to investigate HD progression in the cerebral cortex using intracortical T_1 -weighted (T_1W) and T_2 -weighted (T_2W) MR signal intensity as a potential marker of changes in cortical tissue composition. In the brain, T_1 (Stüber et al., 2014) and T_2 (Desmond et al., 2016) are sensitive to myelin and iron amounts and can be used to measure tissue water content (Neeb, Zilles, & Shah, 2006). This study utilizes previously collected MRIs from the cross-sectional TRACK-HD study (Tabrizi et al., 2009), which contains a large number of well-described subjects that were imaged at high resolution with multiple MR contrasts including the requisite T_1W and T_2W for our analysis. The dataset represents disease stages across HD, starting before disease onset to well after the disease has progressed, which permits the investigation of cortical changes with HD advancement. The neuroimaging portion of the TRACK-HD study (Tabrizi et al., 2009) previously revealed changes in HD brains including cortical thickness decreases in occipital, temporal and parietal lobes, in addition to decreases in overall brain volume with increased disease burden score.

One challenge in analyzing MRIs from studies such as the TRACK-HD that collect data over multiple clinical sites is that variations in the different MRI systems used can introduce biases in the amplitude of MRI signals across the brain. These biases can obscure the subtle changes in intracortical contrast related to disease. A proposed solution to this problem is to form a ratio of T_1W and T_2W images that has a reduced sensitivity to bias (Glasser & Van Essen, 2011). These ratio maps have also been suggested to map myelin across the cortex (Glasser & Van Essen, 2011), although they might not be entirely specific to myelin (Arshad, Stanley, & Raz, 2017), especially in the presence of iron or cellular density changes that may be present in HD. In this study, we are thus investigating the T_1W/T_2W ratio image as a general marker of cortical composition changes in HD. To evaluate intracortical changes with disease progression, we measured the T_1W/T_2W ratio signal intensity in 82 regions at a middle depth in the cortex across four stages of HD and in healthy controls. We further investigated the T_1W and T_2W contrasts separately to see if either proved particularly sensitive to HD pathology.

4.2 Methods

TRACK-HD imaging and participant recruitment information has been detailed previously (Tabrizi et al., 2009). The main points are summarized below.

4.2.1: Participants

366 subjects were recruited from four imaging centers (London, UK; Paris, France; Leiden, Netherlands and Vancouver, Canada). Each center aimed to recruit a sample of 90 subjects with the following composition: 30 controls, 30 participants with

premanifest HD, and 30 participants with early HD. There were 366 images made available to us, with the following distribution: 123 controls, 120 premanifest HD, and 123 early HD.

Premanifest subjects were excluded with a burden of pathology score lower than 250, and had a total motor score below 5 using the motor assessment of the United Huntington's Disease Rating Scale (UHDRS). Healthy control subjects were age- and gender-matched to the combined HD and preHD group. To help control for environmental factors, controls were chosen from spouses or partners of preHD subjects, or were gene-negative siblings. This strict selection criterion aids in associating reported changes with HD.

HD participants were further subdivided for analysis. Premanifest HD subjects were split based on the median time for the predicted years to diagnosis (Langbehn et al., 2004) into those far from onset (PreHD-A) and closer to onset (PreHD-B). Early HD subjects were split based on their score on a total functional capacity scale (TFC) (Shoulson & Fahn, 1979) into Stage 1 (HD1, TFC 11-13) and Stage 2 (HD2, TFC 7-10).

In total 45 subjects had data that was not technically suitable for analysis: 19 subjects were excluded in primary stages of processing due to inadequate intrasubject image registration and 26 subjects were excluded in the analysis due to low signal-to-noise ratios in the MRIs. The remaining 321 subjects used in the study are summarized in Table 4.1.

	Controls (n=109)	PreHD			HD		
		PreHD- A (n=53)	PreHD- B (n=51)	Total (n=104)	HD Stage 1 (n=68)	HD Stage 2 (n=40)	Total (n=108)
Age (years)	46.1 (10.5)	40.6 (8.7)	39.6 (8.8)	40.1 (8.9)	47.1 (10.2)	51.1 (8.6)	48.6 (9.8)
Women	59 (54%)	29 (55%)	29 (57%)	58 (56%)	40 (59%)	18 (45%)	58 (54%)
Disease- Burden score	N/A	259.4 (29.0)	335.4 (30.2)	296.6 (48.2)	357.8 (74.5)	398.0 (70.4)	372.7 (75.3)
Centres							
Leiden	22	13	11	24	15	11	26
London	29	14	16	30	19	11	30
Paris	29	13	15	28	23	4	27
Vancouver	29	13	8	21	11	14	25

Table 4.1: Demographics for the participants used from the baseline TRACK-HD

dataset. Disease-burden score = Age \times (CAG length – 35.5). Data values are mean (SD), or number (%).

4.2.2: Imaging

All images were collected on 3T whole body scanners from two vendors (Siemens [S]: Paris and London, Phillips [P]: Leiden and Vancouver). T₁W images were collected using a 3D MPRAGE acquisition with the following parameters: TR = 2200ms [S]/ 7.7ms [P], TE = 2.2ms [S]/ 3.5ms [P], TI = 900ms [S] /950ms [P], FA= 10° [S]/ 8° [P],

FOV = 28cm [S]/ 24cm [P], matrix size 256x256 [S]/ 224x224 [P], 208 [S]/ 164[P] sagittal slices with 1mm thickness to cover the entire brain. T₂W images were acquired (SPACE sequence on Siemens scanners, VISTA on Phillips scanners) with identical field of view, acquisition matrix, slice thickness and the following timing parameters: TR = 3000ms, TE = 421ms.

4.2.3: Processing

The aim of the image processing was to accurately segment GM and WM tissue classes in each subject's T₁W MRI and construct a middle-depth surface through the cortex for visualizing intracortical MRI signals. The middle depth surface of each subject was registered to a template to allow for group comparisons using a region-of-interest (ROI) analysis.

The software used for image processing was: Matlab (vR2015a, <https://www.mathworks.com>), Elastix (Klein, Staring, Murphy, Viergever, & Pluim, 2010; Shamonin, Bron, & Lelieveldt, 2013), ITK-SNAP (version 3.4, <http://www.itksnap.org/>) (Yushkevich et al., 2006), MIPAV v7.4 software (mipav.cit.nih.gov) using the JIST v3.0 (www.nitrc.org/projects/jist/), TOADS-CRUISE vR3c (www.nitrc.org/projects/toads-cruise), and CBS High-Res Brain Processing Tools Version v3.0 (www.nitrc.org/projects/cbs-tools) plug-ins.

First, images were rigidly registered to begin the cortical segmentation. Each subject's T₂W image was rigidly registered to that subject's T₁W image using Elastix. The T₁W image was rigidly registered to the 1mm MNI-152 template, and then the 6-

parameter affine transform was applied to the T_2W image such that both images were co-registered in MNI-152 space.

Tissue segmentation was performed using custom scripts in Matlab. First a custom written algorithm was applied to perform local intensity normalization to the T_1W image to aid in segmentation of the pial surface where cortical signal is artificially reduced in some images due to bias in radiofrequency transmit and receive fields (B_1+ and B_1-). Briefly, a new image was created by sliding a $3 \times 3 \times 3$ window across the original T_1W image, with the center voxel location in the new image taking on the greatest intensity value in the original image. This image was smoothed using a 10mm 3D Gaussian kernel creating an intensity field map. The original T_1W image was divided by this new image, creating an image where intensity is normalized by nearby voxels. This image was used solely for image segmentation and not for subsequent MRI signal analysis, since meaningful changes in intracortical signal are also potentially normalized.

Next the MNI-152 template was registered to the subject using a b-spline transform, and the transformation was applied to a smoothed brain mask that had been created in MNI-152 space. The transformed binary mask was multiplied with the normalized T_1W image to skull strip the image. The resolution in the masked normalized image was doubled in all dimensions, and then the image was sharpened to further increase the intensity gradient at the pial surface. An intensity threshold was applied to the skull stripped image that was derived using an intensity histogram to calculate the threshold to remove CSF. A morphological algorithm to remove small objects was applied to remove dura mater. The new cerebrum mask was first eroded, then dilated to

further remove dura mater. Following this, the cerebrum mask was down sampled back to the original image dimensions. One final threshold operation was applied to remove CSF that may have been added in during the dilation operation. This threshold intensity value was the same as was calculated earlier using the intensity histogram. All segmentations were manually inspected and corrected to remove any remaining dura mater or cerebellum using ITK-SNAP. Each subject's group was blinded to the investigator until after the completion of all image processing.

The cerebrum segmentation was used to mask the locally normalized T_1W created earlier. The masked image was used as the input to the FANTASM algorithm (Pham, 2001) in MIPAV, which segmented the image into two tissue classes: WM and GM. Following segmentation, labels for each tissue class were split back into left and right hemispheres for subsequent processing. A volume-preserving cortical depth model was used to generate the middle depth intracortical surface (Waehnert et al., 2014). Each subject's surface was registered to the middle depth surface generated from the MNI-152 atlas using a multi-scale surface registration approach (Tardif et al., 2015). Each hemisphere was registered separately to improve speed and accuracy. Surfaces labeled with the T_1W , T_2W , and T_1W/T_2W ratio intensity were created using CBS-Tools.

4.2.4: Statistics

Cortical maps were generated using Surfstat (<http://www.math.mcgill.ca/keith/surfstat/>) in Matlab, where signal intensity values were smoothed along the surface using a 6mm Gaussian kernel. The MarsAtlas (Auzias,

Coulon, & Brovelli, 2016) was used to parcellate the cortex into 82 regions-of-interest (ROIs) for analysis with statistical analysis completed using R (<https://www.r-project.org>).

Signal intensity as a function of age was investigated for each ROI. Since *ncvTest* in R reported non-equal error variance in the linear model, weighted regression was instead used for the analysis. The weight used was $1/\text{standard deviation of the signal intensity}$ for each ROI, which in effect applies a lower weighting to images with more artifacts such as noise. The regression equation took the form: $Signal \sim Age + Study_site + Disease_group$, where *Study_site* was a factor with four levels corresponding to the location where the scans were taken. This was used to account for differences in bias fields and imaging methods at each site, validated by a lower Akaike criterion compared to using the scanner manufacturer.

Corrections for type-I errors were performed using the Holm-Bonferonni method (Ludbrook, 1998) on the resulting p-values calculated for each *Disease_group*, accounting for 82 ROIs. An exploratory analysis without correction was conducted using the raw T_1W and T_2W images to see whether one contrast, or both, were more sensitive to changes in HD.

4.3 Results

4.3.1 T_1W/T_2W Ratio Image Signal

Group differences based on the T_1W/T_2W ratio image intensity are presented in Figure 4.1. The regression coefficients are visualized for each group to illustrate the

difference relative to the control population. This value represents the difference in ratio signal that would exist with the other regression variables held equal between a subject in each group. The disease coefficients were similar for groups preHD-A, preHD-B, and HD Stage 1, with no regions in these groups being statistically significant relative to controls. Though insignificant, there were both increases and decreases in T_1W/T_2W ratio across regions and stages. Significant regions were found in the HD Stage 2 group relative to controls, and are shown at the bottom of Figure 4.1. The ratio signal increased in a similar pattern bilaterally within the following significant regions: pars opercularis, pars triangularis, superior temporal gyrus, medial temporal gyral pole, and cuneus.

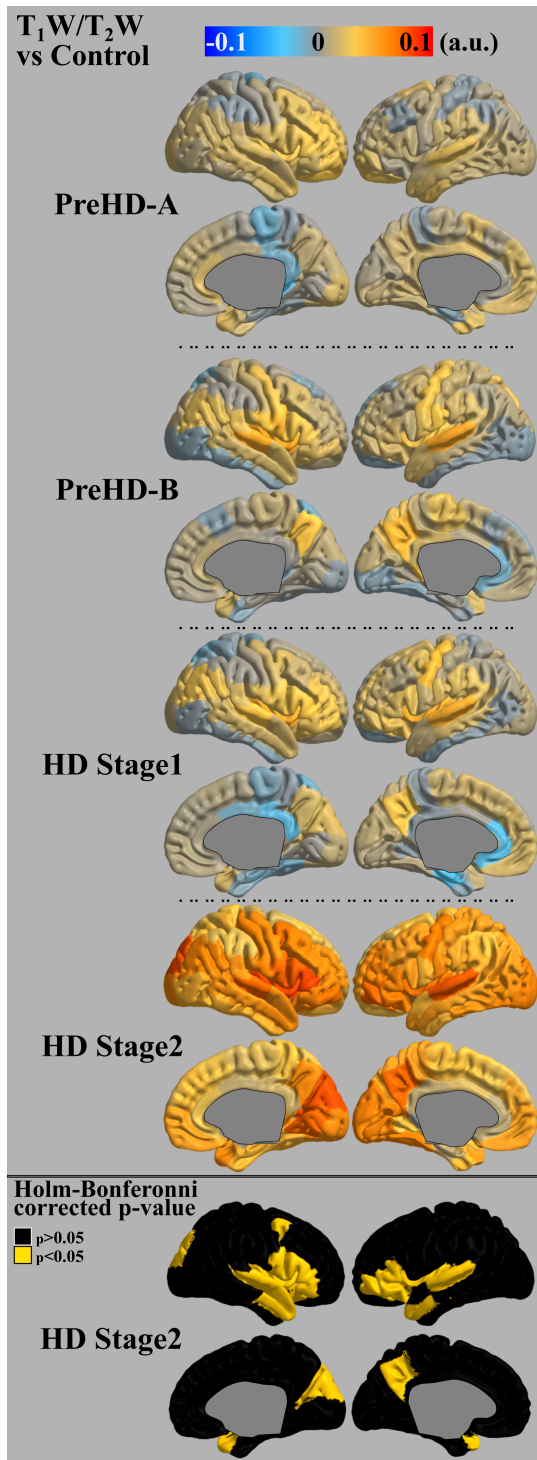


Figure 4.1: T₁W/T₂W ratio changes in HD. Coefficients from the intracortical signal analysis are mapped onto the cortex, illustrating the difference in ratio signal relative to

controls with other regressors being held equal. Significant changes are seen only in the Stage 2 HD group (highlighted in the bottom panel).

4.3.2 Separate analysis of T₁W and T₂W Signal

To investigate which signal contrast contributes most to the changes seen in HD Stage 2 in this study, we performed the same weighted-regression analysis on both T₁W and T₂W as for the ratio images. No ROIs in either the T₁W or T₂W analysis were significant following the Bonferonni-Holm correction, so as an exploratory analysis we examined the uncorrected p-values. The uncorrected p-values for this analysis are mapped to the cortical surface in Figure 4.2. No significant changes were seen between groups in the T₁W images. Regions were found to be significant ($p < 0.05$ uncorrected) in the T₂W images in similar locations where the ratio image had shown significant changes in this group. A decrease in T₂W intensity thus appears to be the driving factor for the increase in the T₁W/T₂W ratio signal. The T₁W/T₂W ratio signal however, shows better sensitivity than the T₂W signal for detecting changes related to Stage 2 HD, likely due to the partial bias field cancellation in the ratio image.

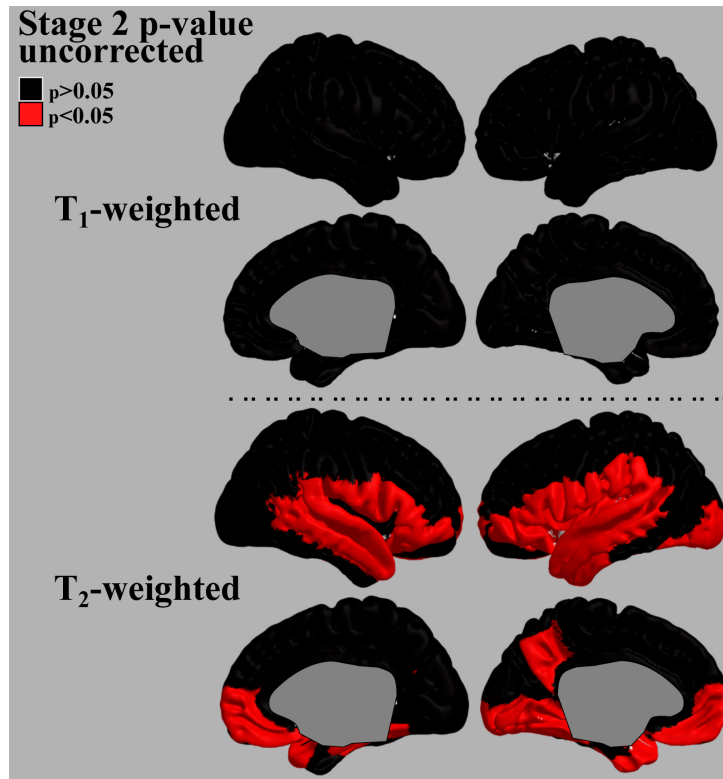


Figure 4.2: Separate analysis of T₁W and T₂W signal changes in HD Stage 2. Many of the same regions that were significant for T₁W/T₂W signal in HD Stage 2 relative to control show significant T₂W signal changes ($p < 0.05$ uncorrected).

4.4 Discussion

To look at the composition of cortical tissue in HD progression, we examined the intracortical MRI intensity values (Eickhoff et al., 2005). However, differences in radiofrequency coil geometries between different MRI vendors and sites can mean that T₁W and T₂W images have strong intensity bias fields that obscure signal changes in the cortex caused by pathology. Thus, we turned to using a ratio of T₁W/T₂W images to reduce these biases and increase sensitivity. Using this approach, we uncovered

significant differences in T_1W/T_2W intensity in the cortex in the most advanced HD group, suggesting alterations in the composition of the cerebral cortex in HD. A potential pitfall in using the ratio signal is that one cannot know whether T_1W , T_2W or both signals are changing, which complicates the interpretation of findings. To attempt to clarify this, we conducted a separate analysis of the T_1W and T_2W MRIs. We found that the T_1W/T_2W ratio image was more sensitive than either of the separate MRIs in detecting changes in HD since no changes in T_1W or T_2W intensity survived multiple comparison correction (Figure 4.2). This is likely because the ratio image has a reduced sensitivity to bias fields, such that separate investigations of T_1W and T_2W images in the future would benefit from bias correction using maps of B_1+ and B_1- fields in the MRI. Secondly, we found in our exploratory analysis of uncorrected p-values that between T_1W and T_2W signals, the T_2W signal was more sensitive to changes in HD. This should not be interpreted as saying that HD only affects T_2 , since the sensitivity of a T_1W or T_2W image is highly dependent on the MRI acquisition sequence and its parameters. The T_1 sequence used in the TRACK-HD study was selected to optimize sensitivity to grey/white matter contrast around the subcortical structures and therefore may not have been as sensitive to cortical pathology as other acquisitions. For instance, we found that the T_1W signal had little correlation with age, but this relationship has been shown to exist in other studies (Rowley et al., 2017; Salat et al., 2009; Vidal-Piñeiro et al., 2016; Westlye et al., 2010). Conversely, the T_2W and ratio signal in this study displayed a correlation with age, and this was expected based on previous reports (Shafee, Buckner, & Fischl, 2015; Westlye et al., 2010). This suggests that the T_2W images had a greater sensitivity to intracortical contrast than the

T₁W images in this cohort, and that changes in T₂W signal were driving the changes seen in the ratio images.

The decrease in the T₂W signal in Stage 2 HD could be reflecting increases in myelin and/or iron amounts, as both of these are prominent features of cortical composition that affect the MR signal (Fukunaga et al., 2010) and have been shown to strongly affect the T₂W signal (Desmond et al., 2016; Fukunaga et al., 2010). An increase in myelin could be the result of overall increases in oligodendrocytes, or an increased density of myelin due to neuronal loss and/or shrinkage. Oligodendrocyte densities are known to double in presymptomatic HD carriers in the tail of the caudate nucleus, while other cell densities are unchanged (Gómez-Tortosa et al., 2001). Neuronal densities have been shown to decrease while oligodendrocyte density increases after HD onset in the caudate (Myers et al., 1991). While this finding is in subcortical GM, increased glial density been reported in the GM of the cortex with HD onset as well (Passani, Vonsattel, Carter, & Coyle, 1997; Rajkowska, Selemon, & Goldman-Rakic, 1998; Selemon et al., 2003). The decrease in T₂W signal could also be reporting increased levels of cortical iron. It has previously been reported that ferritin iron increases in subcortical GM in HD (Bartzokis et al., 1999; 2007), and found only after HD onset (Dumas et al., 2012). Ferritin has a strong effect on decreasing T₂W signal, but only a weak effect on increasing T₁W signal (Vymazal et al., 1995). An increase in cortical ferritin levels would support our findings of decreased T₂W signal, and an increase in the subsequent ratio image. While there are conflicting MRI reports of cortical iron accumulation (Rosas et al., 2012) and iron decreases (Sánchez-Castañeda et al., 2014), both studies agree that iron

concentrations become further altered the longer the disease progresses. As histology work has reported increases in glia in both subcortical GM and cortical GM, it is likely that the increase in subcortical iron levels could be present in the cortex as well. Disentangling iron and myelin contributions to signal can be difficult, since oligodendrocytes are iron enriched cells (Todorich, Pasquini, Garcia, Paez, & Connor, 2009), and combined MRI and histology work has shown that there is considerable overlap in iron and myelin distributions in the cortex (Stüber et al., 2014). However, it has been shown that in later stages of HD, ferritin accumulates in the microglia of both the cortex and the striatum, not in oligodendrocytes (Simmons et al., 2007). Thus this change in T_2W signal could be separate from changes in myelin, and be reporting increased ferritin levels in cortical microglia.

Finally, the lower T_2W signal could be due to changes in cytoarchitecture of the cortex, such that there is less bulk water content per imaging voxel. Histological studies have shown that neuronal densities decrease in HD (Passani et al., 1997; Rajkowska et al., 1998; Selemon et al., 2003). This decrease in neuronal and increase in glial density could therefore decrease MR visible water as it has been highlighted in the mammalian central nervous system that neurons have a higher water percentage than glial cells (LoPachin, Castiglia, & Saubermann, 1991). However, Eickhoff et al., previously reported that myelin content dominates the cortical signal over the underlying cytoarchitecture (Eickhoff et al., 2005), such that it is unlikely that our change in signal in HD is due to changes in cytoarchitecture. To obtain a better understanding regarding the underlying pathology using neuroimaging, more specific MRI contrasts should be used, such as

magnetization transfer for investigating myelin (Helms, Dathe, Kallenberg, & Dechent, 2008), quantitative susceptibility mapping for iron (Langkammer et al., 2010) and diffusion imaging for exploring neurite density (Calamante, Jeurissen, Smith, Tournier, & Connelly, 2017).

4.5 Conclusions

In this study, intracortical T_1W/T_2W analysis revealed a significant change in the most advanced HD group, which could reflect an increase in iron and/or myelin, or a decrease in MR visible water resulting from changes in cytoarchitecture in the cortex. Our analysis revealed that each individual scanner should be taken into account for signal analysis. This is likely due to inter-site differences in radiofrequency field inhomogeneities (B_1+ and B_1-), which cannot be accurately corrected during post-hoc analysis without B_1 maps. It would be worthwhile to revisit this study with targeted imaging for intracortical contrast, with MRI protocols that account for intensity biases between imaging sites. With increased cortical contrast and bias correction, intracortical MR signal mapping may better track HD through disease stages, and have the potential to be used as a biomarker to mark disease progression in clinical trials. It would also be useful to explore cortical pathology in HD using MRI methods that are most specific for features of cortical tissue composition.

References

- Arshad, M., Stanley, J. A., & Raz, N. (2017). Test-retest reliability and concurrent validity of in vivo myelin content indices: Myelin water fraction and calibrated T1 w/T2 w image ratio. *Human Brain Mapping, 38*(4), 1780–1790.
<http://doi.org/10.1002/hbm.23481>
- Auzias, G., Coulon, O., & Brovelli, A. (2016). MarsAtlas: A cortical parcellation atlas for functional mapping. *Human Brain Mapping, 37*(4), 1573–1592.
<http://doi.org/10.1002/hbm.23121>
- Aylward, E. H., Anderson, N. B., Bylsma, F. W., Wagster, M. V., Barta, P. E., Sherr, M., et al. (1998). Frontal lobe volume in patients with Huntington's disease. *Neurology, 50*(1), 252–258.
- Bartzokis, G., Cummings, J., Perlman, S., Hance, D. B., & Mintz, J. (1999). Increased basal ganglia iron levels in Huntington disease. *Archives of Neurology, 56*(5), 569–574.
- Bartzokis, G., Lu, P. H., Tishler, T. A., Fong, S. M., Oluwadara, B., Finn, J. P., et al. (2007). Myelin Breakdown and Iron Changes in Huntington's Disease: Pathogenesis and Treatment Implications. *Neurochemical Research, 32*(10), 1655–1664.
<http://doi.org/10.1007/s11064-007-9352-7>
- Bourbon-Teles, J., Bells, S., Jones, D. K., Coulthard, E., Rosser, A., & Metzler-Baddeley, C. (2017). Myelin breakdown in human Huntington's disease: Multi-modal evidence from diffusion MRI and quantitative magnetization transfer. *Neuroscience*.

<http://doi.org/10.1016/j.neuroscience.2017.05.042>

- Calamante, F., Jeurissen, B., Smith, R. E., Tournier, J.-D., & Connelly, A. (2017). The role of whole-brain diffusion MRI as a tool for studying human in vivo cortical segregation based on a measure of neurite density. *Magnetic Resonance in Medicine*, 218(Pt 2), 303–7. <http://doi.org/10.1002/mrm.26917>
- Desmond, K. L., Al-Ebraheem, A., Janik, R., Oakden, W., Kwiecien, J. M., Dabrowski, W., et al. (2016). Differences in iron and manganese concentration may confound the measurement of myelin from R1 and R2 relaxation rates in studies of dysmyelination. *NMR in Biomedicine*, 29(7), 985–998. <http://doi.org/10.1002/nbm.3549>
- Dumas, E. M., Versluis, M. J., van den Bogaard, S. J. A., van Osch, M. J. P., Hart, E. P., van Roon-Mom, W. M. C., et al. (2012). Elevated brain iron is independent from atrophy in Huntington's Disease. *NeuroImage*, 61(3), 558–564. <http://doi.org/10.1016/j.neuroimage.2012.03.056>
- Eickhoff, S., Walters, N. B., Schleicher, A., Kril, J., Egan, G. F., Zilles, K., et al. (2005). High-resolution MRI reflects myeloarchitecture and cytoarchitecture of human cerebral cortex. *Human Brain Mapping*, 24(3), 206–215. <http://doi.org/10.1002/hbm.20082>
- Fennema-Notestine, C., Archibald, S. L., & Jacobson, M. W. (2004). In vivo evidence of cerebellar atrophy and cerebral white matter loss in Huntington disease. *Neurology*.
- Fukunaga, M., Li, T. Q., van Gelderen, P., de Zwart, J. A., Shmueli, K., Yao, B., et al. (2010). Layer-specific variation of iron content in cerebral cortex as a source of MRI

contrast. *Proceedings of the National Academy of Sciences of the United States of America*, *107*(8), 3834–3839. <http://doi.org/10.1073/pnas.0911177107>

Glasser, M. F., & Van Essen, D. C. (2011). Mapping Human Cortical Areas In Vivo Based on Myelin Content as Revealed by T1- and T2-Weighted MRI. *Journal of Neuroscience*, *31*(32), 11597–11616. <http://doi.org/10.1523/JNEUROSCI.2180-11.2011>

Gómez-Tortosa, E., MacDonald, M. E., Friend, J. C., Taylor, S. A., Weiler, L. J., Cupples, L. A., et al. (2001). Quantitative neuropathological changes in presymptomatic Huntington's disease. *Annals of Neurology*, *49*(1), 29–34.

Hedreen, J. C., Peyser, C. E., Folstein, S. E., & Ross, C. A. (1991). Neuronal loss in layers V and VI of cerebral cortex in Huntington's disease. *Neuroscience Letters*, *133*(2), 257–261.

Helms, G., Dathe, H., Kallenberg, K., & Dechent, P. (2008). High-resolution maps of magnetization transfer with inherent correction for RF inhomogeneity and T1 relaxation obtained from 3D FLASH MRI. *Magnetic Resonance in Medicine*, *60*(6), 1396–1407. <http://doi.org/10.1002/mrm.21732>

Kim, E. H., Thu, D. C. V., Tippett, L. J., Oorschot, D. E., Hogg, V. M., Roxburgh, R., et al. (2014). Cortical interneuron loss and symptom heterogeneity in Huntington disease. *Annals of Neurology*, *75*(5), 717–727. <http://doi.org/10.1002/ana.24162>

Klein, S., Staring, M., Murphy, K., Viergever, M. A., & Pluim, J. P. W. (2010). elastix: a toolbox for intensity-based medical image registration. *IEEE Transactions on*

Medical Imaging, 29(1), 196–205. <http://doi.org/10.1109/TMI.2009.2035616>

Langbehn, D. R., Brinkman, R. R., Falush, D., Paulsen, J. S., Hayden, M. R., on behalf of an International Huntington's Disease Collaborative Group. (2004). A new model for prediction of the age of onset and penetrance for Huntington's disease based on CAG length. *Clinical Genetics*, 65(4), 267–277. <http://doi.org/10.1111/j.1399-0004.2004.00241.x>

Langkammer, C., Krebs, N., Goessler, W., Scheurer, E., Ebner, F., Yen, K., et al. (2010). Quantitative MR Imaging of Brain Iron: A Postmortem Validation Study. *Radiology*, 257(2), 455–462. <http://doi.org/10.1148/radiol.10100495>

LoPachin, R. M., Castiglia, C. M., & Saubermann, A. J. (1991). Elemental composition and water content of myelinated axons and glial cells in rat central nervous system. *Brain Research*, 549(2), 253–259.

Ludbrook, J. (1998). Multiple comparison procedures updated. *Clinical and Experimental Pharmacology & Physiology*, 25(12), 1032–1037.

MacDonald, M. E., Ambrose, C. M., Duyao, M. P., & Myers, R. H. (1993). A novel gene containing a trinucleotide repeat that is expanded and unstable on Huntington's disease chromosomes. *Cell*, 72(6), 971–983. [http://doi.org/10.1016/0092-8674\(93\)90585-E](http://doi.org/10.1016/0092-8674(93)90585-E)

Mehrabi, N. F., Waldvogel, H. J., Tippett, L. J., Hogg, V. M., Synek, B. J., & Faull, R. L. M. (2016). Symptom heterogeneity in Huntington's disease correlates with neuronal degeneration in the cerebral cortex. *Neurobiology of Disease*, 96, 67–74.

<http://doi.org/10.1016/j.nbd.2016.08.015>

Myers, R. H., Vonsattel, J. P., Paskevich, P. A., Kiely, D. K., Stevens, T. J., Cupples, L.

A., et al. (1991). Decreased neuronal and increased oligodendroglial densities in Huntington's disease caudate nucleus. *Journal of Neuropathology and Experimental Neurology*, 50(6), 729–742.

Neeb, H., Zilles, K., & Shah, N. J. (2006). Fully-automated detection of cerebral water

content changes: Study of age- and gender-related H₂O patterns with quantitative MRI. *NeuroImage*, 29(3), 910–922. <http://doi.org/10.1016/j.neuroimage.2005.08.062>

Passani, L. A., Vonsattel, J. P., Carter, R. E., & Coyle, J. T. (1997). N-

acetylaspartylglutamate, N-acetylaspartate, and N-acetylated alpha-linked acidic dipeptidase in human brain and their alterations in Huntington and Alzheimer's diseases. *Molecular and Chemical Neuropathology*, 31(2), 97–118.

Paulsen, J. S., Nopoulos, P. C., Aylward, E., Ross, C. A., Johnson, H., Magnotta, V. A.,

et al. (2010). Striatal and white matter predictors of estimated diagnosis for Huntington disease. *Brain Research Bulletin*, 82(3-4), 201–207.

<http://doi.org/10.1016/j.brainresbull.2010.04.003>

Pham, D. L. (2001). Robust fuzzy segmentation of magnetic resonance images.

Computer-Based Medical Systems.

Rajkowska, G., Selemon, L. D., & Goldman-Rakic, P. S. (1998). Neuronal and glial

somal size in the prefrontal cortex: a postmortem morphometric study of schizophrenia and Huntington disease. *Archives of General Psychiatry*, 55(3), 215–

224.

Rangel-Barajas, C., & Rebec, G. V. (2016). Dysregulation of Corticostriatal Connectivity in Huntington's Disease: A Role for Dopamine Modulation. *Journal of Huntington's Disease*, 5(4), 303–331. <http://doi.org/10.3233/JHD-160221>

Rosas, H. D., Chen, Y. I., Doros, G., Salat, D. H., Chen, N.-K., Kwong, K. K., et al. (2012). Alterations in brain transition metals in Huntington disease: an evolving and intricate story. *Archives of Neurology*, 69(7), 887–893. <http://doi.org/10.1001/archneurol.2011.2945>

Rosas, H. D., Koroshetz, W. J., Chen, Y. I., Skeuse, C., Vangel, M., Cudkowicz, M. E., et al. (2003). Evidence for more widespread cerebral pathology in early HD An MRI-based morphometric analysis. *Neurology*, 60(10), 1615–1620. <http://doi.org/10.1212/01.WNL.0000065888.88988.6E>

Rosas, H. D., Liu, A. K., Hersch, S., Glessner, M., Ferrante, R. J., Salat, D. H., et al. (2002). Regional and progressive thinning of the cortical ribbon in Huntington's disease. *Neurology*, 58(5), 695–701. <http://doi.org/10.1212/WNL.58.5.695>

Rosas, H. D., Salat, D. H., Lee, S. Y., Zaleta, A. K., Pappu, V., Fischl, B., et al. (2008). Cerebral cortex and the clinical expression of Huntington's disease: complexity and heterogeneity. *Brain*, 131(4), 1057–1068. <http://doi.org/10.1093/brain/awn025>

Ross, C. A., & Tabrizi, S. J. (2011). Huntington's disease: from molecular pathogenesis to clinical treatment. *The Lancet Neurology*. [http://doi.org/10.1016/S1474-4422\(10\)70245-3](http://doi.org/10.1016/S1474-4422(10)70245-3)

- Rowley, C. D., Sehmbi, M., Bazin, P.-L., Tardif, C. L., Minuzzi, L., Frey, B. N., & Bock, N. A. (2017). Age-related mapping of intracortical myelin from late adolescence to middle adulthood using T1-weighted MRI. *Human Brain Mapping, 37*, 1573–13. <http://doi.org/10.1002/hbm.23624>
- Salat, D. H., Lee, S. Y., van der Kouwe, A. J., Greve, D. N., Fischl, B., & Rosas, H. D. (2009). Age-associated alterations in cortical gray and white matter signal intensity and gray to white matter contrast. *NeuroImage, 48*(1), 21–28. <http://doi.org/10.1016/j.neuroimage.2009.06.074>
- Sánchez-Castañeda, C., Squitieri, F., Di Paola, M., Dayan, M., Petrollini, M., & Sabatini, U. (2014). The role of iron in gray matter degeneration in Huntington's disease: A magnetic resonance imaging study. *Human Brain Mapping, 36*(1), 50–66. <http://doi.org/10.1002/hbm.22612>
- Selemon, L. D., Rajkowska, G., & Goldman-Rakic, P. S. (2003). Evidence for progression in frontal cortical pathology in late-stage Huntington's disease. *The Journal of Comparative Neurology, 468*(2), 190–204. <http://doi.org/10.1002/cne.10938>
- Shafee, R., Buckner, R. L., & Fischl, B. (2015). Gray matter myelination of 1555 human brains using partial volume corrected MRI images. *NeuroImage, 105*(C), 473–485. <http://doi.org/10.1016/j.neuroimage.2014.10.054>
- Shamonin, D. P., Bron, E. E., & Lelieveldt, B. (2013). Fast parallel image registration on CPU and GPU for diagnostic classification of Alzheimer's disease. *Frontiers in ...*

<http://doi.org/10.3389/fninf.2013.00050/abstract>

Shoulson, I., & Fahn, S. (1979). Huntington disease: clinical care and evaluation.

Neurology, 29(1), 1–3.

Simmons, D. A., Casale, M., Alcon, B., Pham, N., Narayan, N., & Lynch, G. (2007).

Ferritin accumulation in dystrophic microglia is an early event in the development of Huntington's disease. *Glia*, 55(10), 1074–1084. <http://doi.org/10.1002/glia.20526>

Stoffers, D., Sheldon, S., Kuperman, J. M., Goldstein, J., Corey-Bloom, J., & Aron, A. R.

(2010). Contrasting gray and white matter changes in preclinical Huntington disease: An MRI study. *Neurology*, 74(15), 1208–1216.

<http://doi.org/10.1212/WNL.0b013e3181d8c20a>

Stüber, C., Morawski, M., Schäfer, A., Labadie, C., Wähnert, M., Leuze, C., et al. (2014).

Myelin and iron concentration in the human brain: A quantitative study of MRI contrast. *NeuroImage*, 93, 95–106. <http://doi.org/10.1016/j.neuroimage.2014.02.026>

Tabrizi, S. J., Langbehn, D. R., Leavitt, B. R., & Roos, R. (2009). Biological and clinical

manifestations of Huntington's disease in the longitudinal TRACK-HD study: cross-sectional analysis of baseline data. *The Lancet*. [http://doi.org/10.1016/S1474-](http://doi.org/10.1016/S1474-4422(09)70170-X)

[4422\(09\)70170-X](http://doi.org/10.1016/S1474-4422(09)70170-X)

Tabrizi, S. J., Reilmann, R., Roos, R., & Durr, A. (2012). Potential endpoints for clinical

trials in premanifest and early Huntington's disease in the TRACK-HD study:

analysis of 24 month observational data. *The Lancet*. [http://doi.org/10.1016/S1474-](http://doi.org/10.1016/S1474-4422(11)70263-0)

[4422\(11\)70263-0](http://doi.org/10.1016/S1474-4422(11)70263-0)

- Tabrizi, S. J., Scahill, R. I., Durr, A., Roos, R., & Leavitt, B. R. (2011). Biological and clinical changes in premanifest and early stage Huntington's disease in the TRACK-HD study: the 12-month longitudinal analysis. *The Lancet*.
[http://doi.org/10.1016/S1474-4422\(10\)70276-3](http://doi.org/10.1016/S1474-4422(10)70276-3)
- Tardif, C. L., Schäfer, A., Waehnert, M., Dinse, J., Turner, R., & Bazin, P.-L. (2015). Multi-contrast multi-scale surface registration for improved alignment of cortical areas. *NeuroImage*, *111*(C), 107–122.
<http://doi.org/10.1016/j.neuroimage.2015.02.005>
- Thieben, M. J., Duggins, A. J., Good, C. D., & Gomes, L. (2002). The distribution of structural neuropathology in pre-clinical Huntington's disease. *Brain*.
- Todorich, B., Pasquini, J. M., Garcia, C. I., Paez, P. M., & Connor, J. R. (2009). Oligodendrocytes and myelination: The role of iron. *Glia*, *57*(5), 467–478.
<http://doi.org/10.1002/glia.20784>
- Vidal-Piñeiro, D., Walhovd, K. B., Storsve, A. B., Grydeland, H., Rohani, D. A., & Fjell, A. M. (2016). Accelerated longitudinal gray/white matter contrast decline in aging in lightly myelinated cortical regions. *Human Brain Mapping*, 1–16.
<http://doi.org/10.1002/hbm.23267>
- Vymazal, J., Brooks, R. A., Patronas, N., Hajek, M., Bulte, J. W., & Di Chiro, G. (1995). Magnetic resonance imaging of brain iron in health and disease. *Journal of the Neurological Sciences*, *134 Suppl*, 19–26.
- Waehnert, M. D., Dinse, J., Weiss, M., Streicher, M. N., Waehnert, P., Geyer, S., et al.

- (2014). Anatomically motivated modeling of cortical laminae. *NeuroImage*, 93(P2), 210–220. <http://doi.org/10.1016/j.neuroimage.2013.03.078>
- Walker, F. O. (2007). Huntington's disease. *Lancet (London, England)*, 369(9557), 218–228. [http://doi.org/10.1016/S0140-6736\(07\)60111-1](http://doi.org/10.1016/S0140-6736(07)60111-1)
- Westlye, L. T., Walhovd, K. B., Dale, A. M., Bjørnerud, A., Due-Tønnessen, P., Engvig, A., et al. (2010). Differentiating maturational and aging-related changes of the cerebral cortex by use of thickness and signal intensity. *NeuroImage*, 52(1), 172–185. <http://doi.org/10.1016/j.neuroimage.2010.03.056>
- Yushkevich, P. A., Piven, J., Hazlett, H. C., Smith, R. G., Ho, S., Gee, J. C., & Gerig, G. (2006). User-guided 3D active contour segmentation of anatomical structures: Significantly improved efficiency and reliability. *NeuroImage*, 31(3), 1116–1128. <http://doi.org/10.1016/j.neuroimage.2006.01.015>
- Zatorre, R. J., Fields, R. D., & Johansen-Berg, H. (2012). Plasticity in gray and white: neuroimaging changes in brain structure during learning. *Nature Publishing Group*, 15(4), 528–536. <http://doi.org/10.1038/nn.3045>

Chapter 5: Future Directions and Conclusions

5.1 Conclusions

The first aim of this thesis was to extend a previous cortical analysis technique in MRI to include information about the underlying myeloarchitecture. It was found that T₁W imaging with high ICM contrast displayed two types of tissue classes in the cortex. It was possible to use a fuzzy clustering algorithm to label these two classes across the brain for subsequent thickness calculations. It is likely that a sufficient contrast-to-noise ratio is required for the algorithm to produce meaningful tissue classes. The usefulness of the technique was demonstrated in BD where a preferential loss of heavily myelinated layers was found in the dorsal lateral prefrontal cortex. This was an expected finding based on previous reports of decreased densities of oligodendrocytes in the cortex in BD (Rajkowska, Halaris, & Selemon, 2001; Uranova, Vostrikov, Orlovskaya, & Rachmanova, 2004) and has since led to other studies confirming reduced ICM in the disorder.

The second aim was to characterize intracortical myelin trajectories from young to middle adulthood. This study used same imaging with strong intracortical contrast to investigate age-related changes at three cortical depths and in the superficial white matter. It was found that for a cohort of healthy subjects representing young to middle adulthood, a quadratic fit best followed age trajectories in the cortex, while neither linear nor quadratic age predictors globally fit the SWM intensity. A quadratic model provides additional information to a linear fit, as it can reveal the peak of the trajectory. This was

exploited in the mapping of peak age to chart developmental trajectories. It was found that visual areas reached peak myelination first, while motor regions are the last to mature.

The final aim of this work was to test if ICM analysis could be extended to commonly acquired images from the clinic. T_1W and T_2W are commonly acquired anatomical scans, and exist in many databases from previous studies. Both images have myelin-related contrast, and the ratio of the two provides some B_1 inhomogeneity correction. This imaging method for myelin mapping was explored in HD, where known increases in oligodendrocyte densities are found. A novel segmentation method was developed to acquire accurate cortical segmentations to account for bias field shading. The applicability of T_1W/T_2W ‘myelin mapping’ in HD was demonstrated as an increase in signal was discovered in the most advanced disease group. Ultimately, it was suggested that imaging with increased intracortical contrast-to-noise would be better suited to track more subtle changes in the cortex.

5.2 Future Directions

Based on the findings in this thesis, suggested future directions for ICM mapping focus on improving the quality and sensitivity of the MRIs used as inputs for the image analysis. Also, there is a need for studies that follow up the neuroscience and clinical findings in this thesis with targeted imaging to better understand the mechanism underlying ICM and its relationship with cortical function.

5.2.1 Increased imaging resolution

The resolution of MRI is limited by many physical and practical parameters, especially in terms of clinical applicability. The research in this thesis was conducted at 1mm resolution (Chapter 2 and 3) or 1.1mm (Chapter 4), which is coarse compared to the underlying cortical microstructure. It is interesting to postulate what could be uncovered at higher resolutions enabled by better imaging hardware and scanning protocols. This section comments on the current limitations due to 1mm isotropic resolution when studying the cortex, and highlights the potential for work to be performed at a sub millimeter resolution.

In the Introduction, cortical parcellation using cytoarchitecture and myeloarchitecture was briefly reviewed. MRI studies have attempted to produce their own parcellations based on structural data (Glasser & Van Essen, 2011), and by incorporating functional data (Glasser et al., 2016). It has been noted that intracortical signal measurements are highly reliable (Arshad, Stanley, & Raz, 2017), but there still remains the limitation from previous parcellation schemes of interindividual variability. It could also be argued that these MR-derived fine parcellations of the cortex require too much neuroanatomical precision to match the functional segregation (Nieuwenhuys, 2012). It will be of interest to see if these cortical parcellation maps generated from MRI data remain stable with an increase in resolution that could better delineate the cortical layers. Additionally, as an increasing number of individuals are imaged, it is worth future investigation into the degree of anatomical variation that exists in these myeloarchitectonic parcellation maps. This information will aid in performing MRI

studies as it can either be used to improve registration techniques, or uncover a novel region-of-interest (ROI) approach that better captures and represents an individual's neuroanatomy for group-comparison.

Increases in resolution could also permit improved laminar analysis of the cortex. Early myeloarchitecture work by Kaes found that ICM in the internal principal zone peaks around 19th year of age, where the external principal zone peaks around 45 years (Nieuwenhuys, 2012). The work in Chapter 3 found a peak of 35-40 years of age, across three different cortical depths. The peaks at the different layers found in the histological study may be worthwhile to try and reproduce with higher resolution imaging that is better able to capture the individual cortical layers. This early peak discovered by Kaes was likely missed due to the age range selected for the study in Chapter 3.

It would also be of interest to investigate if the stage of cortical development affects how the brain is parcellated, as the analysis in Chapter 3 highlighted that different cortical areas peak at different points in life. Ultimately, this would depend on the parcellation scheme used, but it is conceivable that parcellations could be unstable due to the differential trajectories of cortical areas. This may have the largest impact during periods of rapid change, such as in the developing brain through childhood, and during neurodegeneration in the elderly. These questions may be revisited with 7 Tesla scanners that facilitate sub millimeter resolution within standard imaging times or in clinical studies that focus exclusively on collecting images for ICM analysis, such as the Human Connectome project which uses 0.7mm isotropic images collected at 3T (Glasser et al., 2016).

5.2.2 Improved Field Homogeneity

Bias fields were introduced in Chapter 1, where it was advocated that its correction is critical for the interpretation of MR signal in ICM analysis. The work in this thesis used a ratio of two images to correct for the smoothly varying bias shading that appears in the collected images. As work in this field moves towards imaging at 7T, it is worth noting that these bias artifacts are worsened by the shortened wavelength of the penetrating RF pulses at the increased magnetic field strength. Thus, developing methodology for accurate correction is important for the progression of ICM mapping. Recent work has aimed to acquire subject specific B_1 maps to perform a data-driven intensity correction. It has been demonstrated that *in vivo* B_1 maps can be generated that improve variable tip angle T_1 maps (Boudreau et al., 2017b), while the effectiveness of this *post hoc* correction varies depending on the T_1 mapping method used (Boudreau, Stikov, & Pike, 2017a). Correcting T_1 maps for B_1 reduces both intra- and intersubject variability in T_1 values (Haast, Ivanov, & Uludag, 2018), which would provide an increase in statistical power. B_1 maps need to be collected at the time of subject imaging, which is a drawback for analyzing previously collected data, as was performed in Chapter 4. Thus, adding a B_1 mapping sequence should be of strong consideration in future ICM imaging studies to perform intensity correction.

5.2.3 Biological Interpretation of ICM Signal

Sequences that are more iron-heavy in contrast, are more likely measuring oligodendrocyte density, rather than myelin sheaths. Whereas using a contrast with more

lipid sensitivity may be more sensitive to changes in myelin. It was noted in the introduction that myelin sheaths are less than 30 μ m from an oligodendrocyte, therefore it should be suspected that the two contrasts would be highly correlated at the resolution of MRI. With the study designs employed in this thesis, the differentiation between the two cannot be made. In future work, it would be valuable to be able to make this distinction in cases of pathology where a change may present itself in either the myelin or in the oligodendrocytes, thus making their contrasts less correlated. Figure 5.1 illustrates the potential mechanisms that could drive a change in ICM signal, that would all be interpreted as an increase in myelin levels. The importance of myelin sheaths was reviewed in Chapter 1, and the role of iron in oligodendrocytes will be reviewed demonstrating its important role in the nervous system. This should suggest that both myelin and iron are worth investigating in the brain in terms of functionality and in disease.

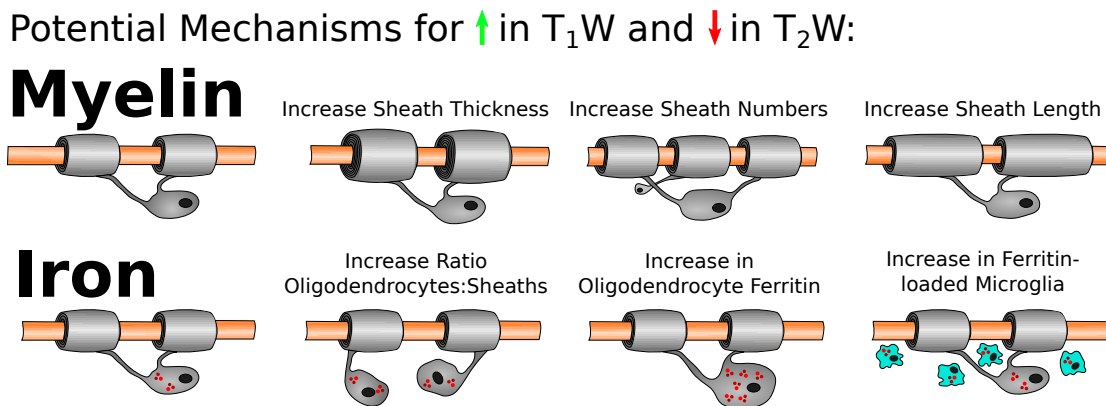


Figure 5.1: Potential mechanisms that could increase intensity in a T_1W image, and/or decrease intensity in a T_2W image.

While iron can be found in other glial cells, it is predominately found in oligodendrocytes in the CNS (Connor, Menzies, St Martin, & Mufson, 1990). Iron plays a critical role in oligodendrocytes as it is required for the synthesis of lipids and cholesterol (Connor & Menzies, 1996), both of which are abundant in myelin sheaths. It has been shown in mice that an iron deficient diet leads to decreased cholesterol and lipid content in their myelin (Ortiz et al., 2004). In addition to that, iron is required by many enzymes necessary for metabolism (reviewed in (Connor & Menzies, 1996)). Thus iron plays a critical role in oxidative metabolism, where oligodendrocytes are known to have double the cellular respiration rates compared to neurons on a per volume basis (Hyden & Pigon, 1960).

It is also worth noting that iron is typically located within the perikarya of the oligodendrocytes, rather than in the myelin sheaths (Connor et al., 1990). Transferrin is one iron transport protein produced by oligodendrocytes, but it has been found that iron distribution patterns do not match that of transferrin (Hill, Ruff, Weber, & Pert, 1985). More recent work has suggested that iron is transported into mature oligodendrocytes by ferritin, rather than transferrin (Todorich, Zhang, Slagle-Webb, Seaman, & Connor, 2008). Indeed, it has been shown that ferritin and MBP demonstrate a high level of co-localization at the laminar level (Fukunaga et al., 2010), which makes it difficult to separate at current MRI resolutions.

Ferritin is comprised of subunits that exists in two types, heavy (H) and light (L) chains. A primary difference is that H-ferritin is able to convert Fe(II) to Fe(III) for storage or use by other cellular processes (Levi et al., 1992). L-ferritin has been suggested

to be used for storage and is found in oligodendrocytes and microglia, where H-ferritin is associated with a high iron turnover/utilization rate and is found in neurons and oligodendrocytes (Connor & Menzies, 1996). Thus the ferritin subunit is related to cell function, as neurons have a high iron demand, but low storage capacity, microglia are considered scavenger cells storing iron, and oligodendrocytes have increased iron usage and storage (Connor & Menzies, 1996). As Fe(III) contributes more to MR contrast as a stronger paramagnet, and since oligodendrocytes contain more iron than neurons, MR signal variances due to iron are more likely to be reflecting alterations to oligodendrocytes compared to other cell types.

5.2.4 Myelin and Metabolism

Due to the high energy demands of oligodendrocytes to maintain myelin sheaths, it is attractive to be able to concurrently study myelin levels and metabolism *in vivo*. One approach could be to investigate changes in cortical iron levels. Iron is important for cellular metabolism as it upregulates the transcription of proteins in the citric acid cycle (Oexle, Gnaiger, & Weiss, 1999), the primary process for aerobically producing adenosine trisphosphate (ATP). Interestingly, Fe(III) supplementation and not Fe(II) together with apotransferrin increased DNA content in the cells (Silvestroff, Franco, & Pasquini, 2013). This evidence suggests that iron has the potential to be used as a surrogate marker in MRI for DNA transcription. It has been shown in the rat brain that oligodendrocytes contain ferroportin, which provides a potential mechanism that allows the oligodendrocytes to export iron to prevent accumulation (Moos & Rosengren Nielsen,

2006). This research suggests that iron concentrations are dynamic within the oligodendrocyte, and its concentration has biological significance.

Magnetic resonance spectroscopy (MRS) is a technique that permits the testing of chemical composition of the brain and could be used to investigate the link between neuron and myelin metabolism. It has been used previously in mice to demonstrate that lactate produced by oligodendrocytes is metabolized within axons in WM (Fünfschilling et al., 2013). A widely used MRS chemical, N-acetylaspartate (NAA), is a unique CNS marker that is produced by neurons (Moffett, Ross, Arun, Madhavarao, & Namboodiri, 2007). NAA can be transported from a neuron to oligodendrocyte where it is used for the synthesis of fatty acids, ultimately facilitating myelin sheath development (Moffett et al., 2007). With the link between myelin and NAA, one may anticipate that it could be used as a metabolic marker for myelin in the brain. Indeed, cortical NAA levels have been shown to decline with age (Angelic et al., 2001), where myelin is also known to decrease. However there exists a conflicting report suggesting no change in NAA with age (Saunders, Howe, van den Boogaart, Griffiths, & Brown, 1999). Due to the strong age-related trends with age presented in Chapter 3, one might expect to see a strong age dependency on NAA concentrations if it were a valid myelin marker. Additionally, as the technique involves interpreting the signal from an isolated voxel, it does not hold promise as a whole-brain myelin mapping technique. However, it may have value combined with other ICM methods, to provide information in studies where signaling metabolics are hypothesized to be compromised.

5.2.5 Cognition and Myelin Mapping

Few studies have investigated the connection of ICM levels and cognitive functionality, such that this correlation should be explored further in the future. A previous study in healthy participants suggested that ICM levels are correlated with consistency in a task. They demonstrated that a higher degree of ICM was associated with greater performance stability (Grydeland, Walhovd, Tamnes, Westlye, & Fjell, 2013). Additionally, it was established that ICM levels in the left posterior cingulate cortex were correlated with error-related negativity amplitude, an electrophysiological response to an incorrect response on a task (Grydeland, Westlye, Walhovd, & Fjell, 2016). Thus, ICM levels could have an impact on one's ability to process mistakes. ICM levels in the insular cortex have been correlated with cognitive empathy scores (Allen et al., 2017). More recently, we showed that ICM levels in BD and not in controls were correlated to verbal memory scores (Sehmbi et al., 2018). This suggests that the adaptability of the brain can be compromised in disease states, where function is ultimately affected. It would be of interest to further this research in clinical populations to correlate ICM levels with functional deficits to obtain a better understanding of its impact on cognition.

Due to the ongoing myelin-related structural changes in the brain with age, it is fair to suspect that this should have an impact on the functionality of the CNS as well. Cognitive studies have demonstrated that the brain is better at preserving certain skills compared to others with age (Craik & Bialystok, 2006; Li et al., 2004; Salthouse, 2009; Siegel, 1994). Most cognitive scores such as memory, reasoning, speed and spatial visualization appear to start declining in the 20's (Li et al., 2004; Salthouse, 2009). It

appears as though short-term memory remains stable through middle-adulthood, while working memory performance decreases (Siegel, 1994). A more recent study reinforced the stability of short-term memory through middle-adulthood, but found that more abstract task scores such as arithmetic, vocabulary and comprehension peaked closer to 50 years of age (Hartshorne & Germine, 2015). Future imaging work is necessary to investigate if these peaks of cognitive function align with peaks of cortical myelination. If a link can be generated between ICM levels and cognitive ability, then it opens up the possibility of cognitive therapy or pharmacological interventions to be developed to restore cognitive function in affected individuals, or maintain functionality through aging.

References

- Allen, M., Frank, D., Glen, J. C., Fardo, F., Callaghan, M. F., & Rees, G. (2017). Insula and somatosensory cortical myelination and iron markers underlie individual differences in empathy. *Scientific Reports*, 1–12. <http://doi.org/10.1038/srep43316>
- Angelic, E., Bonmartin, A., Boudraa, A., Gonnaud, P. M., Mallet, J. J., & Sappey-Marinier, D. (2001). Regional differences and metabolic changes in normal aging of the human brain: proton MR spectroscopic imaging study. *AJNR. American Journal of Neuroradiology*, 22(1), 119–127.
- Arshad, M., Stanley, J. A., & Raz, N. (2017). Test-retest reliability and concurrent validity of in vivo myelin content indices: Myelin water fraction and calibrated T1 w/T2 w image ratio. *Human Brain Mapping*, 38(4), 1780–1790. <http://doi.org/10.1002/hbm.23481>

Boudreau, M., Stikov, N., & Pike, G. B. (2017a). B1 -sensitivity analysis of quantitative magnetization transfer imaging. *Magnetic Resonance in Medicine*.

<http://doi.org/10.1002/mrm.26673>

Boudreau, M., Tardif, C. L., Stikov, N., Sled, J. G., Lee, W., & Pike, G. B. (2017b). B1 mapping for bias-correction in quantitative T1 imaging of the brain at 3T using standard pulse sequences. *Journal of Magnetic Resonance Imaging : JMRI*.

<http://doi.org/10.1002/jmri.25692>

Connor, J. R., & Menzies, S. L. (1996). Relationship of iron to oligodendrocytes and myelination. *Glia*, *17*(2), 83–93. [http://doi.org/10.1002/\(SICI\)1098-](http://doi.org/10.1002/(SICI)1098-1136(199606)17:2<83::AID-GLIA1>3.0.CO;2-7)

[1136\(199606\)17:2<83::AID-GLIA1>3.0.CO;2-7](http://doi.org/10.1002/(SICI)1098-1136(199606)17:2<83::AID-GLIA1>3.0.CO;2-7)

Connor, J. R., Menzies, S. L., St Martin, S. M., & Mufson, E. J. (1990). Cellular distribution of transferrin, ferritin, and iron in normal and aged human brains. *Journal of Neuroscience Research*, *27*(4), 595–611. <http://doi.org/10.1002/jnr.490270421>

Craik, F. I. M., & Bialystok, E. (2006). Cognition through the lifespan: mechanisms of change. *Trends in Cognitive Sciences*, *10*(3), 131–138.

<http://doi.org/10.1016/j.tics.2006.01.007>

Fukunaga, M., Li, T. Q., van Gelderen, P., de Zwart, J. A., Shmueli, K., Yao, B., et al. (2010). Layer-specific variation of iron content in cerebral cortex as a source of MRI contrast. *Proceedings of the National Academy of Sciences of the United States of America*, *107*(8), 3834–3839. <http://doi.org/10.1073/pnas.0911177107>

Fünfschilling, U., Supplie, L. M., Mahad, D., Boretius, S., Saab, A. S., Edgar, J., et al.

- (2013). Glycolytic oligodendrocytes maintain myelin and long-term axonal integrity. *Nature*, 485(7399), 517–521. <http://doi.org/10.1038/nature11007>
- Glasser, M. F., & Van Essen, D. C. (2011). Mapping Human Cortical Areas In Vivo Based on Myelin Content as Revealed by T1- and T2-Weighted MRI. *Journal of Neuroscience*, 31(32), 11597–11616. <http://doi.org/10.1523/JNEUROSCI.2180-11.2011>
- Glasser, M. F., Coalson, T. S., Robinson, E. C., Hacker, C. D., Harwell, J., Yacoub, E., et al. (2016). A multi-modal parcellation of human cerebral cortex. *Nature*, 536(7615), 171–178. <http://doi.org/10.1038/nature18933>
- Grydeland, H., Walhovd, K. B., Tamnes, C. K., Westlye, L. T., & Fjell, A. M. (2013). Intracortical Myelin Links with Performance Variability across the Human Lifespan: Results from T1- and T2-Weighted MRI Myelin Mapping and Diffusion Tensor Imaging. *Journal of Neuroscience*, 33(47), 18618–18630. <http://doi.org/10.1523/JNEUROSCI.2811-13.2013>
- Grydeland, H., Westlye, L. T., Walhovd, K. B., & Fjell, A. M. (2016). Intracortical Posterior Cingulate Myelin Content Relates to Error Processing: Results from T1- and T2-Weighted MRI Myelin Mapping and Electrophysiology in Healthy Adults. *Cerebral Cortex*, 26(6), 2402–2410. <http://doi.org/10.1093/cercor/bhv065>
- Haast, R. A. M., Ivanov, D., & Uludag, K. (2018). The impact of B1+ correction on MP2RAGE cortical T1 and apparent cortical thickness at 7T. *Human Brain Mapping*, 27(8), 1163–14. <http://doi.org/10.1002/hbm.24011>

Hartshorne, J. K., & Germine, L. T. (2015). When Does Cognitive Functioning Peak?

The Asynchronous Rise and Fall of Different Cognitive Abilities Across the Life Span. *Psychological Science*, *26*(4), 433–443.

<http://doi.org/10.1177/0956797614567339>

Hill, J. M., Ruff, M. R., Weber, R. J., & Pert, C. B. (1985). Transferrin receptors in rat brain: neuropeptide-like pattern and relationship to iron distribution. *Proceedings of the National Academy of Sciences of the United States of America*, *82*(13), 4553–4557.

Hyden, H., & Pigon, A. (1960). A cytophysiological study of the functional relationship between oligodendroglial cells and nerve cells of Deiters' nucleus. *Journal of Neurochemistry*, *6*, 57–72.

Levi, S., Yewdall, S. J., Harrison, P. M., Santambrogio, P., Cozzi, A., Rovida, E., et al. (1992). Evidence of H- and L-chains have co-operative roles in the iron-uptake mechanism of human ferritin. *Biochemical Journal*, *288* (Pt 2)(2), 591–596.

<http://doi.org/10.1042/bj2880591>

Li, S.-C., Lindenberger, U., Hommel, B., Aschersleben, G., Prinz, W., & Baltes, P. B.

(2004). Transformations in the couplings among intellectual abilities and constituent cognitive processes across the life span. *Psychological Science*, *15*(3), 155–163.

<http://doi.org/10.1111/j.0956-7976.2004.01503003.x>

Moffett, J. R., Ross, B., Arun, P., Madhavarao, C. N., & Namboodiri, A. M. A. (2007).

N-Acetylaspartate in the CNS: from neurodiagnostics to neurobiology. *Progress in*

- Neurobiology*, 81(2), 89–131. <http://doi.org/10.1016/j.pneurobio.2006.12.003>
- Moos, T., & Rosengren Nielsen, T. (2006). Ferroportin in the Postnatal Rat Brain: Implications for Axonal Transport and Neuronal Export of Iron. *Seminars in Pediatric Neurology*, 13(3), 149–157. <http://doi.org/10.1016/j.spen.2006.08.003>
- Nieuwenhuys, R. (2012). The myeloarchitectonic studies on the human cerebral cortex of the Vogt–Vogt school, and their significance for the interpretation of functional neuroimaging data. *Brain Structure and Function*, 218(2), 303–352. <http://doi.org/10.1007/s00429-012-0460-z>
- Oexle, H., Gnaiger, E., & Weiss, G. (1999). Iron-dependent changes in cellular energy metabolism: influence on citric acid cycle and oxidative phosphorylation. *Biochimica Et Biophysica Acta*, 1413(3), 99–107.
- Ortiz, E., Pasquini, J. M., Thompson, K., Felt, B., Butkus, G., Beard, J., & Connor, J. R. (2004). Effect of manipulation of iron storage, transport, or availability on myelin composition and brain iron content in three different animal models. *Journal of Neuroscience Research*, 77(5), 681–689. <http://doi.org/10.1002/jnr.20207>
- Rajkowska, G., Halaris, A., & Selemon, L. D. (2001). Reductions in neuronal and glial density characterize the dorsolateral prefrontal cortex in bipolar disorder. *Biological Psychiatry*, 49(9), 741–752.
- Salthouse, T. A. (2009). When does age-related cognitive decline begin? *Neurobiology of Aging*, 30(4), 507–514. <http://doi.org/10.1016/j.neurobiolaging.2008.09.023>
- Saunders, D. E., Howe, F. A., van den Boogaart, A., Griffiths, J. R., & Brown, M. M.

- (1999). Aging of the adult human brain: in vivo quantitation of metabolite content with proton magnetic resonance spectroscopy. *Journal of Magnetic Resonance Imaging : JMRI*, 9(5), 711–716.
- Sehmbi, M., Rowley, C. D., Minuzzi, L., Kapczinski, F., Steiner, M., Sassi, R. B., et al. (2018). Association of intracortical myelin and cognitive function in bipolar I disorder. *Acta Psychiatrica Scandinavica*, 161, 262–11. <http://doi.org/10.1111/acps.12875>
- Siegel, L. S. (1994). Working Memory and Reading: A Life-span Perspective. *International Journal of Behavioral Development*, 17(1), 109–124. <http://doi.org/10.1177/016502549401700107>
- Silvestroff, L., Franco, P. G., & Pasquini, J. M. (2013). Neural and oligodendrocyte progenitor cells: transferrin effects on cell proliferation. *ASN Neuro*, 5(1), e00107. <http://doi.org/10.1042/AN20120075>
- Todorich, B., Zhang, X., Slagle-Webb, B., Seaman, W. E., & Connor, J. R. (2008). Tim-2 is the receptor for H-ferritin on oligodendrocytes. *Journal of Neurochemistry*, 107(6), 1495–1505. <http://doi.org/10.1111/j.1471-4159.2008.05678.x>
- Uranova, N. A., Vostrikov, V. M., Orlovskaya, D. D., & Rachmanova, V. I. (2004). Oligodendroglial density in the prefrontal cortex in schizophrenia and mood disorders: a study from the Stanley Neuropathology Consortium. *Schizophrenia Research*, 67(2-3), 269–275. [http://doi.org/10.1016/S0920-9964\(03\)00181-6](http://doi.org/10.1016/S0920-9964(03)00181-6)

Appendices

Reprint Permissions – Figure 1.1

SPRINGER NATURE LICENSE TERMS AND CONDITIONS

Mar 15, 2018

This Agreement between Christopher Rowley ("You") and Springer Nature ("Springer Nature") consists of your license details and the terms and conditions provided by Springer Nature and Copyright Clearance Center.

License Number	4310280276292
License date	Mar 15, 2018
Licensed Content Publisher	Springer Nature
Licensed Content Publication	Brain Structure and Function
Licensed Content Title	The myeloarchitectonic studies on the human cerebral cortex of the Vogt-Vogt school, and their significance for the interpretation of functional neuroimaging data
Licensed Content Author	Rudolf Nieuwenhuys
Licensed Content Date	Jan 1, 2012
Licensed Content Volume	218
Licensed Content Issue	2
Type of Use	Thesis/Dissertation
Requestor type	academic/university or research institute
Format	electronic
Portion	figures/tables/illustrations
Number of figures/tables/illustrations	2
Will you be translating?	no
Circulation/distribution	<501
Author of this Springer Nature content	no
Title	Investigating Intracortical Myelin in Humans using MRI
Instructor name	Christopher D Rowley
Institution name	McMaster University
Expected presentation date	Jun 2018
Portions	Requesting to use figures 3 and 4 highlighting cortical layering patterns.